Direct Injection of Liquid Nitrogen into Water for a Cryogenic Engine

by

Angela Mutumba

A dissertation submitted in accordance with the

requirements for the degree of

Doctor of Philosophy

(Chemical Engineering)

UNIVERSITY OF LEEDS

School of Chemical and Process Engineering

March 2019

The candidate confirms that the work submitted is her own, except where work which has formed part of jointly authored publications has been included. The contribution of the candidate and the other authors to this work has been explicitly indicated below. The candidate confirms that appropriate credit has been given within the thesis where reference has been made to the work of others.

Publications in the Thesis

Chapter 3: Development of a liquid nitrogen injection rig

Design and development of a liquid nitrogen injection rig, Mutumba, A., Cheeseman, K., Clarke, H. and Wen, D., 2018. Design and development of a direct injection system for cryogenic engines. *Cryogenics*, *91*, pp.77-86.

My contributions towards the publication

I was the lead author of this paper and the other three authors inputted ideas and offered guidance and assisted in the editing process.

Acknowledgement

I would like to thank my supervisors, Prof. Dongsheng Wen and Dr. Henry Clarke for their support and guidance throughout the duration of the project. I would also like to express my gratitude to the Department of Mechanical Engineering for their help in the fabrication and repair some of the components of the rig.

I am grateful to Dearman Company Limited and the Leeds Scholarship Foundation for their joint funding and support for this project. I extend a special thanks to Kevin Cheeseman and Adil Karakayis who provided their expertise and knowledge to the project. I would also like to extend a special thanks to Robert Harris whom without, experiments would not have been possible and was never dull.

I would like to extend my gratitude to my parents; Moses and Harriet who have support me in every way possible and without whom I would not be here today. I also extend a special thank you to my partner, Ian who has provided unconditional love and enduring support during the duration of the project. Lastly, would like to thank Miss Doreen Astles for adopting me as her own and being the lovely human being that she is.

I dedicate this thesis to my grandmother who always believed in me and saw the best in me. She will forever be missed but is always in my heart cheering me on.

Abstract

The cryogenic engine was developed as a non-combustion zero emission engine that converts thermal energy to work by the vaporisation of liquid nitrogen using ambient heat. Its output is dependent on the heat transfer rate between liquid nitrogen and the ambient, where the efficiencies of previous designs were operated in an indirect process and heavily reliant on the performance of air heat exchangers used.

The direct injection process was recently introduced to improve the heat transfer rate by directly injecting liquid nitrogen into a warmer fluid. The large temperature difference between two fluids in contact is expected to lead to rapid vaporization of liquid nitrogen, hence improving the performance of a liquid nitrogen engine. However, the feasibility of direct injection is challenged by the lack of an adequate valve system to control the delivery of the cryogen, along with a deep understanding of the heat transfer mechanism involved.

To address these challenges, a fundamental study of the direct injection of liquid nitrogen into water at ambient temperature is conducted in this thesis. A static rig is designed to allow for the control of the injection process in order to investigate the influence of the injection parameters on the pressurisation rate. The injection timing and valve movement are controlled by a hydraulic actuator, which allows for synchronized injections at the desired pressure and temperature. Over 400 injections of nitrogen at different thermodynamic conditions were conducted and maximum pressurisation rates of up to 5156 bar/s were recorded for a clearance volume of 5 ml, which is 10 times greater than those found in the literature as a result of the

increased injection pressure. Based on the pressurization curve, a two-stage boiling mechanism of liquid nitrogen is inferred that occurs inside the vessel, that is, film boiling and breakup of liquid nitrogen jet into small droplets, and subsequent boiling of liquid nitrogen droplets.

To further increase our understanding of these complicated processes involved, a numerical study using CFD software Fluent is conducted to simulate the jetting and boiling of a liquid nitrogen droplet in water. A heat transfer and thermodynamic analysis is conducted and the implications of the results to the engine performance and its development are discussed.

Keywords: zero emission engine, cryogen, liquid nitrogen, direct injection, boiling

CONTENTS

Table of Figures

List of Tables

Nomenclature

α	Volume fraction	
β	Accommodation coefficient	
C_v	Evaporation coefficient	
$\dot{m}$	Mass flow rate	Kg/s
l	Valve lift	mm
η	Efficiency	
μ	Viscosity	
ρ	Density	kg/m^3
γ	Polytropic exponent	
σ	Surface tension	N/m
$\bar{\bar{\tau}}$	Stress strain tensor	
C_d	Drag coefficient	
Re	Reynolds number	
Nu	Nusselt's number	
Pr	Prandtl number	
T	Temperature	
h	Heat transfer coefficient	J/kg.K
k	Thermal conductivity	
m	Mass	kg
p	Pressure	
P	Power	W
V	Volume	m^3

v	Velocity	m/s
W	Work	
A	Area	mm^2
R	Gas constant	J/mol.K
n	Moles	
RMM	Relative molecular mass	g/mol
Q	Heat transfer	J
d	Diameter	
r	Radius	
Λ	Isothermality	
φ	Exergy	J
F	Force	J
U	Internal energy	J
g	Gravitational constant	m/s^2
t	Time	S
h_{fg}	Latent heat	J/kg
$\dot{V}$	Volumetric flow rate	l/s

Subscripts

g	Gas
v	Vapour
l	Liquid
p	Droplet/bubble

w	Water
inj	Injection
sat	Saturation

Abbreviations

TDC	Top dead centre
BTD	Bottom dead centre
ICE	Internal combustion engine
ZEV	Zero emissions vehicle
LNG	Liquified natural gas
HEF	Heat transfer fluid
UHMWPE	Ultrahigh molecular weight polyethylene
FCI	Fuel coolant interactions

CHAPTER 1

1 Introduction

Road transport is one of the major contributors to air pollution in urban areas and is a risk to health and the environment. In 2016, outdoor air pollution was estimated to cause 4.2 million premature deaths worldwide(6), motivating significant effort into researching methods to reduce the amount of polluting emissions in the air.

To reduce greenhouse gas emissions by 60 % of the 1990 levels by 2050(7), the transport sector is forced to find alternatives to the combustion of fossil fuels. One way of achieving this with the substitution of fossil fuels with carbon free energy carriers. Although, research to develop efficient and effective combustion of diesel and gasoline has shown to reduce carbon emissions by up to 50 %(8, 9), stringent legislations and increasing fuel prices have prompted the development of Zero-Emission Vehicle (ZEV) technology.

As early as 1990, the California Air Resources Board passed a mandate aimed to reduce mobile air pollution(10). This required every automobile manufacturer to design cars with zero tailpipe pollutants, which launched an interest in the innovation of clean automotive fuel and engine technology. This led to the production of alternative green engine technology such as electric, biogas, fuel cell and compressed air (11). Each of these has suffered similar difficulties to the road to mass production due to safety concerns, but mainly because of the dependency and reliability that the internal combustion engine (ICE) has established over last two centuries.

To this day, this market is dominated by electric vehicles, with Toyota selling over 75,000 of its Toyota Prius in the UK since 2000(12). Despite its success, battery technology has its shortcomings such as the use of rare earth metals. More recently the technology has been criticised for the recycling and deposal of battery packs and the overall impact on the national grid with increasing sales.

1.1 The cryogenic engine

The cryogenic engine is non-combustion engine developed as zero-emission engine. The basic idea of the engine is to vaporise and superheat a cryogenic fluid using the atmosphere as a heat source for the use in a power cycle. This is in contrast to typical heat engines that utilise an energy source at significantly higher temperatures and use the atmosphere as a heat sink (5). In this case, the cryogen is used as the heat sink and is pressurised, vaporised, expanded and the gas is expelled to the atmosphere.

A cryogen is a liquid or liquefied gas that boils at temperatures below ~123 K. Examples include; liquid nitrogen, liquid oxygen, liquid hydrogen, liquid helium and liquefied natural gas (LNG). The bespoke heat engine utilises the low boiling point of the fluids, which can be vaporised by ambient/low-grade heat. This technology is based off the same principles of the compressed air engine(13), but with the use of liquid air/liquid nitrogen, that has a volume energy density 2.45 times that of compressed air.

Liquid nitrogen is best suited for this application because of its inert nature and widespread use, which has no impact on the environment compared to the burning of fossil fuels. Liquid nitrogen makes it possible for fast fueling, where it can be transferred between vessels at high rates of >100 liters per minute(14). Furthermore, there is significant existing infrastructure and global transportation. The cryogen is produced by the liquefaction of air, which is a well-developed process whose carbon footprint can be reduced with the use of renewable electricity during off-peak time. Industrial gas companies have large amounts of spare nitrogen production capacity because there is far more nitrogen than oxygen in the atmosphere, with proportionately less commercial demand. The abundance of nitrogen further drives down its cost, making it more cost effective in comparison to battery technology. Notably, the price is determined by the cost of electricity used to make it and the cost of diesel used to transport it.

1.1.1 The concept

The technology was developed with the aim of producing a non-combustive, zero-emission engine. Other applications include energy storage systems to store off peak electricity and expand it through a turbine to deliver power at peak times to meet the demand.

It is a heat engine that uses the atmosphere as a heat source to vaporise and superheat the cryogen in a thermal expansion power cycle. In this process, the energy conversion is completely reliant on the heat transfer. In contrast to the conventional engine, the cryogenic engine operates at temperatures at or below ambient and does not require an intricate cooling mechanism.

Operating between 77 and 300 K, the concept shows immense potential with an impressive ideal thermal efficiency (based on the Carnot cycle) of 74%, similar to that of an internal combustion engine. The challenge has been to develop an engine that can successfully harness the available exergy, whilst still being cost effective and marketable to the everyday consumer.

The engine power is a direct result of the boiling and expansion of the liquid nitrogen thereby making the scale of the heat transfer a very important aspect to the engine performance and its efficiencies.

Cryogenic engines have been of great interest since the 1960s when they were developed by NASA as an alternative to cryogenic pumps for the space industry. Over the years, there have been numerous systems presented in literature with the aim of developing an efficient automotive propulsion system using cryogenic liquids as cold thermal reservoirs. These designs (15, 16) involved the use of a heat exchanger to indirectly heat and expand the cryogen to ambient temperature. Inevitably, this meant that the heat transfer performance was predominantly dependant on the efficiencies of the heat exchanger. Icing and a poor isothermal expansion were considered formidable challenges of the concept. In addition, the use of an air heat exchanger resulted in a reduced heat transfer coefficient, thus producing a close to an adiabatic expansion process. This ultimately reduced the specific work done in comparison to that which could be achieved under an isothermal (constant temperature) expansion.

Subsequently, direct injection was proposed in the early 2000s(17). Liquid nitrogen is injected into a pool of the heat transfer fluid (HEF) inside the engine cylinder, resulting in a direct contact heat transfer between the two fluids. The rapid heat and mass transfer process often led to the phase change of one or both streams resulting in violent explosions(18). This was previously investigated as a safety analysis in the nuclear industry(19) and for the spillage of cryogenic fluids during transportation(20). The large interface area coupled with significant temperature difference resulted in an intense film boiling process that resulted in a rapid pressure rise inside the engine cylinder.

The direct injection of liquid nitrogen into water has demonstrated great potential in improving the performance and work output of the engine, which has led to substantially increase in interest in this area. The key interest lies in the injection processes, but only a few experimental studies have been conducted. Wen et al(21) conducted a number of injections of liquid nitrogen into water that resulted in pressurisation rates of up to 5 bar/s, with the observation of jet dynamics and heat transfer coefficients comparable to values found on the boiling heat transfer over rough surfaces. In similar tests(22), greater pressurisation rates of up to 370 bar/s were observed as a resulted of the increased injection pressure and the addition of sub-cooling prior to injection. The analysis showed the benefits of latent heat by controlling the thermodynamic state of nitrogen prior to injection, as well as the use of water as the heat transfer fluid.

These experiments pioneered research for the direct injection of liquid nitrogen for a cryogen engine but, the range and quantity of the results were limited by the

experimental design and the lack of control of the injection itself, which questioned their repeatability.

Contrary to the standard pool and flow boiling heat transfer characteristic of a constant wall temperature or heat flux, the interfacial heat transfer mechanism between the HEF and injected liquid nitrogen is still unknown. Experiments in this area are difficult and not well documented due to the explosive and unstable nature of the boiling processes.

1.2 The Market

The market for ZEVs is still under development, with fossil fuel ICEs still dominating the personal road transport market. There is yet to be a ZEV technology that is ready to compete with already established infrastructure around fossil fuel engines and appeal to discerning consumers. At present, the main factors affecting the adoption of this technology are cost, engine performance, convenience, re-fuelling durations and public opinion. Some of the ways to increase the demand is to educate the public on the benefits of the technology to the environment and the overall savings to be made in reduced fuel consumption.

This has called attention to the complexity of the criteria used to draw an adequate comparison between ZEV and fossil fuel ICE's, and what aspects to focus on in order to appeal to the consumer.

Cost has always been a major concern and comparing the cost of any alternative fuel with petrol prices would be somewhat misleading, as petrol costs vary across the world. Sticking with the purpose for which they were designed, the technology is

benchmarked on its carbon footprint in order to access its impact on the environment. Well-to-wheel analysis has been used to establish a universal criterion to evaluate the energy cost and emission effects of vehicle/fuel systems from fuel production to the vehicle operation(23). Based on these criteria, each engine concept can be graded on both the energy used to produce it but also its greenhouse gas emissions as well. With zero emissions and the use of renewable energy for the liquefaction process, a cryogenic engine ranks rather highly.

Performance and fuel consumption have also been a major concern. Despite the advantages of liquefied nitrogen as a carbon-free fuel, the development of the technology has been hindered by its low energy density of 0.762MJ/kg(24). That is, 47 litres of nitrogen would be required to produce the same power as 1 litre of petrol. This means a vehicle operating solely on the cryogenic engine has a limited driving range and speed and is incapable of competing with that of an ICE.

Instead, the engine seems best suited to a specific application such as the transport refrigeration unit (TRU) currently being developed by the Dearman Ltd. The engine is designed to provide both auxiliary power and cooling for refrigeration trailers. The transport refrigeration market has grown and is projected to grow to $31 billion by 2023 worldwide, due to the substantial increase in non-seasonal agricultural exports of food products in the developing world(25). Currently, transport refrigeration is overwhelmingly powered by diesel; either through a compressor driven by the main engine, or a separate unit capable of consuming over 20 % of the vehicle fuel(26). The cryogenic engine can be used for this because it extracts both power and cold from the cryogen, providing immediate savings in fuel costs and emissions. It would

provide efficient cooling and power to the vehicle's electrified braking, steering, light and other auxiliary power requirements. The use of such a unit has shown to be 50% more efficient in delivering cooling than conventional cryogenic systems using an evaporator (26). By eliminating diesel, the engine reduces the lifecycle CO_2 emissions by 30% – 85%, and potentially by 96% depending on the carbon intensity of electricity used for the liquefaction process. Additionally, it reduces NOx emissions by 70% and PM for 90%(14).

Another possible application is a hybrid configuration consisting of an ICE as the primary engine and the cryogenic engine as the secondary. The hybrid offers greater performance compared to using a cryogen fuel on its own and also reduces the strain on the existing refuelling network. The waste heat and cold from each respective engine can be used to improve both engine efficiencies. A typical ICE has a thermal efficiency of 22 %. Of the wasted heat energy, 30% is lost through the exhaust heat(27), which could be harnessed instead. If the energy costs were based solely on petrol consumption, the energy efficiency increases from 22 to 40-44% (26).

1.3 Aim and scope of the study

The purpose of this thesis is to investigate the influence of injection parameters on the expansion and pressurisation of liquid nitrogen, so as to improve power output and overall efficiencies of the cryogenic engine.

1.3.1 Objectives

1. Design and develop an injection system with the effective control of the injection pressure, temperature and valve actuation so as to investigate the engine pressurisation and ultimately its work output.
2. Conduct an experimental investigation into the pressure build up and phase change when liquid nitrogen is injected into water at ambient temperature
3. Elucidate the obscured jet dynamics and instabilities under hydrodynamic and thermal instabilities, as well as the heat transfer mechanisms that occur inside the engine cylinder using computational fluid dynamics.

1.3.2 Research methodology

This work focuses on the experimental investigation and analysis of the results from the injection of liquid nitrogen into water using the commissioned test rig.

Well characterised injection experiments have been conducted into a closed vessel ranging from 8 to 80 bar, to investigate the effect of independent parameters on the expansion and pressurisation of the nitrogen. The effects of pressure, sub-cooling degree and valve timing have been studied in detail.

Furthermore, computational simulations using Fluent ANSYS have been carried out to clarify the flow dynamics and jet break-up, as well as the boiling of liquid nitrogen inside the water within a blanket of its own vapour cloud.

Experimental and computational results are analysed and discussed and where possible compared to previous investigations.

1.3.3 Thesis overview

The present chapter contains the introduction and motivation for the thesis and outlines the aims and objectives of the research and the method followed. Chapter 2 highlights the fundamental principles of the engine and thermodynamic assessment of its operating cycle, followed by a review of previous designs categorised by indirect and direct injection. A state of art review of the boiling heat transfer when liquid nitrogen is injected into water.

Chapter 3 addresses the description of the test rig and its operation, detailed description of the main components and the data acquisition. This is followed by a series of baseline tests to determine the limitations and of the test rig. The chapter also presents experiments conducted to control and measure the mass of nitrogen injected. Chapter 4 presents the results of the pressurisation from the liquid injections and a discussion on the implications to the results on the engine's operation and performance. Chapter 5 reports the results from the computational simulations on the flow breakup of the injected jet and also the film boiling of a liquid nitrogen droplet immersed in water. Lastly, Chapter 6 highlights the key accomplishments of the study as well as improvements and suggestions for further work.

This work confirms the potential of the direct injection of liquid nitrogen in improving the pressure rise and therefore the power output of the engine. The test bed allowed for the control of the injection process and for a systematic investigation of injection parameters on the rate of change of pressure inside the cylinder.

The injection of liquid nitrogen although beneficial, requires modification of the injection system and poses a limitation on the engine speed in order to effectively extract the exergy of the injected cryogen fuel.

CHAPTER 2

2 Background

This chapter presents an in-depth look at the thermodynamic principles by which to judge the engine's performance and efficiencies. This is followed by a review of indirect and direct injection methods leading into a detailed literature review of the injection of liquid nitrogen into water.

2.1 Thermodynamic principles

The cryogenic engine is a non-cyclic, open circuit work producing device and like the ICE it is very convenient to compare its performance with ideal air standard cycles(28). Based on ideal gas behaviour, these cycles will have some limitations especially for nitrogen at very low temperatures. Even so, standard air cycles are still used to identify important trends associated with improvements to the cycle efficiency.

All engines undergo a mechanical cycle but are assessed by comparison of the thermal efficiency (Equation 2.1) of air standard cycles. This is because of the similarity between the engine indicator diagram and the state diagram of the hypothetical cycle(28). The thermal efficiency (based on the Carnot cycle) of a cryogenic engine operating between 77 K and 300 K is 74 %, which is very similar to that of the ICE operating between 300 K and 1273 K. This demonstrates that as an ideal heat engine, they demonstrate a similar potential to do work. However, the Carnot cycle is based on ideal processes that are far from what is realistically attainable.

$$\eta = 1 - \frac{T_c}{T_h} \qquad 2.1$$

The cycle assumes that nitrogen/air undergoes an isothermal and adiabatic expansion, meaning that the expansion occurs at a constant temperature without the addition of heat or work to the system. Previous investigations revealed that to maximize the specific work output of the engine, an isothermal expansion was more desirable than an adiabatic one(29). The term quasi-isothermal is often used to acknowledge that in practice the heat transfer rates and temperature differences will limit the performance of such an engine(16).

Whilst an adiabatic expansion is favourable for the conventional ICE as heat flows out from the combustion gases, it is desirable for the cryogenic engine to have a quasi-isothermal expansion as any heat added for example; the waste heat from the primary engine can be converted into work and increase engine efficiencies.

Another example where the Carnot cycle differs from the actual process is that it is based on a closed cycle, in which the working fluid is returned to its original state. In contrast, the Dearman engine operates on an open cycle where the now expanded nitrogen gas is expelled to atmosphere, thus eliminating the compression part of the cycle.

Even though researchers were aware of the energy storage potential of the cryogen, there was still disagreements on the best means to converting it to useful work. Accordingly, numerous theoretical cycles to harness this work potential for automotive propulsion were investigated (30-33). The possibilities include open or closed gas cycles (e.g. Stirling, Brayton) and Rankine vapour cycles however, after

numerous investigations the isothermal expansion of the gas in a Rankine cycle showed to produce higher outputs (16).

2.1.1 Practical shaft work

Assuming a polytropic expansion $(pv^{\gamma} = const)$ that is bounded by adiabatic and isothermal condition, the work delivered by the power-expansion stroke is calculated by:

$$w = \int_1^2 pdv = p_1 {v_1}^{\gamma} \int_1^2 \frac{1}{v^{\gamma}} dv = \frac{p_2 v_2 - p_1 v_1}{1-\gamma}$$

$$= \frac{RT_1}{\gamma - 1}\left[1 - \left(\frac{p_2}{p_1}\right)^{\frac{\gamma-1}{\gamma}}\right] \qquad 2.2$$

where $\gamma = 1$ for an isothermal expansion of an ideal gas

$$w = \int_1^2 pdv = p_1 v_1 \int_1^2 \frac{1}{v} dv = p_1 v_1 \ln\frac{v_2}{v_1} = RT \ln\frac{p_1}{p_2} \qquad 2.3$$

Figure 2.1 shows the specific work plotted as a function of the engine peak pressure. Increase in the peak pressure results in the higher specific work output for an isothermal expansion in comparison to an adiabatic one. Prior thermodynamic analysis has also shown a monatomic increase in the isothermal work with increasing injection pressure, in comparison to an adiabatic cycle that demonstrated a weak dependency when it exceeded 4 MPa (40 bar)(3). Therefore, it is apparent that to fully maximise the available exergy of the liquid nitrogen, the engine should ideally operate at high heat transfer rates, to achieve a quasi-isothermal expansion.

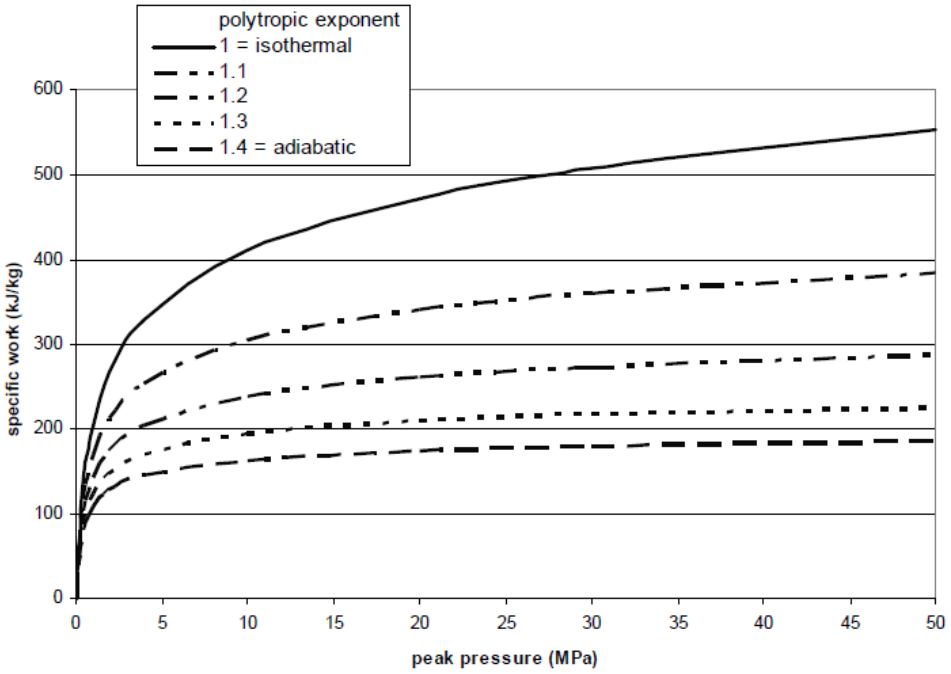

Figure 2.1: Specific work of a polytropic expansion with increasing peak pressure(1)

The pressure rise is a direct result of the expansion of the nitrogen and therefore the mass of nitrogen injected plays a vital role in its performance. Assuming the ideal gas law (Equation 2.4), it can be shown that the mass has a direct correlation with the pressure variation in a fixed volume.

$$pV = nRT \qquad 2.4$$

As a heat engine, the thermal efficiency is used to quantify the performance or work output of a cryogenic engine. It is conventionally the ratio of the amount of work output to the heat input. However, for a cryogenic engine, the utilisation of its free infinite heat source is less informative to its performance. A more appropriate efficiency is the ratio of the actual work output of the engine, to the maximum energy that can be released from the nitrogen. This demonstrates the percentage utilisation of the nitrogen and is referred to as the energy/cycle efficiency.

Accordingly, the cycle efficiency η_c , is a logarithmic function of the pressure ratio of the actual work, to the exergy of nitrogen; where exergy is defined as the available energy to do work (Equation 2.5). A large pressure ratio would call for a larger piston stroke and a shorter injection period before the piston moves from TDC. Unfortunately, at high speeds this would be impossible, thereby reducing the cycle efficiency. In this case, it is recommended to have several cylinders in operation to achieve significantly high speeds (> 1200 rpm) and power.

The efficiency of the cycle can be increased by adopting multistage multi-medium cascading. However, these improvements also increase the complexity and most likely the weight of the engine.

$$\eta_c = \frac{w_{actual}}{\varphi} \quad where\ w_{actual} = RT \ln \frac{p_1}{p_2} \qquad 2.5$$

With the expansion in the cylinder between an adiabatic and isothermal process, a parameter is introduced to quantify the extent to which this occurs. Therefore, the term isothermality (Equation 2.6) is the ratio of the actual work output to isothermal work:

$$\Lambda = \frac{w_{act}}{w_{iso}} \qquad 2.6$$

The isothermality is typically between 0.75-0.90 for reciprocating engines and can be improved by enhancement of the heat transfer process during the expansion(3). Studies have showed a 245 kJ/kg output for an engine operating at Λ=0.9, corresponding to a cycle efficiency of $\sim$ 32 %(31).

To determine the net-work produced by the engine, friction and thermodynamic losses are accounted for in the cycle(η_{cycle}), pumping(η_p) and transmission(η_{trans}) efficiencies. Accordingly, the practical shaft work of the engine can be expressed as:

$$W_{net} = \eta_{trans}\left[\eta_c \Lambda W_{exp} - \frac{W_p}{\eta_p}\right] \quad 2.7$$

Unfortunately, due to the novelty of the engine, this information is still not available in literature.

2.1.2 Heat transfer and pressurisation

The pressurisation in the engine is a direct result of the heat transfer to the nitrogen. The law of thermodynamics is used to simplify the process to correlate the heat transfer and work output of the engine with the rate of pressurisation.

The first law of thermodynamics states that a change in internal energy of a system(ΔU) is equal to the heat added to the system(Q), minus the work done by the system(W) (Equation 2.8). For an isothermal process, the temperature remains constant therefore, $\Delta U = 0$. Accordingly, Equation 2.8 becomes Equation 2.9, and the heat transferred to the system is equal to the work done by the system.

$$\Delta U = Q - W \quad 2.8$$

$$\therefore Q = W \quad 2.9$$

The direct contact film boiling heat transfer and phase change involved in a cryogenic engine is simplified by assuming the system is in a quasi-equilibrium state.

By the differentiation of the ideal gas law (Equation 2.4) where p is the pressure in the cylinder, V is the clearance volume, T_g is the gas temperature and n is the moles of nitrogen injected; the pressurise inside the vessel can be determined equation with respect to time as shown in Equation 2.10. Nitrogen injection occurs at TDC and the expansion is assumed to occur at a constant volume.

$$V\frac{dp}{dt} = RT\frac{dn}{dt} + nR\frac{dT}{dt} \qquad 2.10$$

Due to the small ratio of nitrogen, the temperature of the HEF is assumed unchanged and at thermal equilibrium with the nitrogen gas. Therefore, the term $nR\frac{dT}{dt}$ becomes negligible resulting in:

$$V\frac{dp}{dt} = RT\frac{dn}{dt} \qquad 2.11$$

The mass of nitrogen expanded m is given by the energy balance:

$$m = {Q}/{h_{fg}} = n \times RMM \qquad 2.12$$

where h_{fg} is the latent heat (enthalpy difference between liquid and vapour phase) and m is also equal to the product of the moles (n) and molecular weight (RMM) .

Combining Equations 2.11 and 2.12 gives:

$$\frac{dQ}{dt} = \frac{1000}{28}\frac{Vh_{fg}}{RT_g}\frac{dp}{dt} \qquad 2.13$$

Because $Q = W$, then:

$$\frac{dQ}{dt} = \frac{dW}{dt} = Power\ out\ (kW) \qquad 2.14$$

Heat calculations for an isothermal expansion indicated an efficiency of up to 85 %. Consequently, a theoretical example of a two cylinder- engine operating at an injection pressure of 60 bar at 850 RPM would produce 15 kW and 190 N.m torque, enabling a vehicle to travel 140 km on 200 litres of liquid nitrogen(16).

2.2 Indirect injection engine

In the 1990s there was a lot of emphasis on zero-tailpipe emissions in the USA, and increased legislation led to a significant interest in the production of ZEVs. The University of Washington initiated a programme on cryogenic heat engines to produce a direct substitute for electric vehicles(16). This was based on the premise that liquid nitrogen had a higher specific energy than battery technology at the time, as well as significant advantages in performance and cost.

Indirect injection engines consisted of a cryogenic pump and external heat exchanger to eternally pressurise and vaporise the liquid nitrogen. The high-pressure gas is then used to drive either a reciprocating or turbine expander to do work (Figure 2.2). Icing and fowling of the evaporator resulted in low efficiencies and the designs were often criticised for their bulkiness and weight. It was quickly identified that the key to improving the heat transfer was to increase both the heat transfer coefficient and the total wetted area in the evaporator.

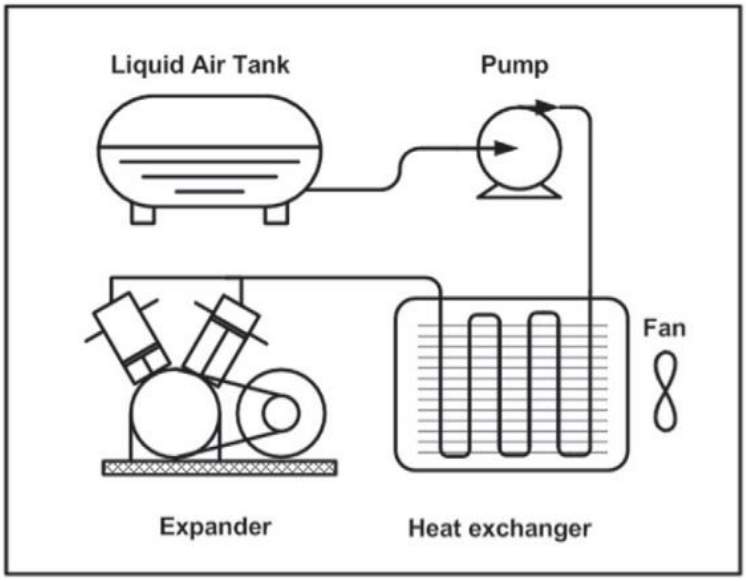

Figure 2.2: Indirect injection system for a cryogenic engine (4)

To expose the injected gas to a larger surface area, a finned piston head (Figure 2.3) consisting of multiple conical fins fitted into a heater core was suggested(3). Embedded in the top of the expansion cylinder it would provide a higher surface to volume ratio in the initial stages of the expansion, which would facilitate a higher heat transfer process. The theoretical analysis of the proposed idea indicated an

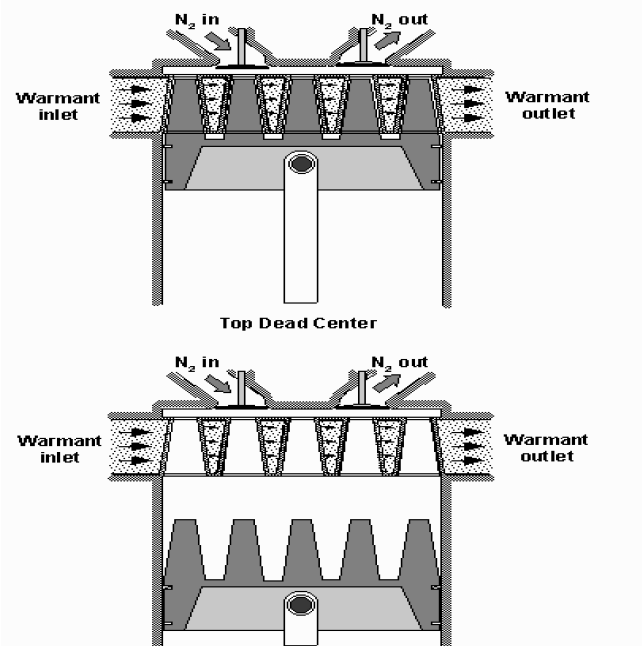

Figure 2.3: Conception piston head with heat transfer fins (3)

increase of over 80 % in the isothermal work however, careful and intricate design of the piston head would be necessary to realise its full potential.

Other suggestions included the circulation of the warm air in the cylinder walls to maintain a 10 K temperature difference. The analysis also demonstrated a promising performance thus far, with an energy efficiency of 45% (194-314 kJ/kg) depending on the quality of the isothermal expansion(16). However, the concept suffered with a poorly sized and heavy portable vaporiser that required 1.5kW for just the circulation of warm air so as to maintain the cylinders at 10 K below ambient at high speeds.

Another approach looked at the combination of cryogenic and combustion engines to utilise the combustion of fossil fuels to elevate the temperature of the nitrogen and supplement the work obtained from the initial expansion(34, 35). The engine makes use of wasted heat from the combustion process allowing for multiple expansions, with reheats in order to extract more energy created by the large temperature difference.

Other attempts to increase the work output focused on modifications to the engine cycle. These included the addition of cryogenic pumps for multiple stage pressurisation and numerous air flow heat exchangers, for a multistage expansion of nitrogen (36). Multistage expansion allowed for re-heating between stages in order to enhance engine performance. However, this could be difficult to achieve under varying power requirements, because of the control required for the multiple expansions. Although the theoretical analysis showed an energy efficiency of 25-36%

without an isothermal expansion, its practicality was brought it question due to the exclusion of pumping losses in the analysis. Furthermore, the design was critiqued for its unnecessary complexity and inadequate control of the injection process, due to the use hand-pump priming system.

Subsequently, the use of cam lobes located on the crankshaft to time the movement of the valves was introduced. Initial testing revealed the need for longer valve opening times at lower injection pressures in order to yield the same stroke as that at higher pressures(37). Sadly, the design lacked a thermodynamic or heat transfer analysis and therefore no definitive figures of their engine efficiencies.

To improve the performance of another combustion free prototype, the University of North Texas(38), investigated several means of achieving complete expansion in the engine cylinder using a dual expansion. This consisted of an isobaric expansion as the gas enters the expander, followed by a second isolated isothermal or adiabatic expansion. However, the rotary vane–type expander was only able to achieve the isobaric part of the expansion and was limited to a maximum inlet pressure of 7 bar. This limited its driving range to 24 km between refills at a poor fuel consumption of 0.13 km/l(38).

Subsequently, others(30) proposed the use a closed Brayton cycle as a possible alternative for the vehicle. The concept was based on the heating and expansion of cold nitrogen gas, as opposed to liquid nitrogen which is simply used a as a heat sink to condense the actual working fluid. The analysis showed an improvement in the

work output that was 10 times that of the open cycle but, it was based off assumptions that the expander operated at over 90 % efficiency.

The performance of these designs was heavily dependent on the efficiency and operation of the heat exchangers and turbines used. It was also clear early on that the engine speed and power would be limited not only by the energy density of liquid nitrogen, but the speed of the heat transfer process to allow for the complete expansion inside the cylinder.

2.3 Direct injection engine

Direct injection was introduced to enhance the heat transfer to the cryogen by eliminating the use of heat exchangers. The idea was to inject liquid nitrogen instead of compressed gas into a reciprocating expander with the piston held at TDC. It was assumed that the nitrogen vaporised very quickly to ambient temperature, achieving a peak pressure very early into the engine stroke. The rapid heat transfer was achieved using hydraulic fluid as a heat source, which also served as a lubricant and seal to the piston. However, this limited the engine speed and made it impossible to achieve a swift variation of engine power.

The idea was improved in most recent designs(39, 40) that were purposely developed to enhance the heat transfer by the direct injection of liquid nitrogen into a HEF contained in the engine cylinder as shown in Figure 2.4. The design concept provided a method of direct contact heat transfer between two fluids, thus increasing the

speed of the heat transfer process and consequently the pressure build-up inside the engine cylinder.

The cooled HEF is reheated and recirculated through a heat exchanger, where it is returned to ambient temperature and pumped into the cylinder at optimal pressure. The liquid nitrogen is also injected at TDC and all the contents of the cylinder expelled

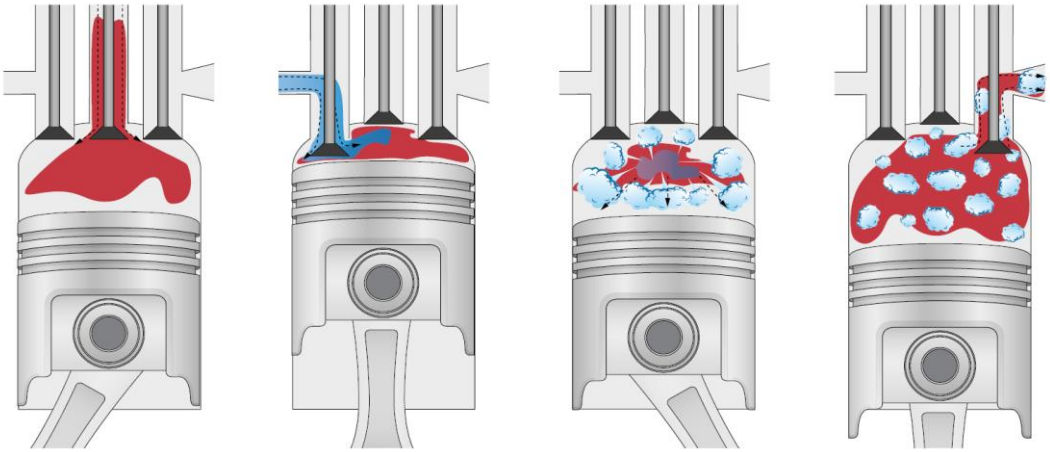

Figure 2.4: Operation of the cryogenic engine with the direct injection of liquid nitrogen into a heat transfer fluid at ambient temperature(5).

through the exhaust valve; where now expanded nitrogen is bled off at the HEF reservoir. The reciprocating movement of the piston is governed by the cam, where part of the cycle includes a time period in which the piston is held at TDC, at or close to the minimum chamber volume. During this time the intake valve admits the HEF, followed by the liquefied gas at the desired pressure.

The injection system was designed to optimise and control the admission of the pressurised liquid nitrogen. It consisted of a housing where liquefied nitrogen was slightly heated to attain an injection pressure before it was delivered to the inlet of the engine chamber. The timings of the inlet valve and the outlet valve of the housing

were synchronised so that when one was opened, the other was closed. The housing was fabricated to function as a heat exchanger to facilitate the transfer of heat between the two fluids, prior to delivery in the chamber.

A variation of the apparatus was accommodated the use a slush instead of a liquid was proposed(41) so as to convert more energy from the phase change and increase the engine's output. However, no performance figures were mentioned, and a lot of energy would be required to store the slush at such low temperatures.

Several variations of the direct injection design have led to the current generation of Dearman engines(5), which use direct contact heat transfer with the injection of saturated nitrogen into water as the HEF. This initiated research into understanding the fundamental heat transfer mechanisms that occur during the injection process in order to develop this engine technology.

2.4 State of Art: Direct injection of liquid nitrogen

2.4.1 Experimental

The most critical process of the cryogenic engine is the injection process. Direct contact heat transfer between two immiscible fluids occurs in several industrial processes and a few relevant studies are reviewed here. A rapid heat transfer is facilitated by the larger interfacial area between the two fluids. Phase change is likely to occur in one or both streams which could enhance mixing and result in a violent vapour explosion(42).

2.4.1.1 Fuel-coolant interactions

Violent vapour explosions were observed in light water reactors when high temperature molten metal came into contact with a coolant that is at ambient temperature. These were a great safety concern for the nuclear industry and extensive research has been conducted in this area. This interaction was found to result in the violent film boiling of the coolant due to large temperature difference.

Studies of the injection of water into a cryogenic pool were conducted to replicate these fuel-coolant interactions (FCIs) in the nuclear industry (43). The experiments revealed the strong influence of the water to liquid nitrogen interaction, as well as a minimum injection pressure above which the strong interaction would occur. The injection pressure was increased to acquire an adequate injection velocity to initiate hydrodynamic fragmentation upon impact (44), which increased the pressurisation inside the chamber. The rates of the pressure rise were a magnitude greater than those that did not demonstrate a vapour explosion

The formation of some hollow ice debris in the chamber, as a result of the ratio of liquid nitrogen to water, suggested that this was a result of trapped liquid nitrogen inside the water droplet, which was heated, expanded and vaporised; before escaping(19). However, before the nitrogen could be vaporised, the water is quenched and solidified into the resulting ice debris. In effect, this confirmed the existence of an interface (vapour layer) surrounding the liquid nitrogen, hindering the immediate transfer of heat. Unfortunately, it was impossible to quantify the boiling heat transfer because of the ambiguous and unmeasurable contact area.

Some numerical studies (18) were undertaken to estimate the interfacial area during the direct contact. Duckworth et al(43) attempted a thermodynamic analysis of similar experiments using a systems code in order to investigate the accidental failure of cryogenically cooled magnets. This was a method to calculate the interfacial area from the pressure curves, which were based on heat transfer coefficient correlations for film boiling over a vertical surface. The analysis could not be verified to the lack of visibility of the interface and thus making it impossible to select a suitable heat transfer correlation. Another code was developed and used to simulate the injection structure based on the pressure curves, however it was still unclear how these could be translated to an injection inside a closed vessel or with the inclusion of sensible heat transfer(18).

Although there is extensive work on surface film boiling, there are a few studies that are comparable. For the more common film boiling, it is well documented that the process is highly dependent on the surface characteristics of the heating element and the thermal properties of the fluids in question (45-48).

The liquid-liquid film boiling, in this case, is further complicated by non-constant heat flux, interfacial area and high temperature and velocity gradients at the interface between both liquids. The lack of visibility due to the formation of the vapour blanket makes it difficult to gather any comprehensive data and any information at the interface is physically impossible to measure. Accordingly, there are only a few relevant publications in this research area.

2.4.1.2 Direct contact heat transfer

There is limited research on the direct contact heat transfer between two immiscible fluids(49-53). However, it will be informative to draw comparisons with more common cases and experiments involving liquid to liquid heat transfer such as the film boiling of cryogens on water. These have been mainly researched to investigate the accidental spillage of a toxic cryogenic such as liquefied natural gas (LNG), which resulted in the spread of a toxic vapour cloud. Various numerical and experimental studies(20, 54) were mainly focused on the pool spread and vapour dispersion, but results were mostly qualitative. The analytical treatment of the heat transfer was approached in two ways; (1) by determining the heat transfer rate to the liquid pool or (2) by analysing the evaporation time of a single droplet on a surface.

The accepted theory was that heat transfer to the liquid pool or a liquid drop from the surface was proportional to the heat needed for the bubble/vapour formation. Investigations concluded that the breakdown of vapour film would occur due to either instability at the vapour-liquid interface, or the decrease of the temperature difference which would fall below what was needed to maintain the vapour film(55). With the reduction of the vapour film, more liquid is able to gain contact with the heating surface/medium causing an increase in the heat flux and the onset of transition boiling.

Numerous studies on the evaporation of liquid nitrogen droplets are available in literature. A study(56) of the Leidenfrost evaporation of a stationary liquid nitrogen droplet on different surfaces showed that the variation in the shape of the droplet as

it evaporates, posed a significant challenge to the development of numerical models where the initial shape of the droplet had to be defined. In agreement with previous authors, the study also observed the reduction of the vapour film as the droplet decreased in size due to increased contact with the heated surface.

2.4.1.3 Injection of liquid nitrogen into water

Research by Wen et al(21) investigating the injection of liquid nitrogen into water was conducted in relation to the cryogenic engine. The conditions inside the pressure vessel were to replicate that inside the engine cylinder however, the liquid nitrogen to HEF ratio was scaled up to obtain practical measurements of the pressure rise. Pressurisation rates of up to 5 bar/s and a peak pressure of 2.84 bar were recorded. Three stages of the pressurisation were identified with the rapid increase in the pressure gradient a result of the rapid boiling and expansion of the liquid nitrogen. The pressure gradient and the peak pressure were found to increase linearly with the injection pressure, but the data was limited to an injection pressure of 3.3 bar. There was no significant variation to the water temperature due to the large water to nitrogen ratio. Similar observations were made by Drake et al. (47)investigating the transient boiling of liquid nitrogen on water. The heat transfer coefficient was comparable to values for the flow boiling over very rough surfaces associated with high nucleation sites for the formation of bubbles found in literature. This was because of the rippled surface of water provides the same effect as the grooves and dimples on a solid surface to promote the nucleation of bubbles during boiling.

The continuous monitoring of the liquefied nitrogen temperature pre-injection was neglected and the thermodynamic state of nitrogen prior to injection was unknown. The interfacial area was assumed to be a cylindrical shape: πdl; where l is determined by the penetration of the injected jet and d the bore diameter of the injector. Although this is a reasonable assumption initially, it is more likely that this shape would be completely altered on its impact with the water surface and continues to change as it evaporates. Accordingly, this draws attention to the influence of the inertia and surface tension forces on the jet and therefore its Weber number especially with injection velocities of between 3-18 m/s(18).

Subsequently, visual experimentation(22) of the injection process observed the jet structure and propagation through a pool of water in a similar set up as previous work. The thermodynamic state of the nitrogen prior to injection was identified by the synchronised measurement of temperature and pressure. Higher pressurisation rates were recorded by liquid injections, in comparison to gas, demonstrating the benefits of latent heat. Pressurisation rate of up to 362 bar/s were observed, which were $\sim$70 times higher that attained before. Like previous experiments(21, 57), the pressurisation rates and peak pressure also showed linearity with the increasing injection pressure ranging to up to 14 bar.

The highest pressure gradient was observed to coincide with the jet break up due to impact with the walls of the vessel. However, the majority of the heat transfer occurred whilst the jet was still in a continuous stream surrounded by its own vapour. There was very little mixing with the water which could only occur as a result of further turbulence in the pool of water. Visual confirmation of a liquid core inside

the jet stream was observed a few milliseconds into the injection which was characterised with the rapid acceleration of the pressurisation. A large velocity and thermal gradient across the jet was formed due to high velocity and temperature difference between the two fluids, thus resulting in a boundary layer. Similar findings were observed in previous research related to the heat and mass transfer of impinging liquid nitrogen jets below the surface (58).

The propagation and consequently penetration depth of the jet was greatly influenced by the fluctuation of buoyancy and momentum forces acting on the jet stream, which increased with the rapid evaporation of the liquid nitrogen, and the momentum flux controlled by the variation to the jet velocity during its propagation(58). A thin velocity and thermal boundary layer are formed at the stagnation zone, as a result of the rapid deceleration and temperature variation due to its impact with the surface. The thickness of the boundary layer was thought to be up to a tenth of a micro-meter, which resulted in a very high heat transfer coefficient.

Generally, the primary breakup of any liquid jet is categorised into two stages; the initial stage where jet surface agitation at the nozzle exit is due to aerodynamic forces, and the second stage where the initial instability grows due to further aerodynamic interactions. For jets that were injected from a nozzle under turbulent conditions, it was argued that initial instability was a result of eddies within the flow(59). Under laminar conditions, destabilisation was caused by Kelvin-Helmholtz instability where the most unstable wavelength is proportional to the thickness of the gas boundary layer formed in the annular nozzle(60). The liquid core length (jet break up length) is an important parameter used to describe the axial downstream

location where the jet's continuity is intact across its entire cross-section. Although several correlations (59, 61, 62) for the measurement of the core length are available in literature, no single correlation can predict the core length for other experiments.

Studies of the primary jet breakup of liquid nitrogen in subcritical and supercritical environments showed a decrease in core length because surface instabilities were amplified with the increase in chamber pressure (60-62). Droplets and ligaments were seen to emerge from the jet at pressures of 0.83 times the critical pressure (33. 4 bar). The break-up of droplets from the vapour blanket was never confirmed in Clarke's(22) injection experiments, but the formation of ligaments due to Kelvin–Helmholtz instability was observed.

Liquid nitrogen into water (L-L) revealed better pressurisation in comparison to liquid nitrogen into air (L-G) injections, because water is not only a better conductor of heat but drag/aerodynamic forces are enhanced by the presence of the denser fluid which caused the impinging jet to disintegrate enhance the turbulent mixing and exchange of heat between the two fluids.

The few studies mentioned in this section have pioneered research in this area and have provided significant insight into the physical mechanisms that dominate the subtleties of the injection process. However, they also highlight some key areas that required further experimental testing and computational modelling to clarify theories and assumptions of the jet break up that were lacked any quantitative data.

2.4.2 Computational

Computational Fluid Dynamics (CFD) can be a useful tool to further our understanding of the injection process especially due to the lack of visibility of the process inside the engine cylinder. In such cases, virtual experimentation can be performed numerically with the ability to explore the control of difficult parameter or in some cases provides information that cannot be physically measured.

The Navier Stokes equations used to describe the behaviour of fluid through a controlled volume are based on the conservation law of the physical properties of fluids. The terms introduced into the Navier equations are still entirely reliant on experimental data, thus limiting their range and capability(63).

The jet dynamics and liquid interaction during the injection process is of particular interest here. The process requires a complex model to describe the hydrodynamic and thermal interaction between the water, liquid and gas nitrogen phases. There are very few studies in this area because of the fundamental physics involved in the three-phase interaction is still not well understood. Additionally, the problem is a transient process that is further complicated by the variation of the interfacial contact area between the fluids in both space and time.

2.4.2.1 Approach to computational modelling

Several researchers adopted the use of molecular dynamics (MD) to analyse the molecular interactions in order to understand the bulk behaviour of complex fluid behaviour. MD can provide a new means to study the heat and mass transfer in micro/nanoscale where classical macroscopic thermodynamic theories have failed to

describe fluid behaviour in such extreme conditions. MD is a particle-based method, where the problem is scaled down to define each molecule and corresponding intermolecular forces between each pair. Although the approach may have some promise in this application, they have extremely small spatial scales, which have an exponential increase in the computational costs and yet would at best confirm what we already know from studies conducted on a macro scale. Furthermore, the characteristic time of the fluid molecules (often 10^{-12} s) is much shorter than that of the dispersed particles.

As an alternative, coarse graining methods such as dissipative Particle Dynamics (DPD) can be used to simulate the hydrodynamic behaviour but on a larger mesoscopic scale(64). Mesoscopic simulations simplify complex models by identifying the characteristic physical lengths and times in the system and therefore provide a bridge between atomistic and macroscale simulation methods. Molecules are clustered into particles, which reduces the particle-particle interactions and allows for increased computational speed. With energy conservation, DPD accounts for the multibody thermodynamic hydrodynamic interactions(65) and give accurate dynamic and transport properties(66). The use of DPD simulations to model the phase change at a solid/liquid interface has been successfully conducted but weighs heavily on how the conservative force is calculated. However, the fluid still does not undergo an automated phase change and would require the definition of particle forces. Owing to the limitations of both MD and DPD, this work focuses on the use of CFD models to study the multiphase flow dynamics and heat transfer involved in the injection process.

2.4.2.2 Multiphase modelling

Currently, there are two approaches to the modelling of multiphase flows; the Eulerian-Eulerian and Eulerian-Lagrangian models. The Eulerian model defines the fluid as a continuum and calculates the flow properties at discrete points, whereas Lagrangian considers the fluid to be a collection of particles and tracks each individual point moving at its own independent velocity. In the Eulerian-Lagrangian, the primary/continuous phase is treated from a Eulerian standpoint and the discrete/secondary phase from the Lagrangian perspective. The Lagrangian approach gives a more comprehensive physical interpretation of the fluid –particle interactions and is, therefore less subject to discretisation errors. Then again, because the particles are modelled as volume-less points, the approach is not applicable where the dispersed phase has a high-volume fraction.

A Eulerian-Lagrangian model developed to simulate fuel-coolant interactions (Section 2.4.1.1) where liquid nitrogen droplets were defined as the discrete phase, proved the approach inadequate due to the profound effect of the choice of the drag coefficient and the particle size of the droplets in the flow field (67). The coefficient used for solid–sphere particles ($C_D = 0.4$) was found to be too low and therefore would prolong the jet's propagation due to the difference in size of the droplets(68). A coefficient about 6 times this gave more reasonable results and has been used in more recent work (18).

At high Weber numbers, the interfacial instability was ignored on the basis that jet dynamics were governed by inertia forces. However, with a variable density due to the phase change, this assumption is invalid for a nitrogen jet(67).

In an attempt to measure the penetration depth of the liquid nitrogen jet in water, Dahlsveen et al.(18) presented a transient axis-symmetric multiphase model for incompressible flow. Like Nougavie et al.(67), liquid nitrogen was also modelled as a discrete phase of spherical droplets, with both the liquid and vapour assumed to be at saturated temperature. The results were in good agreement with the experimental data presented previously(69). The initial size of the droplets (length scale) was computed by the jet Weber number and specified in the code along with a drag coefficient of 2.5. While the length scale of the water and liquid nitrogen were modelled by transport equations, that of the nitrogen vapour was kept constant. The conservation of energy for water was further simplified by assuming that the change in enthalpy was equal to the heat released to the cryogen and therefore the rate of vaporisation was given by Equation 2.15.

$$\dot{m}_v = \frac{6\alpha_w \alpha_l h(T_w - T_{sat})}{d h_{fg}} \qquad 2.15$$

where the heat transfer coefficient h was determined by taking the maximum of the forced convection and free convection film boiling coefficients for a sphere of diameter d.

The momentum equation was solved for each particle, thereby making this approach not only computationally expensive but incapable of account for the sensible heat transfer before and after the saturation temperature. Additionally, the

compressibility of the nitrogen liquid and vapour is neglected which is likely to have a significant influence on the flow densities.

The jet dynamics of cryogenic fluids, using CFD has been investigated extensively for the injection of liquid nitrogen in rocket combustions chambers (70-72). The turbulence flow under critical conditions was investigated by Reynolds-averaged Navier-Stokes (RANS) turbulence models and large eddy simulation (LES). LES is achieved by the direct numerical simulation (DNS) approach, which is too computationally expensive for practical engineering systems that involve complex flow and geometry. However, it can be used to model different parts of the flow field with different complexities depending on the level of turbulence. RANS models are based on average time equations of motion, which make it difficult to monitor the time-dependent variation of the velocity field. Majority of these models still rely heavily on validation from experimental and empirical data, which makes them highly susceptible to error when there is insufficient experimental work. The $\kappa - \epsilon$ model is often used as a good compromise between accuracy and complexity of the CFD problem, solving transport equations for turbulent kinetic energy(κ) and dissipation rate (ϵ) (58, 59).

2.4.2.2.1 VOF model

The Volume of fraction (VOF) model is commonly used in transient simulation such as injections because of its ability to track and model the interface between two immiscible fluids through time. It is specifically designed for applications where the interface between two or more immiscible fluids is of interest. It uses a single set of momentum equations that is shared by the fluids and each volume fraction of each

fluid is in each cell is tracked through the entire domain. In each control volume, the volume fractions of each phase sum up to unity (Equation 2.16). However, the cells are filled with a single phase unless located at the interface, where it is modelled linearly using the volume fraction and its special derivatives. The continuity equation is solved for each phase and used to track the interface sustained by the mass transfer between secondary phase q and n other phases (Equation 2.17). The momentum and energy equation are solved over the entire domain, where temperature and energy are mass averaged variables.

$$\sum_{q=1}^{n} \alpha_q = 1 \qquad 2.16$$

$$\frac{\partial}{\partial t}(\alpha_q \rho_q) + \nabla.(\alpha_q \rho_q \vec{v}_q) = \sum_{p=1}^{n} (\dot{m}_{pg} - \dot{m}_{qp}) \qquad 2.17$$

where p is the primary phase

A study (1) on the injection of liquid nitrogen into water using the VOF model showed that model did not account for the heat transfer between the phases, owing to the collective treatment of the energy equation across the domain. The simulations showed that the increased complexity of the interface and the extent to which it was tracked, was highly dependent on the grid size and the computational capability. The formation of the bubble required that it contains at least 8 cells, thus placing a limitation on the size that could be modelled.

The mixture model has been used as an alternative to study the equilibria between vapour and liquid mixtures(73) however, the phases are treated as interpenetrating continua and the model solves momentum, continuity and energy equations for the mixture and not the individual phase.

2.4.2.2.2 Eulerian model

The immiscible version of the full two-fluid Eulerian model was used to study the dynamics of liquid nitrogen injection in water(1). Momentum, energy and continuity equations are solved for each phase along with tracking of fluid interfaces. With more equations to solve, the model requires more computational power but with improved accuracy. Results showed the existence of a liquid core within the jet that spreads on impact with the water surface and the formation of a vapour layer that inhibits contact with the water. The model also provided more accurate results by interoperating source terms which contain a drag function representative of the relative velocities(1). However, these were not easily applicable or useful if the interphase drag laws for the system are unknown.

2.5 Chapter summary

Indirect heat transfer methods in the cryogenic engine were found to have low efficiencies, due to their reliance on the performance of heat exchangers. Direct injection was introduced to augment the heat transfer by increasing the contact area and temperature difference between the two fluids. This has since then stimulated research to further our understanding of the complex heat transfer mechanisms involved.

Initial studies showed that the accurate control of the injection and heat transfer is fundamental to the operation of the engine. Despite the extensive knowledge of fuel injection in conventional engines, that of the cryogenic engine is relatively elusive. Higher heat transfer capabilities with the direct injection of nitrogen in its liquid state have been reported however, the underlining and governing phenomena are yet to be well understood. Therefore, before predictions of the engine performance can be made, high quality, reliable experimental data is needed for comparison and certainty.

The start of art has provided a fundamental insight into the injection process however, the range and scope of the research have been restricted by the lack of control of the injection process and inadequate design of experiment. This was mainly due to difficulties involved with working with liquid nitrogen at high pressure, which brought into question the repeatability and ultimately the reliability of the results.

Therefore, with effective control of the injection process, this thesis aims to investigate the influence of injection parameters, especially valve timing, on the pressure build up inside the engine cylinder that is missing in current literature.

CHAPTER 3

3 Development of a liquid nitrogen injection rig

Amongst the different possibilities, the direct injection has been recognised as the most effective way to enhance heat transfer needed for the expansion of nitrogen and increase engine output.

To further our understanding of the complex injection process, Chapter 3 presents the development of a system commissioned to inject liquid nitrogen into water. This chapter presents the challenges that have limited experimental work in this area and difficulties in designing such a system. This is followed by a description of the test rig developed and the methodology used in designing it. Finally, the method of commissioning the system is described through a series of base line tests to determine its operating capability.

3.1 Challenges

The injection is one of the most important processes of the engine operation as it controls the quality and quantity of nitrogen injected, and inherently the resulting pressurisation rates.

However, there is limited work on the injection of liquid nitrogen into water due to the challenges associate with developing such a system. These challenges include:

I. Maintaining a low injection temperature:

At ambient pressure nitrogen only remains a liquid up to 77K. Hence, this poses a significant engineering challenge to minimise any heat transfer from the

surroundings, such to prevent any premature vaporisation of the nitrogen prior to injection.

II. High injection pressure:

To achieve the required engine output, a higher injection velocity is needed to increase the volume of nitrogen admitted to the cylinder that expands to drive the piston(21). However, this necessitates the pressurisation of nitrogen supply, which in turn raises its temperature. Hence, further sub-cooling is essential in order to keep the nitrogen in its liquid state.

III. Optimal valve timing

The valve must be opened long enough to allow for the adequate mass of nitrogen to be injected into the engine. However, if the valve is left open too long then the pressure in the engine will exceed that in the injector, causing the back flow of liquid nitrogen in the feed line.

Injection of the liquid nitrogen occurs just after top dead centre (TDC). However, one must still consider that there are optimal temperatures and pressures at which the nitrogen must be injected to achieve the maximum engine output. Therefore, an automated system where the valve timing was dictated by monitoring the temperature and pressure of the liquid nitrogen could significantly improve the output of an engine. To date, this has not been achieved.

3.2 Structure of injection test rig

The liquid nitrogen test rig was designed to perform experiments to investigate the influence of injection parameters on the expansion of the injected nitrogen and

ultimately the pressure rise in the engine cylinder. The design addresses the difficulties and limitations faced in previous work by making modifications and improvements to the delivery, sub-cooling, pressurisation and valve systems of the rig.

The experimental test rig is shown in Figure 3.1. It consisted of a single shot injector, a sub-cooling system, a hydraulic actuator and a small pressure vessel in which the nitrogen was expanded at a fixed volume.

Nitrogen was delivered from a 200 L Dewar to the buffer vessel via a vacuum insulated hose at 2- 3 bar. The double walled buffer was simultaneously cooled by a secondary flow of nitrogen from the Dewar while it was filled. Compressed gas from a gas bottle at 100 bar was used to pressurise the liquid in the buffer as it continued to be sub-cooled.

The injection temperature was controlled by the addition of a sub-cooling system during the pre-pressurisation of the liquid prior to injection. This occurred in the buffer vessel where the flow in its cooling jacket removed heat from the pressurised nitrogen in the vessel. A valve at the buffer was used to control the secondary flow to the buffer, allowing for some control over the cooling rate. Therefore, a larger 200 L Dewar was required to supply and store enough nitrogen for the injections, sub-cooling of the buffer and purging the system.

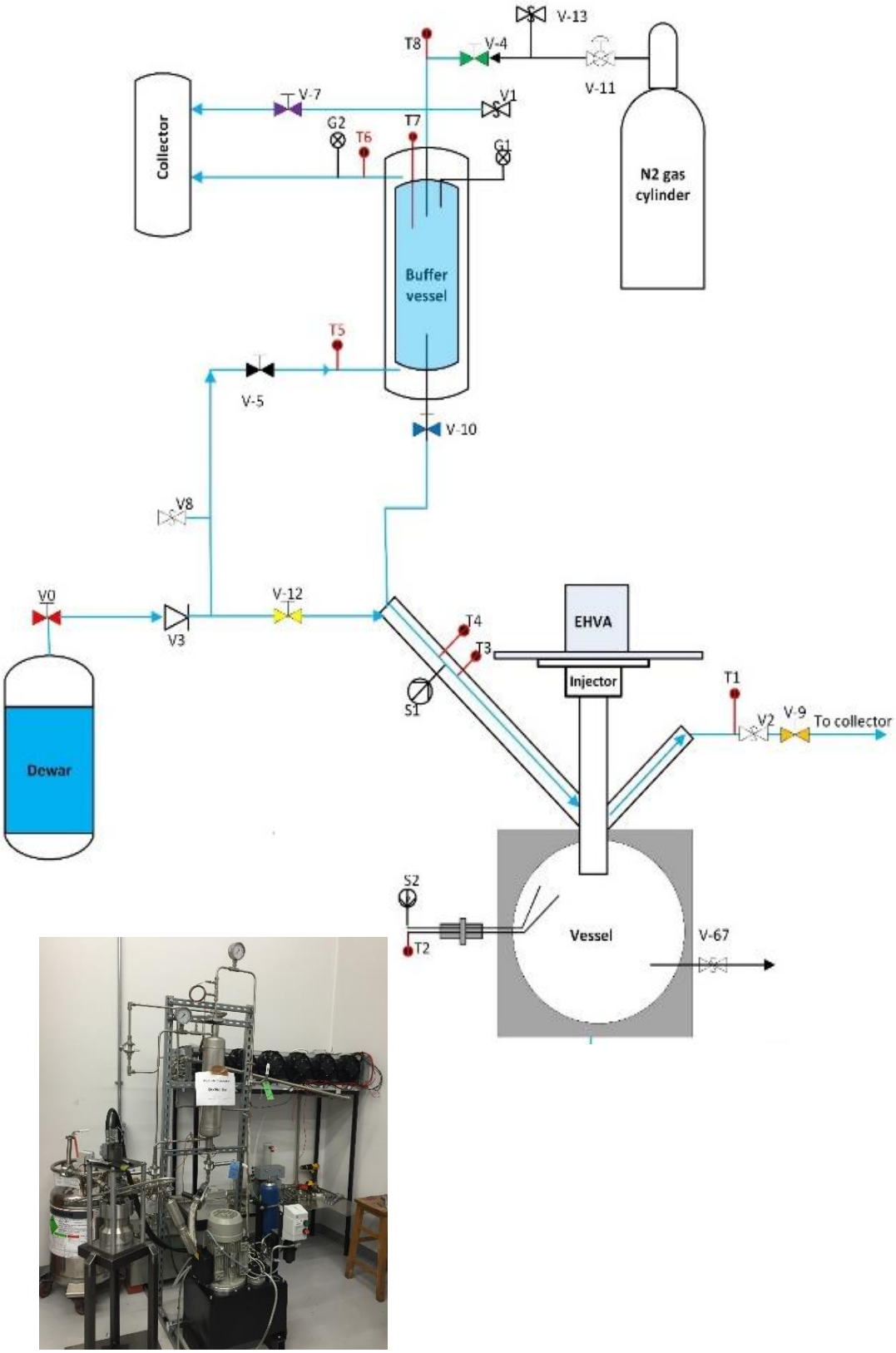

Figure 3.1: Schematic and picture of the liquid nitrogen test rig

A manual valve was used to deliver the pressurised subcooled nitrogen to the injector inlet. A pressure transducer and thermocouples at the inlet were used to closely monitor and recorded the injection pressure and temperature prior to injection. Therefore, the thermodynamic state of the nitrogen was known prior to injection.

The pressure vessel was a stainless-steel cylinder of 85 mm in diameter. The vessel was designed with an adjustable piston to vary the internal volume of the vessel. Two rapid response pressure transducers and a thermocouple were used to monitor the pressure rise and temperature variation within the vessel. Water was added to the vessel via the fill plug and removed via the HEF outlet found inside the piston rod. During testing, water was not reheated but simply replaced so as to maintain it at room temperature.

The injector was made of a stainless-steel poppet valve with a seat diameter of 26 mm. The poppet valve was used to increase the contact area needed to optimise the direct contact heat transfer in the engine. The opening and closing of the valve were controlled by an electro-magnetic hydraulic valve actuator system (EHVA).

The actuator was triggered by the operator using a simulated pulse generated within the LabVIEW programme. The injection period was dependent on the width of the pulse and was manually set by the programme.

For safety, all pipework was directed to a collector tank for the expansion of the liquid nitrogen and avoid the release of the pure liquid through the laboratory extraction system. The entire rig was fitted with five relief valves set to accommodate for any

trapped and expanding liquid nitrogen that would otherwise cause catastrophic damage.

Heat transfer to the nitrogen was addressed by the use of vacuum insulated pipes and the additional of rubber nitrile insulation on all the apparatus. Before testing, liquid nitrogen from the Dewar was delivered to the rig to purge the entire system with the cryogen. This was necessary to remove any trapped air, and to reduce the large temperature gradient across the pipe diameter.

The temperature and pressure of the nitrogen throughout the entire system was continuously monitored by highly responsive transducers and thermocouple capable of handling cryogenic temperatures. The addition of sub-cooling increases the range of injection pressure for the experiments, which had been a challenge in the past.

The EHVA was controlled by a servo valve mechanism that uses its own measured output to accurately match the demand signal. This minimises the effect of errors or anomalies within the control system itself, as well as the load. It also offered greater and precision control of the valve position with a rapid response to changes in speed, direction or frequency. Subsequently, the rig allowed for the timely and controlled opening and closing of the valve. Further detail and specification of the valve is explained in Section 3.1.4 below.

3.3 Test rig equipment

The main apparatus of the test rig consisted of the injector, pressure chamber, buffer vessel and the EHVA. The injector and pressure chamber were provided by Dearman Engine Ltd where the design went through several iterations to improve the flexibility

and pressure capability of the rig for testing(26). They were designed to replicate the features of the actual engine in order to have comparable results.

3.1.1 Buffer vessel

The 5-litre stainless-steel vessel shown in Figure 3.2 below was designed for the pressurising and sub-cooling the nitrogen pre-injection. It consisted of a cooling jacket, which allowed for continuous flow of low-pressure liquid nitrogen around it during the experiments. The secondary flow was used as a heat sink to the pressurised nitrogen and was used to maintain its temperatures below saturation.

The liquid nitrogen inside was pressurised by the addition of nitrogen gas from a gas bottle via a regulator. Increase in the injection pressure had an adverse effect on the temperature, which necessitates further sub-cooling prior to injection.

The temperature was monitored by two thermocouples positioned at the top and halfway, to measure temperatures at different points inside the vessel. The vessel was full when temperatures at the top were below saturation at the given pressure.

While a small cryo-pump may be used as an alternative, the complexities involved in maintaining low heat transfer and flow quality are not considered worth the benefits of enhanced flow control for this type of testing.

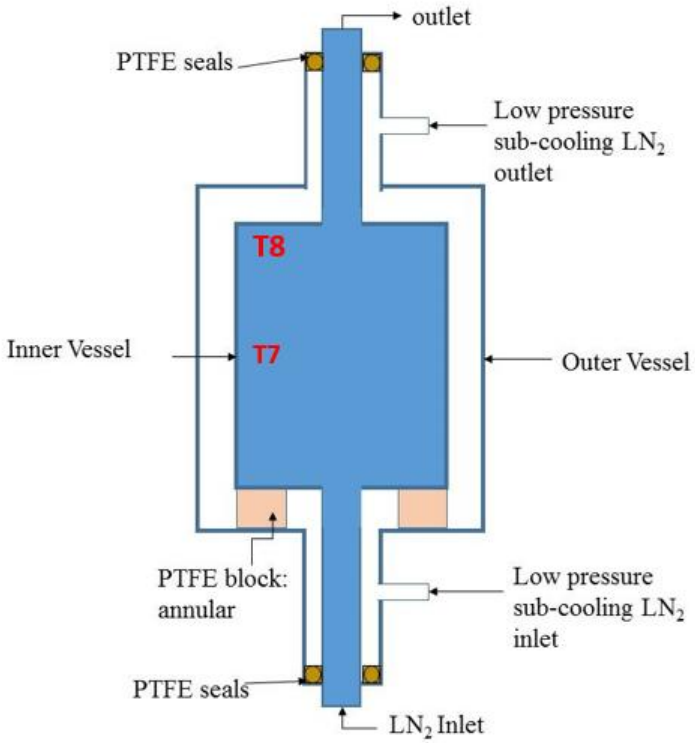

Figure 3.2: Drawing of the fabricated buffer vessel

3.1.2 Pressure vessel

The pressure vessel shown in Figure 3.3 is a hard-stainless-steel block with a bore diameter of 85 mm and a volume of 560 ml. Its walls were 10 mm thick walls to withstand a working pressure of 250 bar however, it was fitted with a relief valve in case this pressure was exceeded.

The variable piston can be used to vary the clearance volume, but it should be noted that the piston does not move during the expansion stroke like in the actual engine. It was kept in a fixed position (400 mL) throughout testing and the clearance volume was varied by the volume of water added.

Figure 3.3: Picture of the pressure vessel and the piston

3.1.3 Injector

The injector shown in Figure 3.4 consisted of an angled inlet and outlet that so as to reduce the pumping work at the inlet, whilst increasing it at the outlet. This increased the flow at the inlet whilst preventing the nitrogen from flowing out of injector too quickly. The inlet feedline was 4 mm longer in order to allow for the establishment of a steady flow, before the valve is opened, and nitrogen is released into the vessel.

Figure 3.4: Picture of the injector and its components

Heat transfer in the injector inlet was restricted by the vacuum jacket surrounding the inlet. A vacuum pump was used every week to reload the insulation in the injector.

A spring mechanism on the head of the injector provided an added force to close the valve against the injection pressure in the inlet.

3.1.3.1 Poppet valve

The poppet valve provided a large flow area with minimal movement. It also had good sealing properties and its simple design making it easy to fabricate and manufacture. Poppet valves travel a minimum distance whilst capable of high flow rates which in turn increases their response times(74).

The valve was also made of hard stainless-steel for its advantageous low thermal shrinkage properties and hardness that remain consistent at cryogenic temperatures. Ultra-high-molecular-weight-polyethylene (UHMWPE) was used to make the valve seat that was pressed onto the stepped base of the valve.

The thermoplastic material was used for its lightweight, high impact strength, good abrasion resistance and good ductility (75, 76) with the purpose of sealing the valve when closed. At cryogenic temperatures, the occurrence of thermal shrinkage in the injector was very likely, resulting in a leak when the valve was closed. At low temperatures, the hardness and friction coefficient of the plastic increases and begins to display characteristics of fatigue and abrasive wear(77). The increased hardness is attributed to the closely packed microstructure at low temperatures,

hindering the movement/slip of the molecular chains. The ductility of the material can be lost, thus reducing its ability to absorb energy during compressions.

The UHMWPE also reduced the wear resulting from impact during the valve movement. Although its fatigue life cycle at low temperatures is still under investigation, the seat did not demonstrate any sign of deformation and remained intact during all the tests.

A two-part cryogenic epoxy adhesive (EP29LPSPAO) was used to bond the valve seat to the poppet valve, which assisted in sealing the valve. The adhesive was cured for 24 hours at 80 °C and before testing, the valve was checked for leakage using both high-pressure gas and liquid nitrogen.

3.1.3.1.1 Flow area

The geometric flow area of the valve, also known as the throat area was obtained as the surface area of a conical frustum (Figure 3.5), where the height of the frustum was the distance between the valve and the seat. The maximum geometric flow area was calculated to be 656.1 mm^2 using Equations 3.1 and 3.2.

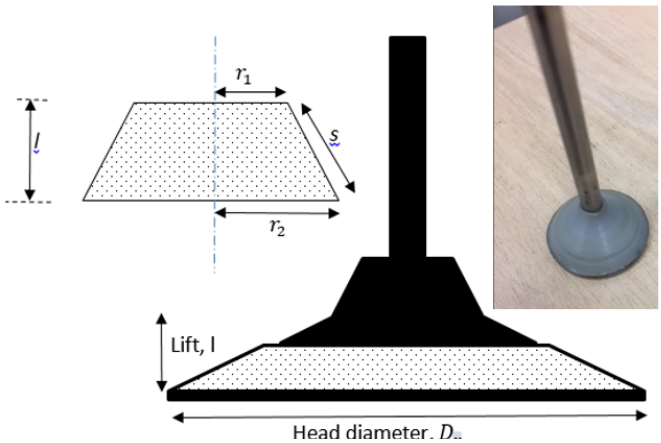

Figure 3.5: Dimensions frustum of the poppet valve

$$s = \sqrt{(r_2 - r_1)^2 + l^2} \quad 3.1$$

$$A = \pi(r_1 + r_2)s \quad 3.2$$

The movement of the poppet valve was controlled by the actuator. The actuator pushed down on to the head of the injector with a 0.3 tonne newton force causing the valve to open. A coupling mechanism shown in Figure 3.6 was designed to allow the EHVA to transmit a force normal to the head of the injector, which would align with the valve. The piston of the actuator was held by split collets that are compressed between two split circular disks. The top disk was bolted to the bottom disk that was connected to the injector head via three triangulated screws.

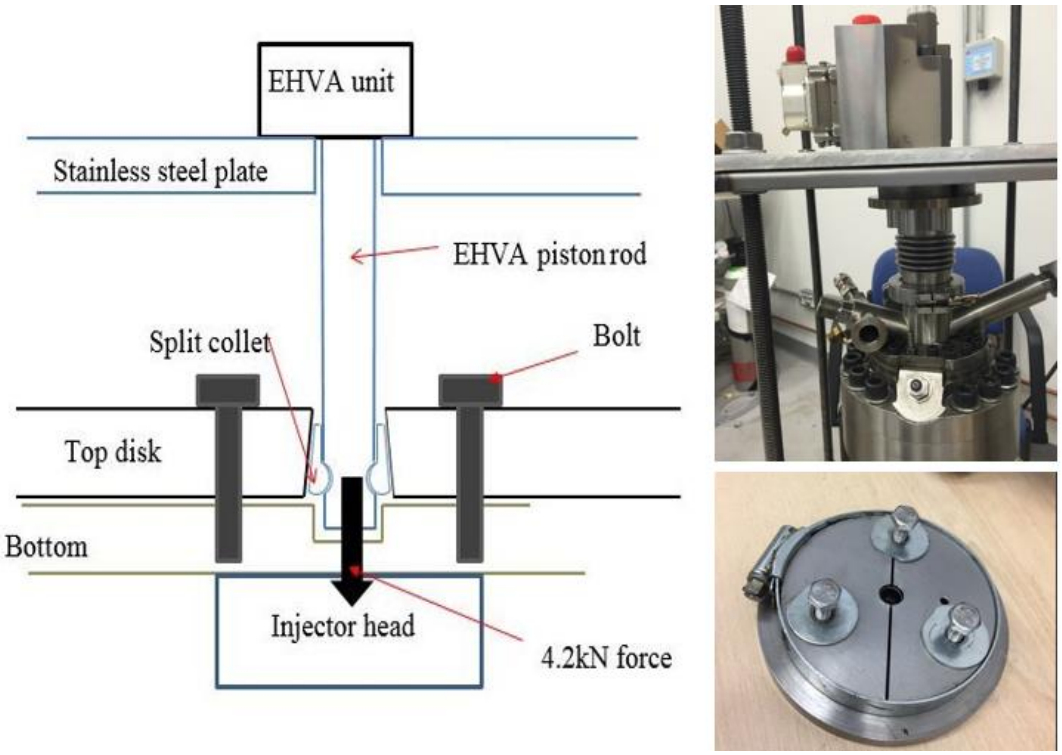

Figure 3.6: Schematic and picture of the hydraulic valve coupling mechanism to the injector

3.1.4 EHVA system

The EHVA system used a hydraulic drive mechanism which, in contrast to electric motor drive systems, provides a smoother performance at low speeds and has a wide speed range without special control circuits. Secondly, it has a substantially higher power to weight ratio and is less expensive for a system operating at relatively high horsepower(2).

3.3.1.1 Hydraulic system

The hydraulics were powered by a hydraulic unit shown in Figure 3.7. It consisted of an electrical motor, a 5 l/min speed pump, a 30 litre oil tank, a 2 litres accumulator mounted on the frame support and a bypass damper for safety. It was used to store pressure that was released or absorbed in order to smoothen out pulsations in the valve. A temperature gauge is incorporated to monitor the oil temperature. This was due to the high fluid temperature caused by constant pumping that could result in

Figure 3.7: Picture of the large hydraulic pumping system for the actuator

mechanical failure. The system had a maximum operating oil pressure of 275 bar, which was used to vary the hydraulic force applied.

The servo valve required a well-designed control system, in order to promptly and accurately open and close the valve in response to the demand signal. The actuator was controlled by a closed-loop servo drive mechanism. The servo valve provided an interface between the electrical input signal and hydraulic power to drive the mechanical action. This type of control system is predominately used in applications where high performance is required to control physical quantities such as force or pressure using a voltage or current.

A feed-forward closed loop control system was used as shown in Figure 3.8. The closed-loop drive mechanism measures its own output and forces the output to quickly and accurately follow the demand signal, which eliminates the occurrence of errors that may result from the load or any external disturbances(2). The servo valve controls the flow rate for the hydraulic actuator based on the input electrical signal.

The servo output (position of the load) was measured and converted to an electrical signal by a position DVRT. The error established from a comparison with the demand was amplified and used as a new input control to the servo valve.

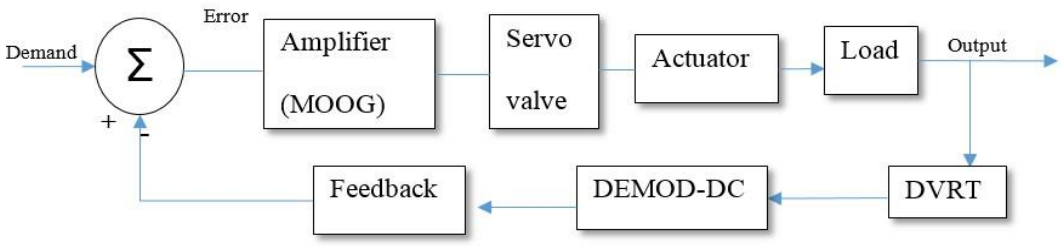

Figure 3.8: EHVA servo control mechanism

The fluid flow to the actuator was in proportion to the drive current from the amplifier forcing the load to move. A change in the demand signal (either speed or direction of movement) read like an error, causing the load to move accordingly to eliminate the error signal. The gain was kept high to match the output to the demand rapidly and accurately.

The robust EHVA provided a much-needed control of the valve closing, going against spring forces and pressure gradient. The minimum open time was limited to 3 ms due to the mechanical limitations of the valve speed.

3.1.4.1 Hydraulic servo valve

The servo valve (Figure 3.9) controls the flow rate for the hydraulic actuator based on the input electrical signal. A magnetic force is induced by the electrical current on the armature creating a torque. The torque rotates the flapper to close one end of the nozzle while opening the other, thus changing the flow in the hydraulic amplifier.

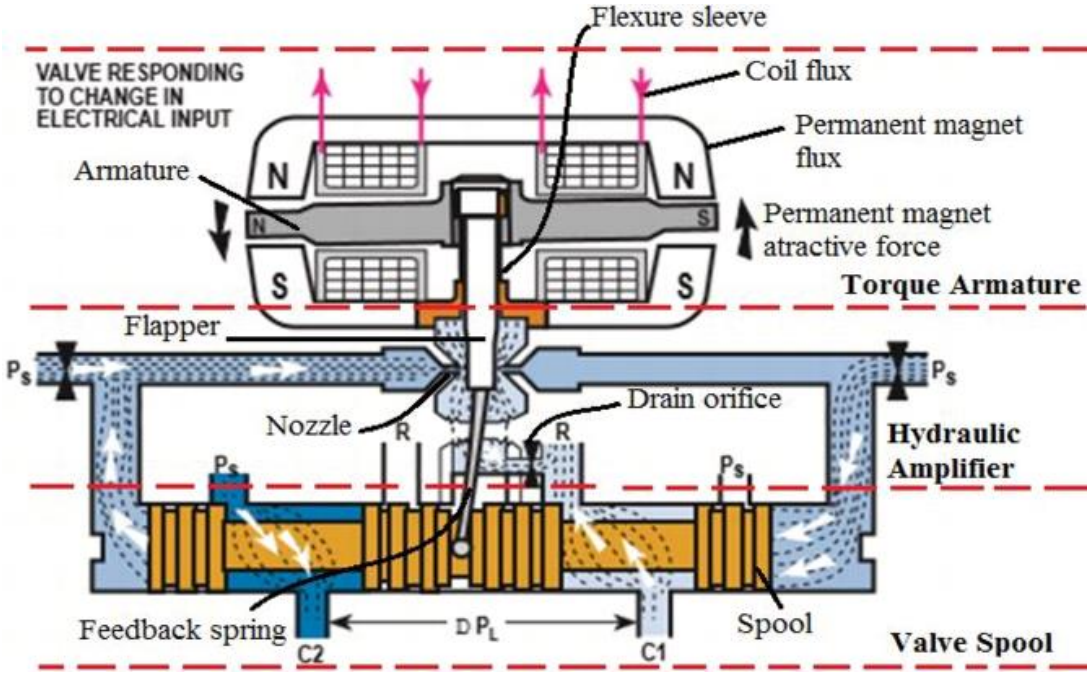

Figure 3.9: Diagram of the servo valve(2)

The altered flow goes through the drain orifice to the return line, which creates an imbalance hydraulic force on the spool. This causes the spool to move in one direction, which opens the pressure port allowing the main oil to flow to the actuator. The force generated by the feedback spring as a result of the spool movement helps the armature and the flapper to return to its original position when the current is set back to zero(78).

The actuator responds to the input signal, with the conversion of fluid pressure into the movement of its own piston rod. This applies a large axial force onto the head of the injector, which is transmitted to the poppet valve As a result, the poppet is pushed down to allow the cryogen to flow into the vessel; also known as the forward stroke.

A large force was needed to allow the valve to move independent of any pressure or forces upstream and downstream, during both the forward and return strokes of the valve. For the forward stroke, the force had to overcome the spring forces and the pressurised liquid nitrogen in the feedline. During the return, the pressure builds up in the vessel coupled with the spring force was most likely to shut the valve a lot quicker than desired. Furthermore, the large force was needed to maintain the seal at the valve when it was closed.

The position of the actuator was measured by a differential variable reluctance transducer (DVRT), with an accuracy of 1.5 %, and ready by the Data Acquisition system and recorded by the computer running LabVIEW software. The 14-bit DAQ

device provides a voltage resolution of 10^{-2} mV per bit and based on the LVDT calibration, the valve lift could be adjusted to the nearest mircrometer.

3.1.5 General Instrumentation

Extensive instrumentation was necessary to monitor the nitrogen at the various stages in the rig. Temperature and pressure were essential for the analysis of thermodynamic state, flow, and heat transfer of the cryogen at key points of the rig. Instrumentation points are shown on the system in Figure 3.1 in Section 3.2.

3.1.5.1 Temperature

The temperature was recorded by T-type thermocouples because of their good accuracy and reliability even at cryogenic temperatures and have an accuracy of ±0.5 K. Eight stainless-steel insulated 0.5 mm dashpot probe thermocouples were used. The mineral insulated probe enables the sensors to be bent or twisted into the flow pipes without impairing their performance.

The probes were installed via stainless-steel compression fittings to prevent leakage due to the high pressure in the system. The injection temperature was a vital aspect of each injection and therefore two thermocouples were placed in the injector inlet and another at the outlet so as to monitor any temperature variation during the injection. These provide vital information of the flow densities across the injector, which would ultimately affect the injected mass.

3.1.5.2 Pressure

Pressure measurements were taken in the chamber as well as the injector. Two types of piezo-resistive transducers were used in the experiments.

The Kulite transducers (CT-375 (M) SERIES) with an operating range of up to 70 K, made them ideal for cryogenic temperatures in the feed pipe. Pre-calibrated to an accuracy of ±0.04% (0.1 bar), they provided stable pressure readings during testing.

It was thought useful to include another transducer to measure the rapidly dynamic pressure in the chamber, which was inserted into the piston head. The Kistler pressure transducer (Type 601CA) was also pre-calibrated, to an accuracy of ±0.03 %, giving maximum ±0.08 bar error within the 0 - 250 bar range.

3.1.6 Data Acquisition System

The Data Acquisition System (DAQ) was used to monitor, record and analysall the electronic signals from the sensors on the rig. All the thermocouples were connected to a NI-9213 temperature input module. A maximum data acquisition rate of 100 S/s (samples per second) was available on the channels. The NI9213 includes anti-aliasing filters, open-thermocouple detection, and cold-junction compensation giving it a high-accuracy of ± 0.25 K.

The transducers and LVDT were wired to a NI USB6001 block connected to the PC and data was logged at 2kS/s. This device was also used to generate the analogue signal that controlled the EHVA, which was modified in the LabVIEW programme.

3.4 Commissioning of the test rig

Preliminary tests were conducted to get familiar with the operation of the test rig, especially to determine the level of sub-cooling possible and the attainable injection temperatures. Secondly, these tests were necessary to understand and fine-tune the valve response and its movement. Accordingly, the test rig was characterised by:

- The highest injection pressure attainable
- Temperatures at 8 locations throughout the rig
- Temperatures at the injector inlet and the heat gain within the injection feedlines
- Highest chamber pressure
- Various valve actuation parameters such as lift, frequency and timings

3.1.7 Valve actuation

These tests were conducted to grasp and get familiar with the operation of the EHVA and its response to the simulated input signal, so as to open the valve in the shortest interval without compromising the flow area.

3.1.7.1 Demand profile

The actuator was given a 0 – 1 V, in which it moved a maximum distance of 1.2 mm based on reading from the DVRT.

Three input waveforms were tested to establish the valve movement in the quickest possible time and to get a better understanding of the valve's response.

As shown in Figure 3.10, a square wave resulted in a better and smoother movement. The triangular wave was inadequate for the control of the lift due to the lack of a dwell period, which permits the valve to catch up and stay open long enough before it was asked to close. A 10 ms triangular wave signal resulted in a 0.626 mm lift in comparison to the 1.222 mm achieved with the square wave of the same duration.

A delay (dead time) between the demand and the movement of the valve was observed. This can be caused by the slow response of the LDVT to the control command or, a delay caused by the flow of hydraulic fluid in the actuator.

Tuning of the PID control was carried out to produce the required performance. The potential gain was increased to make the system faster, but only so far as to avert instability. The integral was tweaked to reduce the steady-state error and stop oscillation but inevitably increased the overshoot. Although some overshoot is needed to for a fast system to respond to changes immediately, there was a need to trade off the speed of the control system with its accuracy to better meet the requirements of the injection.

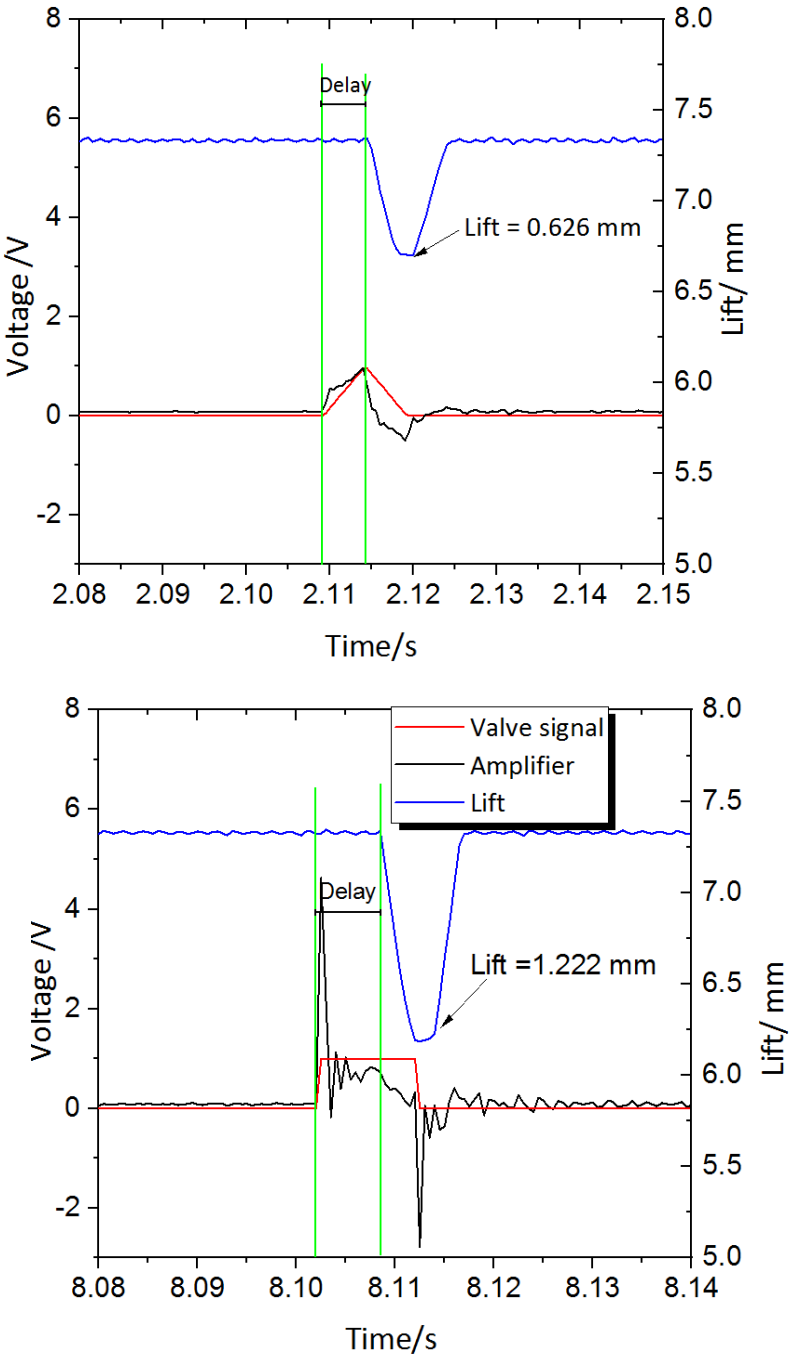

Figure 3.10: Valve lift profiles for a triangular (top) and square (bottom) input signal

3.1.7.2 Injection frequency

Several frequencies were tested, and the maximum operating frequency was limited to 20 Hz (Figure 3.11). Any higher and vibrations bought on by the force of the piston could have caused damage to the injection and also compromise the stability of the rig.

The observed delay discussed in section 3.1.7.1 remained constant and was found not to vary with frequency or injection duration.

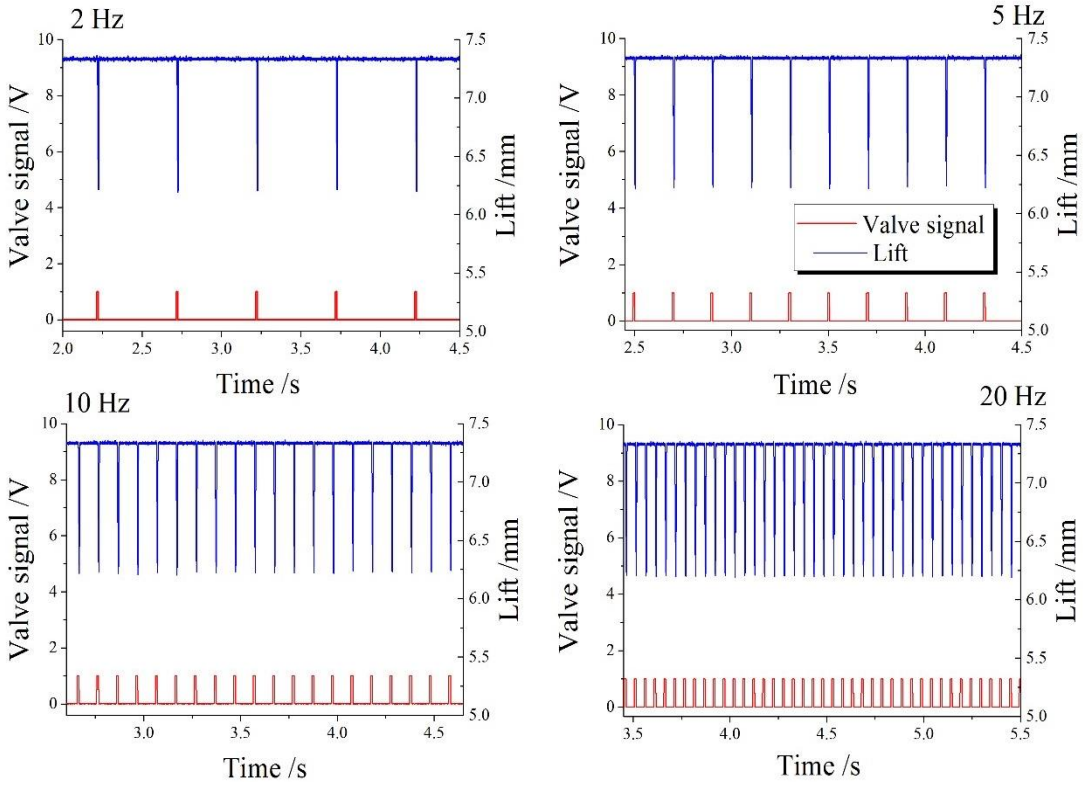

Figure 3.11: Test of a variation of frequencies 2,5,10 and 20 Hz.

3.1.7.3 Valve lift

The lift was controlled by the length of the dwell in the input signal as shown in Figure 3.12. To attain the maximum lift, a signal greater or equal to 10 ms was required. For

a longer pulse, the valve stays open at its maximum lift for longer before commencing the return stroke.

The valve lift was verified by the use of a proximity sensor placed beneath it. The piston in the vessel was removed for this set of experiments and the results were used in the recalibration of the LVDT.

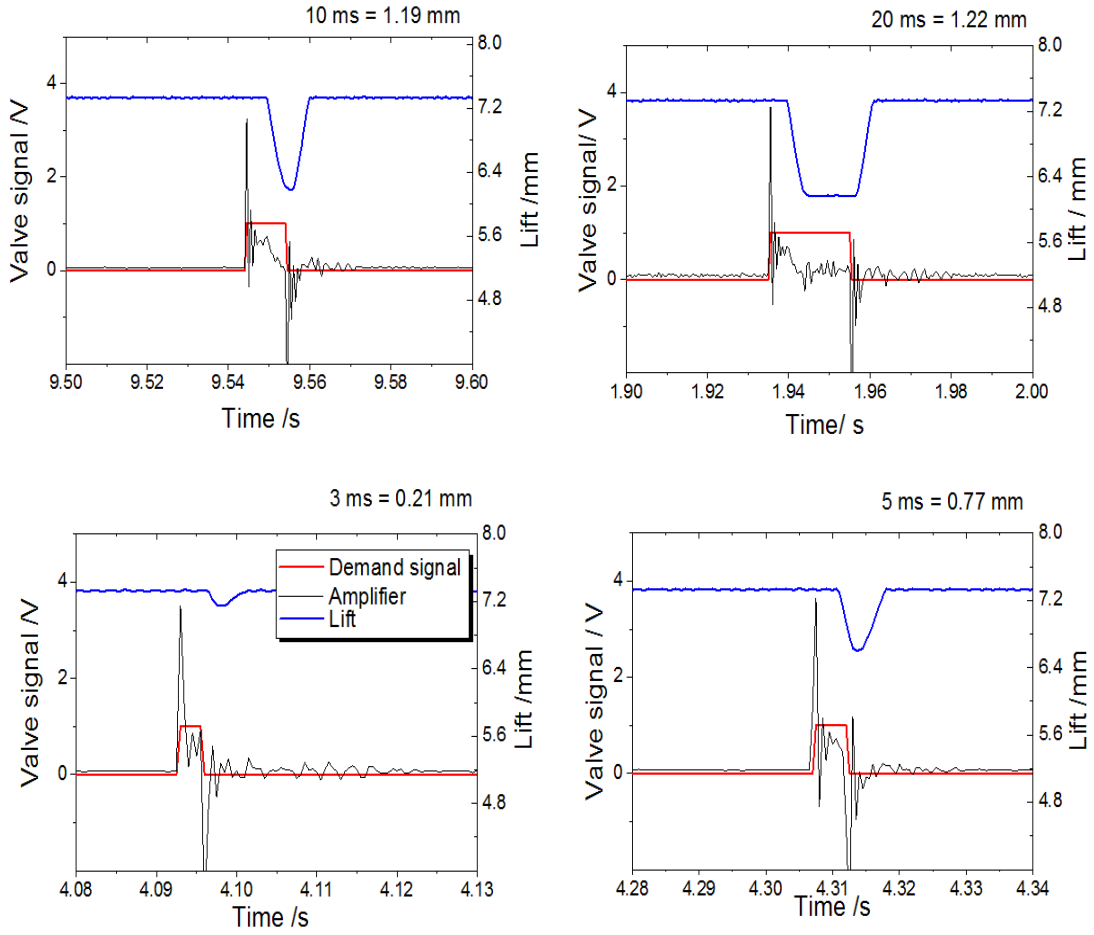

Figure 3.12: Valve profile for increasing injection duration

3.1.8 Temperature

Table3.1 shows a table of thermocouples and where they are located on the rig.

Table 3.1: List of thermocouples and their location

No.	Location
T1	Injector outlet
T2	Pressure vessel
T3	Injector inlet
T4	Injector inlet
T5	Sub-cooling inlet
T6	Scub-cooling outlet
T7	Buffer (liquid)
T8	Buffer (gas)

Before injection, steady flow in the injector feed line was monitored by thermocouples T3 and T4 at the inlet and T1 at the outlet. A large temperature difference between these three indicated a high heat transfer to the liquid. The temperature at the buffer and the injector inlet varied ∼25 K, despite the use of a vacuum insulated pipe. This was reduced to ∼15 K by the addition of extra lagging to the piping and the continuous use of the vacuum pump for the vacuum jacket throughout testing.

There was still a ∼10 K difference between T3 and T4 in the injector inlet prior to injection, which was not considered acceptable for the tests.

Accordingly, the outlet valve was opened to allow the flow of nitrogen across the injector thus reducing the variation at T3 and T4 to < 5 K as shown in Figure 3.13. There is an immediate drop in T3 at the inlet as fully liquid nitrogen follows into the vessel and through the injector outlet.

During testing, the water temperature remained constant which was a similar observation in previous injection experiments (21, 22). On injection, the gas temperature, shown by T2 initially fell by ~2 K and gradually rises with the evaporation of the liquid nitrogen. It eventually reaches ambient temperature 3- 4 minutes later, when the pressure in the vessel plateaus, corresponding to no further heat transfer.

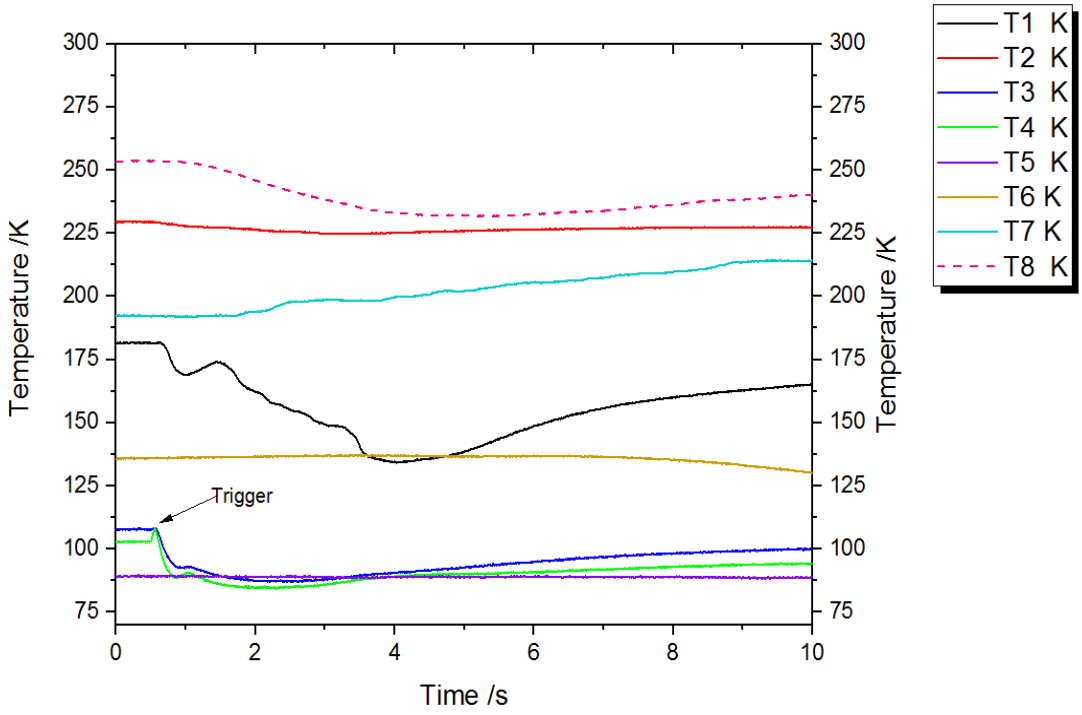

Figure 3.13: Temperature profiles in the injector inlet and buffer vessel during injection 12, before and after the valve is triggered.

The liquid nitrogen temperature in the buffer increases gradually as the nitrogen was discharged and the vessel begins to empty. The buffer was due for a refill when T8 was equal to T7 showing temperatures above saturation for the corresponding pressure.

Post injection, there was a slight oscillation in temperature at the inlet as the pressurised flow attempts to establish a steady-state. After 8.5 s, the needle valve at

the injector outlet was closed to prevent flow through the outlet causing the sudden rise in temperature to the confined flow on account of the insignificant heat transfer. With this procedure, injection temperature as low as 86 K were recorded during testing. A sub-cooling ratio $\left({}^{T_{inj}}\!/_{T_{sat}}\right)$ was used to quantify the degree of sub-cooling.

3.1.9 Injection pressure

There was an immediate pressure drop in the injection pressure when the valve was opened (Figure 3.14:) and gradually recovered as the valve was closed. A minimum injection pressure was recorded at the maximum valve lift and therefore, the recorded pressure was taken as an average over the injection duration.

During a pulsed injection cycle, there was a significant oscillation in pressure between pulses which was an indication of instability. The compressed gas in the gas bottle and the buffer was used to absorb the pressure oscillations, which resulted in the warming of the gas and demanded for a higher rate of cooling. Absorption dampers such as accumulators are most commonly used in such a situation however, with a less than 7% variation (Figure 3.15), the method implemented here was found to be adequate and effective.

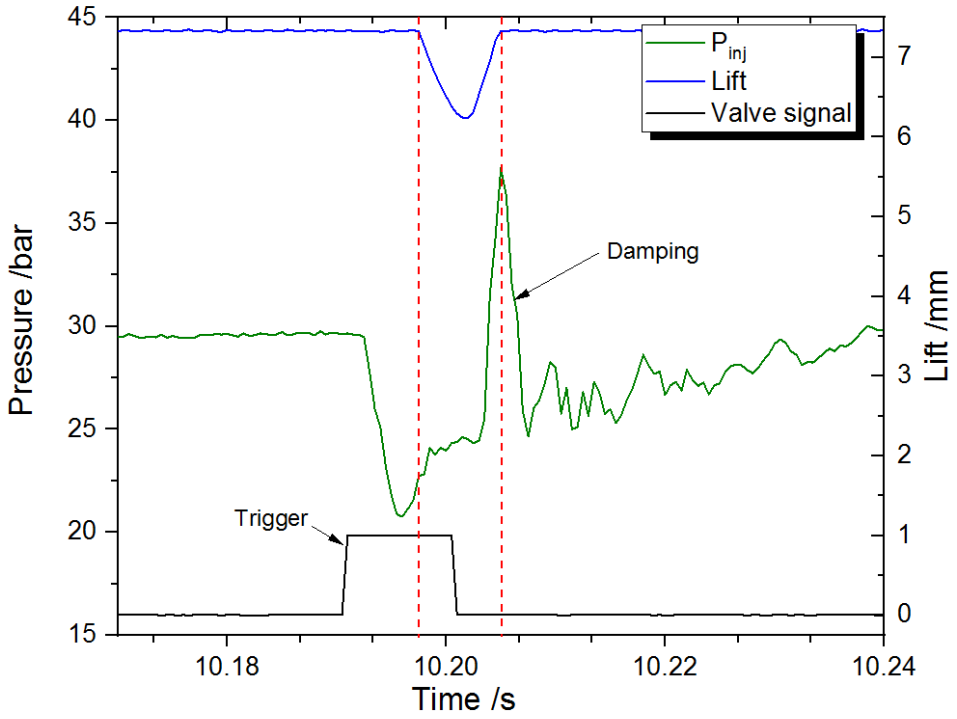

Figure 3.14: Pressure drop in the injector when the valve is opened for 10 ms

Higher injection pressure increased the flow across the valve resulting in immense pressure on the topside of the valve cap, which required a larger force to close and seal off the valve. Consequently, steady low levels of leakage before the valve was triggered to open were observed, due to the failure of the seal. The leak was found to be even more persistent at lower injection temperature and increased pressure due to the increased weight/force applied by the liquid.

The hydraulic oil pressure of the EHVA was increased to its maximum (275 bar) so as to adequately seal off the vessel. This was done in addition to tuning the zero position of the valve on the Servo Amplifier, to move past its end stop during closing.

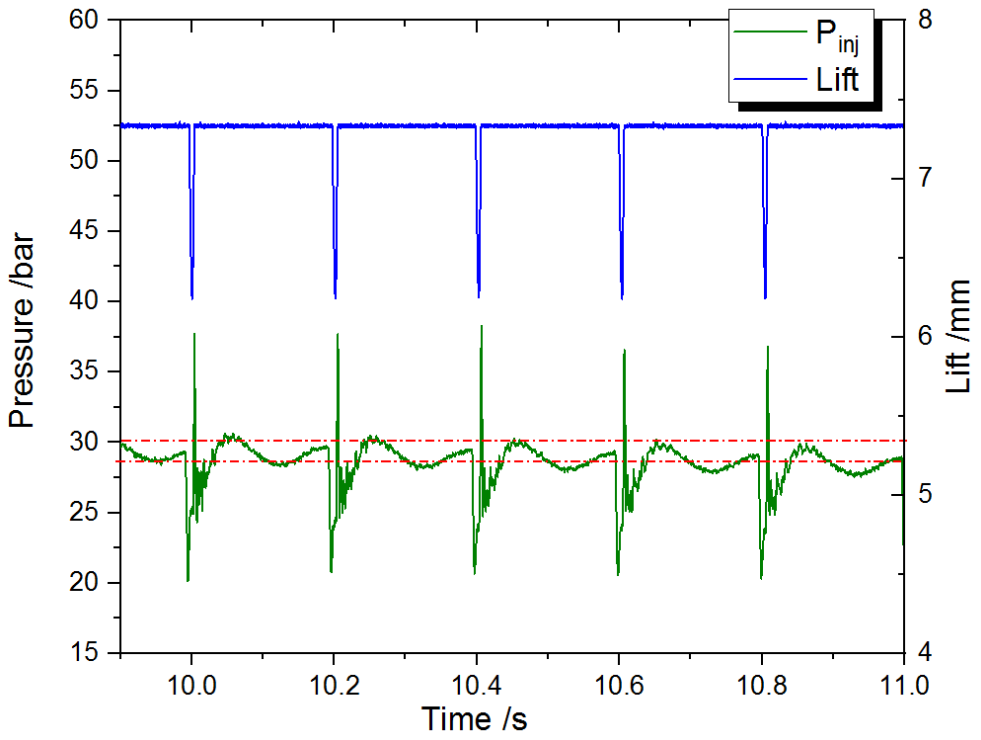

Figure 3.15: Pressure oscillation in pulsed injections reduced to <7 % using

3.1.10 Vessel pressure

The graph in Figure 3.16 illustrates the gradual pressurisation inside the vessel for a 2.2 s injection. Both Kulite and Kistler transducers were in good agreement throughout testing with a less than ± 0.25 bar difference in the recorded peak pressure.

A closer look at the graph shows a loss in pressure in the feed as the vessel pressure exceeds that in the injector. This occurred when the valve was left open for a longer duration. At this critical point, there was a slight depressurisation in the vessel and injector due to backflow in the feedline. On closing the valve, the pressure gradually builds up again and attained a maximum pressure as a result of the expansion of the injected nitrogen. These circumstances would compromise the pressurisation in the vessel and ultimately affect the reliability of the pressure gradient.

In all the experiments, the valve was closed prior to this critical point. Further investigation of an optimal injection duration was conducted and is present in Chapter 4.

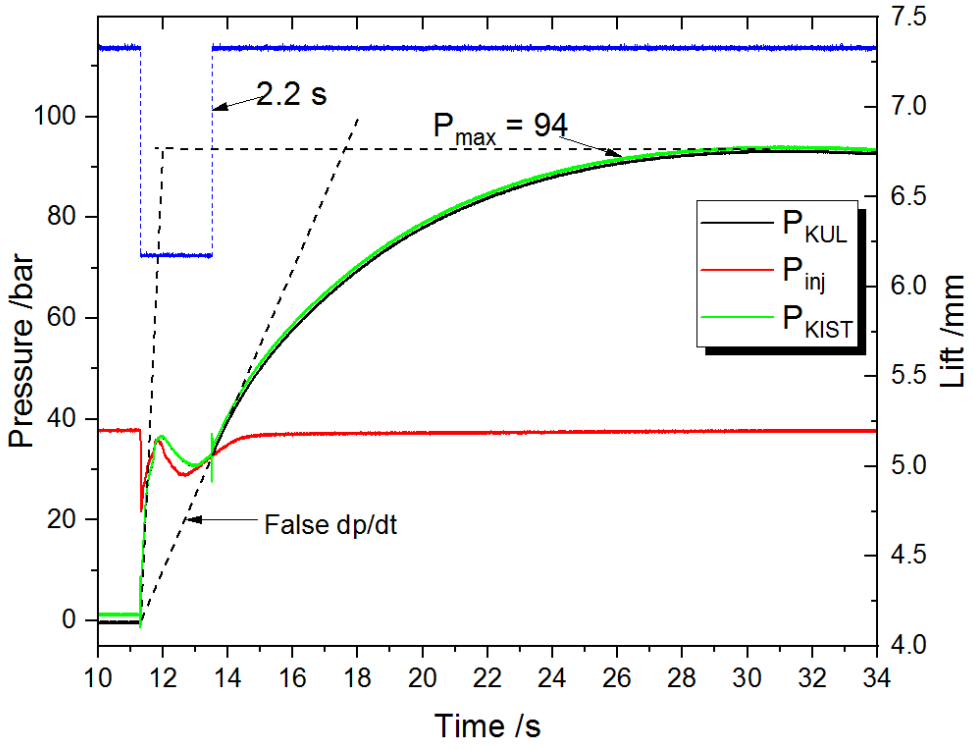

Figure 3.16: Kistler and Kulite transducers pressure profiles for the increasing vessel pressure

During testing, another pressure leak (~1 bar) in the vessel was detected just after the maximum pressure was attained as shown in Figure 3.17. Efforts were made to resolve/reduce this with the replacement of the silicon O-ring and application of PTFE thread seal between the injector and the vessel however, no improvements were made.

This observation could be due to the sudden change in pressure that results in a pressure wave within the compressible fluid. A similar event, known as the water hammer wave, is observed during the rapid closure of a valve. Studies have shown that the only way to resolve this is to regulate the speed at which the valve is opened

and close(79). This was not considered because it would compromise the valve speeds and timings aimed at in this study. After all, the pressure in the vessel continues to rise and held consistently over a 24-hour period with no indication of leakage from the vessel.

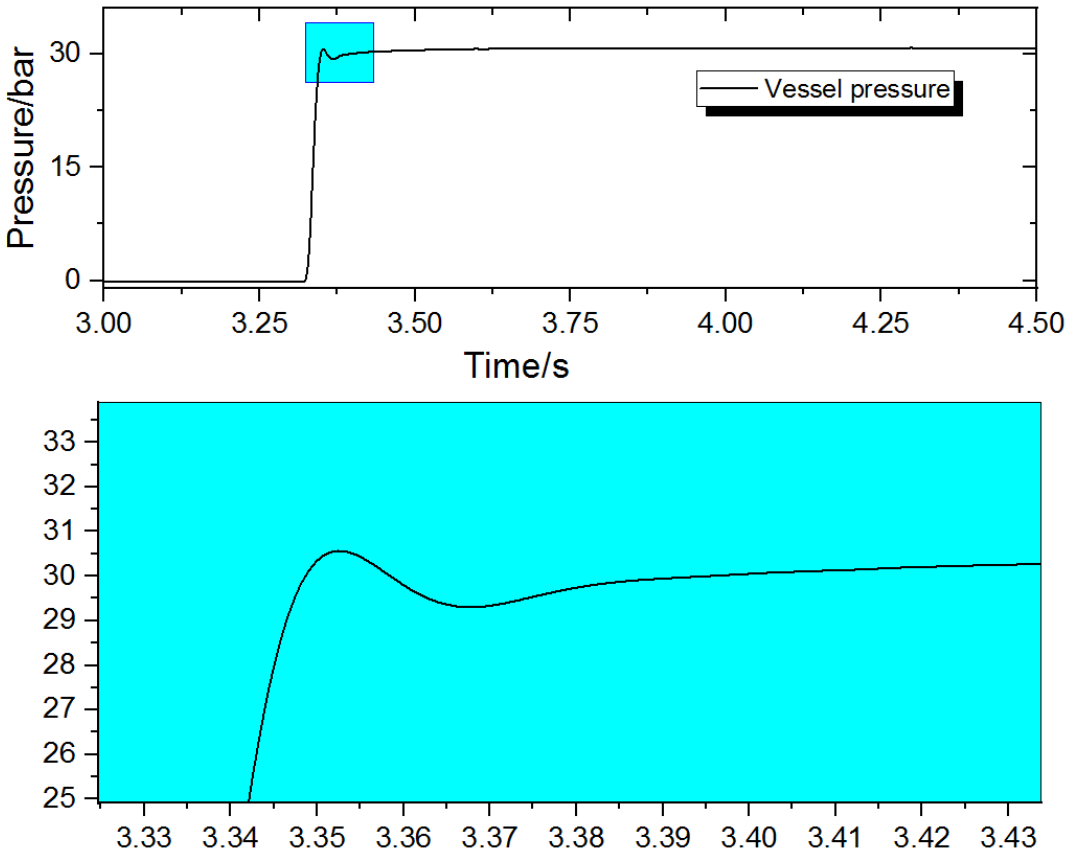

Figure 3.17: Pressure leak detected in the vessel

3.1.11 Repeatability

Pressurisation rates for tests 108, 111 and 112 for liquid nitrogen injected at 55 bar were compared to verify the repeatability and as such the reliability, of the experimental results. Figure 3.18 shows a relatively good repetition of the pressure curves with a standard deviation of 1.7 for the peak pressure which was because of

a ± 0.05 difference in the cooling ratio. So, although not identical there was still a good similarity, thus confirming the reliability of the results presented here.

3.1.12 Test rig restrictions

The test rig has some limitations due to the endurance of each piece of equipment therefore, the maximum operating parameters are given in Table 3.2 below.

Table 3.2: Maximum operating parameters of the injection rig

Parameter	Measured value
Maximum P_{inj}	96 bar
Maximum $\dot{m}$	6000 l/min
Minimum T_{inj}	86 K
Maximum valve lift	1.222 mm
Maximum P_{vessel}	180 bar

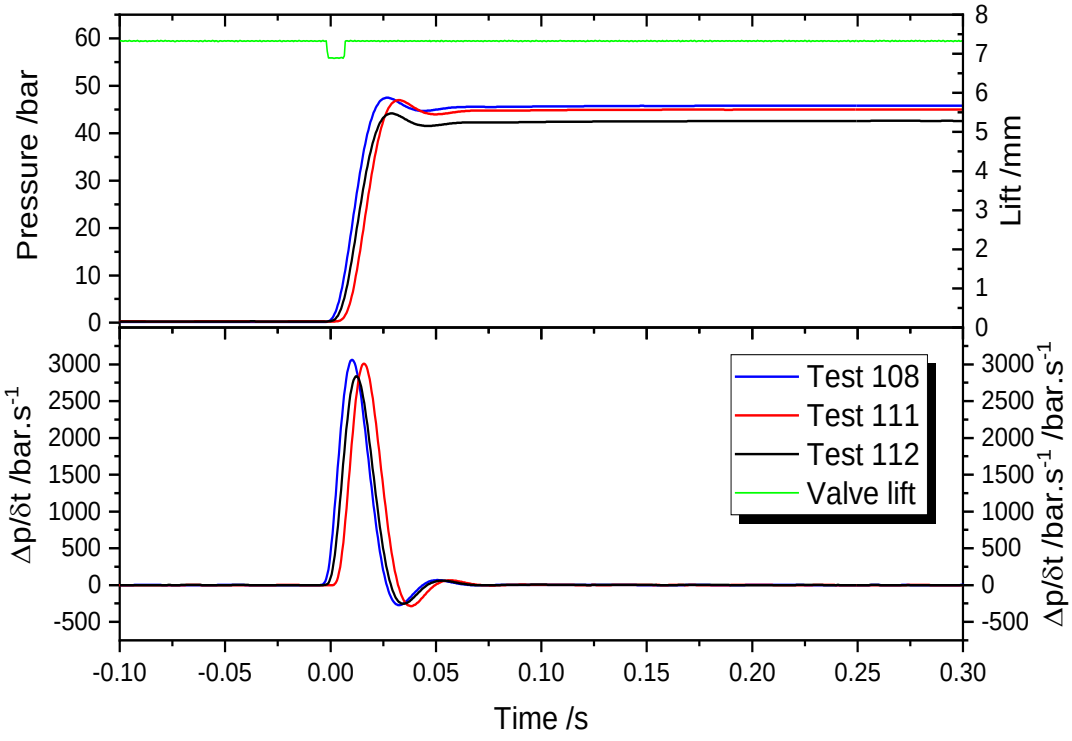

Figure 3.18: Vessel pressure and pressure time derivatives of repeat injections 108,111 and 112 conducted at 55 bar, 10 ms injection duration and sub-cooling ratio 0.78.

3.4.1 Injected mass

The mass of nitrogen injected into the cylinder is the most important aspect of the injection process. However, previous experimental work (21) had found it difficult to measure. Instead, the mass was calculated from the peak pressure assuming all the nitrogen had fully expanded.

The rig was modified (Figure 3.19) to allow for measurement of the nitrogen into the vessel for the duration of the injection. The piston was removed, and a length of pipe was used to connect the vessel to an off the shelf air heat exchanger. At this point, the nitrogen was fully gaseous and flow measurements were taken by the flow meter. A T-type thermocouple and another transducer were used to monitor and record the pressure and temperature of the nitrogen at the stage to verify its thermodynamic state. Any liquid through the flow meter would not only damage the flow meter but give false readings as well.

The volumetric flow rate was measured by the flow meter and the mass of nitrogen injected during this period was calculated from the ideal gas law using the temperatures and pressure readings. This was then converted to the mass of liquid nitrogen using the pressure and temperature readings at the inlet. Although this introduced a lag in the flow measurements (Figure 3.20), it was not an issue for steady-state operation and avoided the complexities associated with two-phase flow measurement(1). The flow was observed to increase 0.4 s after the valve is opened due to the time it takes to reach the flow meter as shown in Figure 3.20.

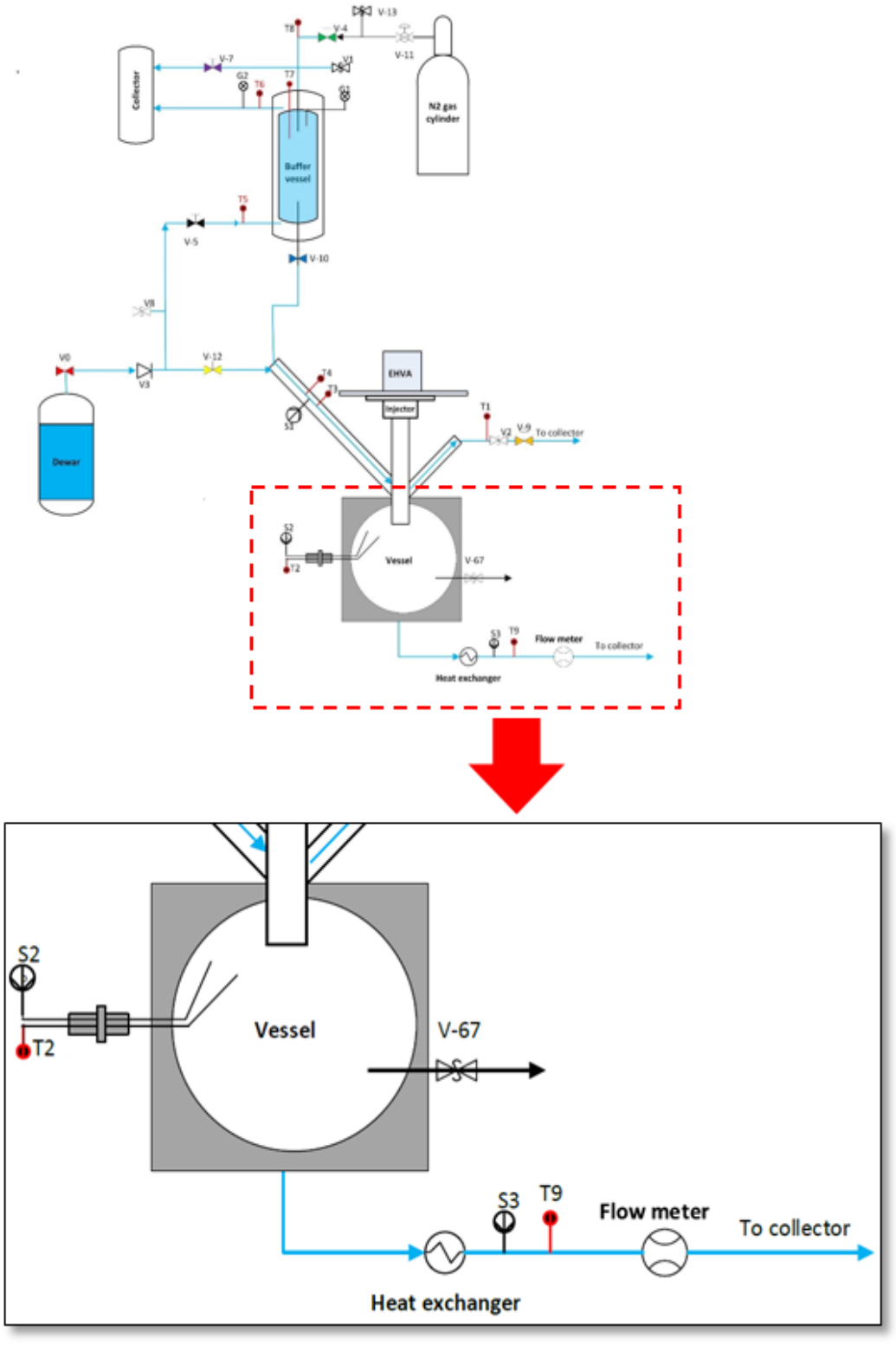

Figure 3.19: Schematic of modified rig to measure injected mass

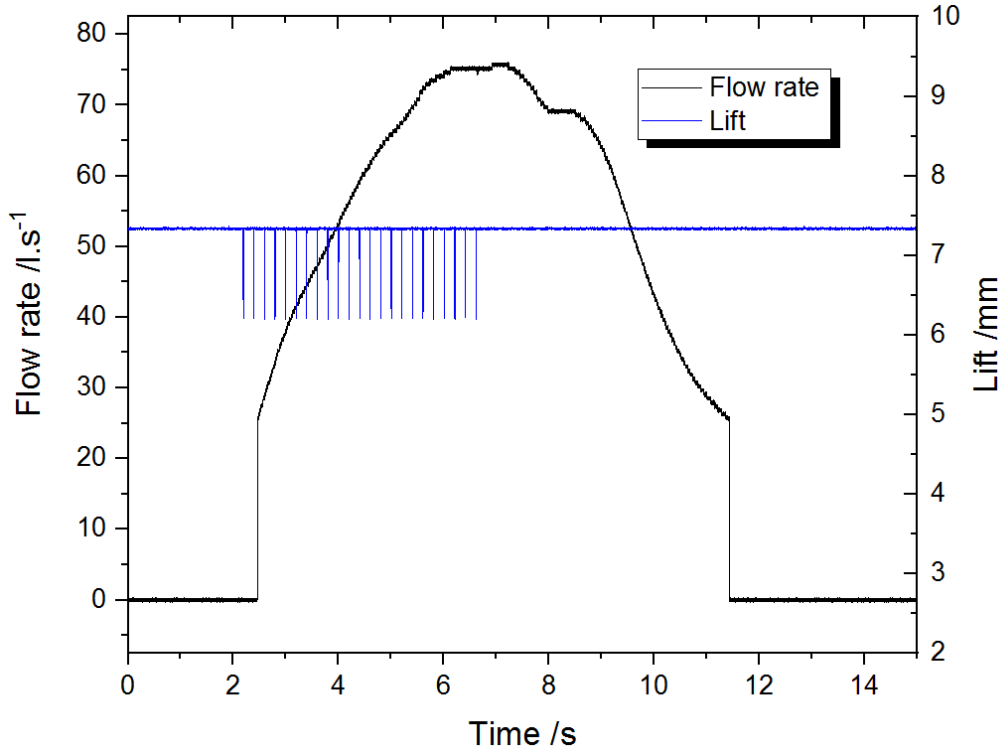

Figure 3.20: Measured flow rate of the expanded nitrogen at the flow meter at P_{inj} = 44 bar at 5 Hz for a duration of 5 s.

The flow is observed to increase immediately to 25 l/s because this was a minimum operating range of the flow meter. The flow rises steadily and reaches a maximum flow rate (76 l/s) when the valve is closed, where it decreases and reaches zero.

A high frequency was necessary so that the flow was high enough to be detected by the flow meter and maximum flow rates of up to 751 l/s were recorded. Over 200 injections were conducted and some of the data is presented in Table 3.3 to demonstrate the range of control parameters provided by the rig. A higher degree of sub-cooling and injection pressure increased the flow density through the valve resulting in a greater mass transfer as shown in Figure 3.21.

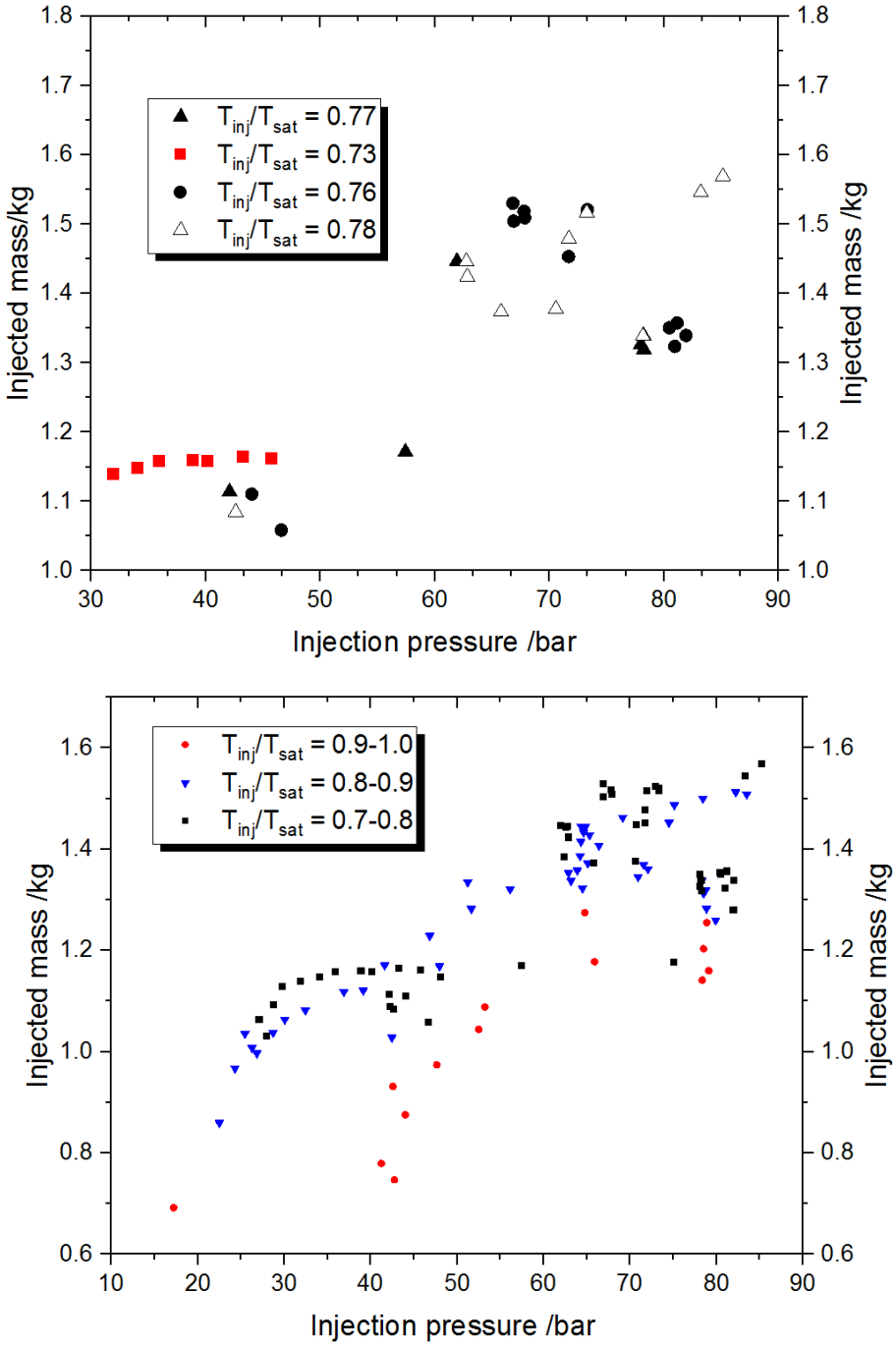

Figure 3.21: Injected mass with increasing pressure and sub-cooling ratio

On the other hand, the inherently high injection velocity would introduce more turbulence and instability across the valve opening. It is important to note that these results will be lower due to the effects of back pressure in the cylinder as well as the onset of turbulence at the valve.

The injected mass was used to estimate the average mass flow rate across the valve for the 10 ms the valve is opened and closed. Results showed values ranging from 0.11- 0.25 kg/s for an injection period at the maximum valve lift, which would indicate a 22- 50 kW output assuming the engine operates at 100% efficiency.

Table 3.3: Injection run parameters to measure the injected mass

Test	P_{inj} (bar)	T_{inj}/T_{sat}	Valve speed (Hz)	Lift (mm)	$\dot{Q}_g$ (l/s)	Time valve is actually open (s)	Injected mass (kg)	$\dot{m}_l$ (kg/s)
54	51.2	0.79	2	1.199	49.9	0.10	0.40	0.40
80	91.7	0.84	2	1.200	54.4	0.10	0.49	0.49
91	51.2	0.82	5	1.200	83.3	0.25	1.33	0.21
96	61.9	0.77	5	1.218	90.0	0.25	1.45	0.17
132	51.7	0.84	5	1.208	85.7	0.25	1.28	0.22
138	30.1	0.85	5	1.216	70.8	0.25	1.06	0.17
142	70.6	0.78	5	1.208	92.8	0.25	1.38	0.22
162	40.1	0.72	5	1.206	70.2	0.25	1.16	0.19
170	25.5	0.80	5	1.212	65.3	0.25	1.04	0.17
193	80.4	0.74	5	1.212	74.0	0.25	1.35	0.22

The total injected mass was observed to increase with valve speed as expected, contrary to previous experiments(1) as shown in Test 54 and 91 in Table 3.3. This was because the valve lift was set to a constant value and does not vary with frequency, which was an advantage of the EHVA system used in this work. Evidence of the effect on the injection period and therefore valve lift is shown in Figure 3.22. A 0.2 mm difference in the lift resulted in a ~10 kg/s decrease in the mass flow rate across the valve. Results showed a linear increase in the injected mass with the increased valve

lift, due to the increased flow area. This correlation can be used to determine the injected mass for a specified lift under these injection parameters, for this valve geometry.

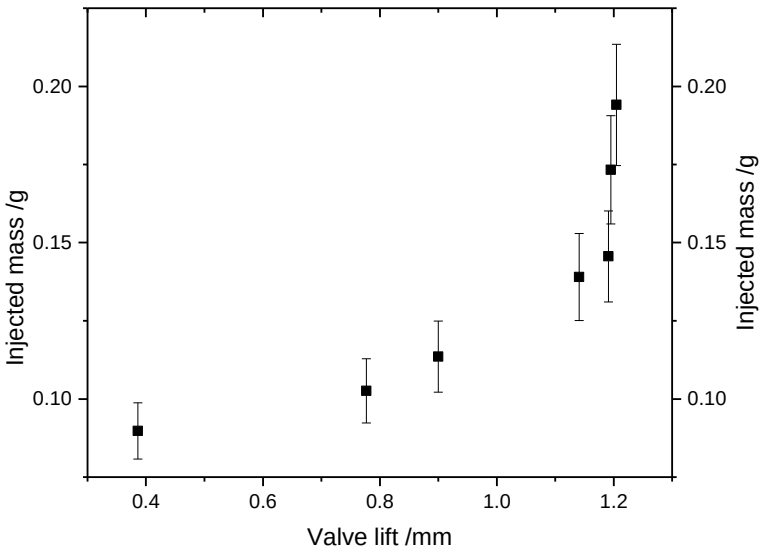

Figure 3.22: Injected mass with increasing valve lift at 68 bar

3.5 Chapter summary

The novelties of this study are shown in the design and modifications of the system that addresses the challenges that have limited the experimental work in the past. The operation of the sub-cooling, pressurisation and EHVA systems were stable. The design allows for effective control on the injection pressure, temperature and valve timing.

Nitrogen is injected at different thermodynamic states at pressures of up to 96 bar, which was 7 times higher than that of previous work (21, 22). This is credited to the simultaneous sub-cooling of the nitrogen as it was pressurised prior to injection, hence increasing fluid density and inherently the mass flow rate through the valve.

The opening and closing of the valve are controlled by the EHVA system using a simulated input signal, which allowed for the variation in the valve lift and injection duration.

CHAPTER 4

4 Injection of liquid nitrogen into water

The pressure rise from which the expansion occurs is a critical process in the engine operation. The pressurisation and expansion of the injected nitrogen determine the performance and efficiencies of the engine. The maximum pressure and rate of pressurisation is controlled and determined by several injection parameters. Previously, the possibility of a liquid nitrogen injection seemed to be extremely inefficient. This was partly due to an inefficacious delivery system causing large heat again prior to the injection into the engine cylinder and the lack of a well-engineered valve system to control the injection(21).

A series of off-engine liquid nitrogen injections were performed in this work using the test rig described in Chapter 3 to provide a greater understanding of the effects of injection parameters on the direct contact heat transfer, measured by the pressurisation that occurs in the cryogenic engine. The insight into this process will aid in the development and advancement of the design and operation of the engine.

4.1 Experimental conditions and procedure

The injections were conducted without the movement of the piston to demonstrate the pressurisation that occurs during the few seconds where the piston is held at TDC. The static nature of the injections allowed for the careful analysis of each individual injection, before factoring engine speed and the movement of other dynamic components, which were also bound to have an influence on the overall engine performance. It also facilitated the measurement and observation of the

continuously varying pressure and temperature in the cylinder. A larger vessel volume, fixed at 400 ml, was used to provide more flexibility in the experiments but specially to cater for a larger volume of HEF inside the vessel. Therefore, the results allowed for a better representation of the volumetric ratios in the real engine compared to previous work(21).

This study conducted over 400 single shot and pulsed injections which are fifty times that presented in the most recent experimental work similar to this. A larger number of injections confirms the repeatability and therefore reliability of the gathered data, allowing for the development of more accurate performance curves of the engine's performance. These can be found in Table 1 and 2 in the Appendix with a few shown in Table 4. The larger data set allows for a better comparison, more confidence in the operation of the test rig to produce reliable and repeatable results. This ultimately is better grounds to further the development of the engine and establish performance correlations.

Nitrogen was injected in three thermodynamic phases; liquid, gas and above its critical point at various injection pressures. Pressure and temperatures readings at the injector inlet were used to monitor the condition of the nitrogen prior to injection. At the desired pressure and temperature, the valve was triggered. As discussed in section 3.3.1, the nitrogen is simultaneously sub-cooled and pressurised in the buffer prior to injection to ensure an all-liquid condition.

Table 4.1. Injection test parameters

Test	P_{inj} (bar)	T_{inj} (K)	ρ_{inj} kg/m^3	Void (ml)	Phase	Injection period (s)	Mass (g)	P_{eak} (bar)	dp/dt (bar/s)
6	30	103.6	685	200	Liquid	2.5	1.617	7.0	349
11	30	87.1	770	2	Liquid	0.01	0.210	90.3	2882
67	10	98.8	627	5	Liquid	0.01	0.104	17.9	627
74	10	107.9	38	5	Gas	0.01	0.037	6.4	314
173	55	193.0	110	2	Supercritical	0.01	0.050	21.7	1419
183	25	99.7	701	2	Liquid	0.01	0.072	30.8	1926

4.2 Results

4.2.1 Effect of injection thermodynamic status

4.2.1.1 Liquid nitrogen injections

An example pressure curve upon the injection of liquid nitrogen is shown in Figure 4.1 over a period of 0.35 s (i.e. Injection 183 at a feed pressure of 25 bar and at 21 K below saturation temperature). The initial pressurisation was very rapid at 1927 bar/s up to 30 bar, at which point the pressure decreased slightly and then plateaus off at 31 bar, some 0.2 s after the valve is triggered.

The very high initial pressurisation rate was a result of both mass transfer of nitrogen into the free volume and heat transfer to the injected liquid. Majority of the heat transfer was from the water due to the increased albeit irregular and intermittent contact area. A smaller percentage of the heat will be from any contact with the walls of the vessel.

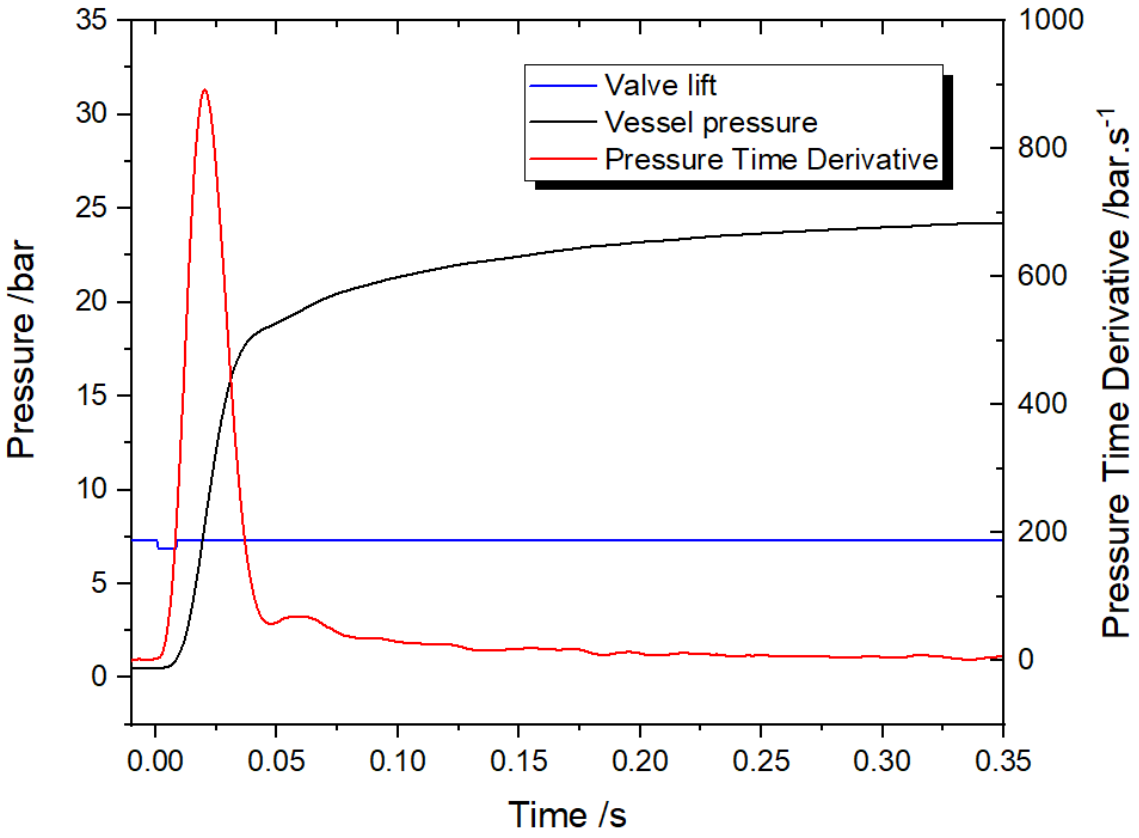

Figure 4.1: Pressure rise for injection 183 at P_{inj} = 25 bar

Any further pressurisation was solely based on the heat transfer over a longer period of time, which was the transfer of sensible heat to the newly expanded cold nitrogen gas. At this point, when dp/dt = 0, it was assumed that the injected nitrogen was completely vaporised, and the gas was at ambient temperature, where there was no further transfer of heat.

Figure 4.2 of the pressure curve on a 10 ms scale indicated three distinctive stages of the pressurisation; the initial stage (1) with a rapid increase in the pressure gradient, a second stage (2) with the decrease in pressure gradient that goes to zero and the final stage (3) with smaller peak.

The slight increase in pressure at stage 3 was due to the further pressurisation of the vessel as a result of heat transfer to the vaporised nitrogen as it reaches ambient temperature. However, this could also be due to further boiling of any remaining liquid that comes into contact with the water as a result of turbulence mixing in the vessel.

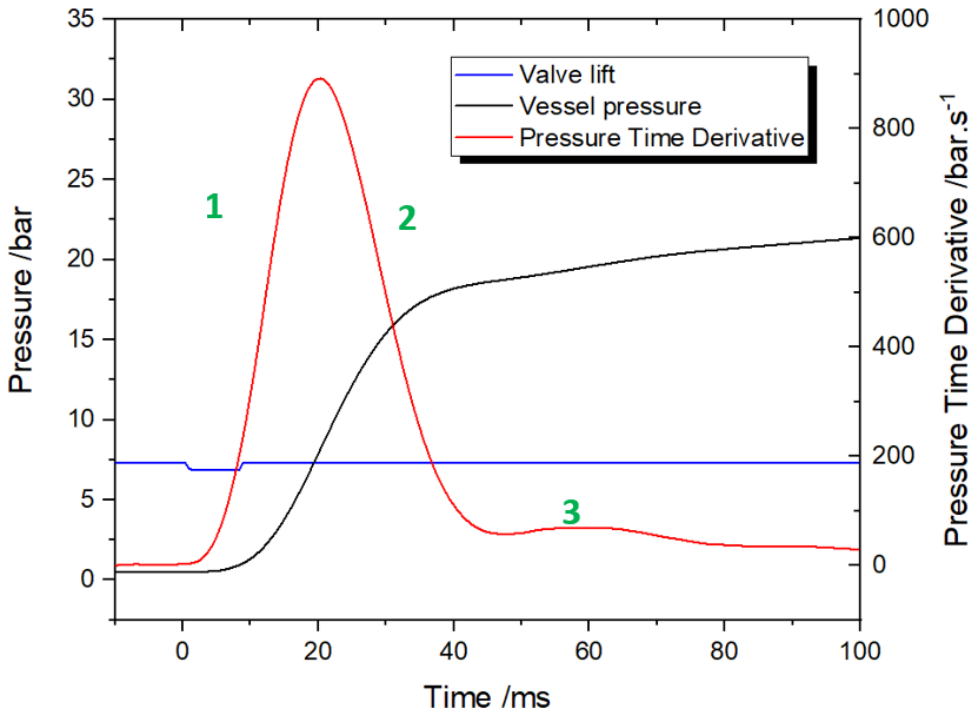

Figure 4.2: Vessel pressure, valve lift and pressure time derivative for injection 183 shown over a 10ms scale.

4.2.1.2 Gas injections into water

Gas and liquid injections of nitrogen at 15 bar were conducted to allow for the comparison of pressurisation rates. Subcooled liquid nitrogen, below saturation temperature, and cold gas injections were compared at 96 K and 112 K respectively (Figure 4.3).

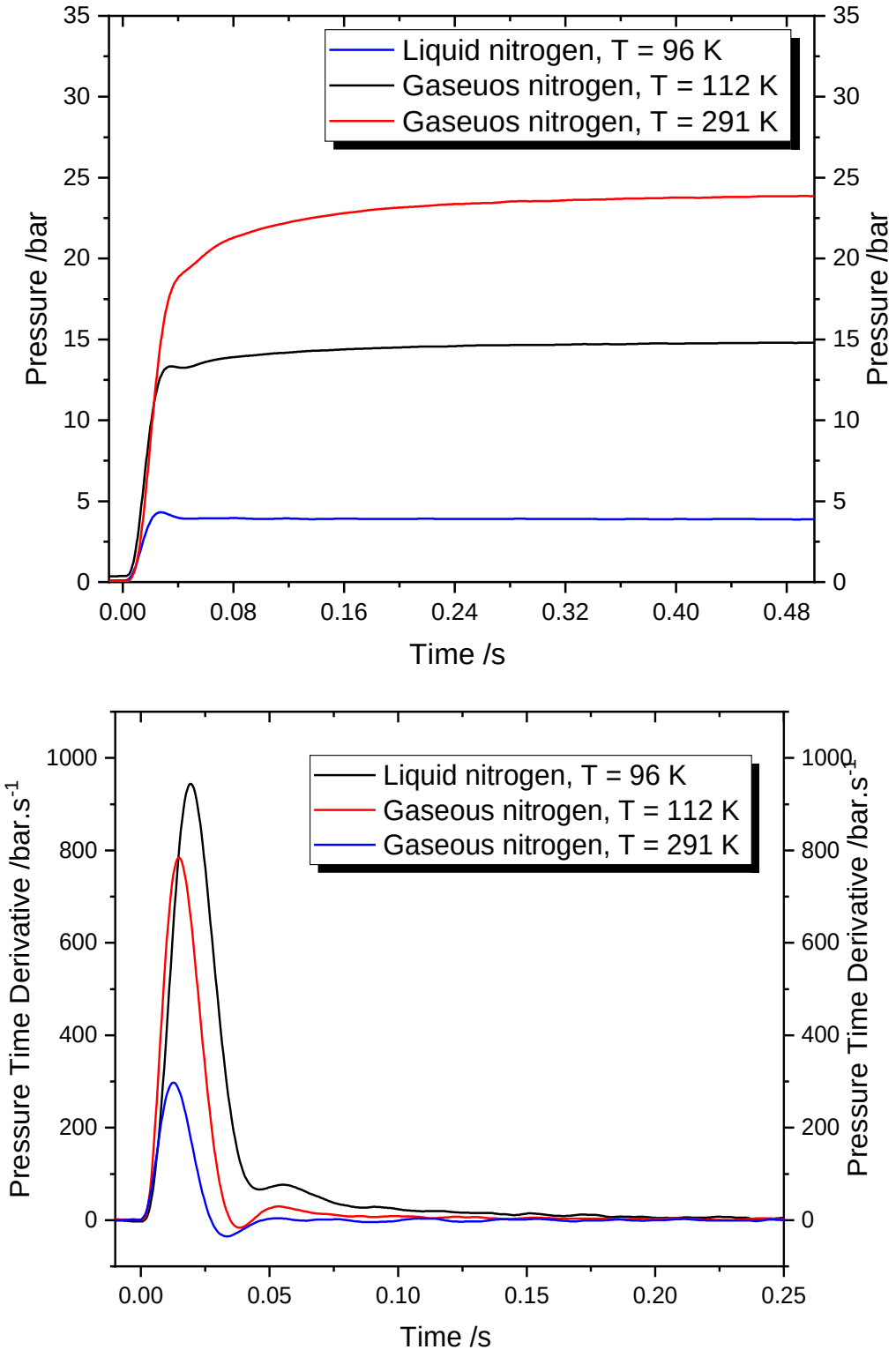

Figure 4.3: Vessel pressure profiles and pressure time derivatives for liquid, cold gas and warm gas nitrogen injections into water at P_{inj} = 15 bar.

The pressure profiles show that the gas injection demonstrates different behaviour

from that of the liquid. Initially, the vessel pressure rises very quickly because the gaseous jet propagates through the water a lot quicker than the liquid, due to higher flow velocity given its reduced density and compressibility. The pressure profile flattens suddenly and remains constant at 15 bar.

The peak pressures of the gas injections were a lot lower than that of the liquid because of the reduced mass flow rate through the valve, as a result of the reduced flow density for the given injection pressure. The mass injected in the liquid phase was $\sim$ 1.7 times of that injected for the gaseous phase, at 0.058 g and 0.035 g respectively. At an injection duration of 10 ms, the gaseous cases showed the lack of further pressurisation after the valve was closed. This indicates that much of the heat transfer is completed during the injection stage.

Liquid and gas injections displayed this variation because the gas fills the void quickly, whilst the liquid fills and expands in the void a lot slower. This is also due to the reduced temperature difference and consequently reduced heat flux in the vessel. In this case, the pressurisation is highly dependent on the sensible heat transfer from the HEF. The pressurisation rates for the injection of nitrogen in its liquid state shows the benefits of the latent heat.

Both warm ($T_{inj} = 291\ K$) and cold injections of gaseous nitrogen are compared. The pressurisation rates showed a significant difference in the peak pressure and maximum pressure time derivative. The maximum dp/dt of the cold gas was 3 times that of the warm gas, solely due to the difference in injection density ($\sim$ 44 kg/m^3), which as discussed before affects the mass flow rate across the valve. Assuming no

heat transfer, the pressurisation from the warm gas was solely as a result of the mass transfer, which accounts for approximately 30 % of the overall pressure rise in the vessel.

For a pressurisation rate of 784 bar/s in the case of cold gas injection, based on *Equation 4.1*, the addition of latent heat resulted in ~ 20 % increase in the pressurisation in the vessel.

$$\frac{dp}{dt} \propto \frac{dQ}{dt} = hA\Delta T \qquad 4.1$$

This was still quite low considering 200 kJ of heat energy is converted to pressurise the vessel. This was due to the boiling of the liquid nitrogen within its own vapour blanket, thereby restricting any direct contact with the HEF inside the vessel. On the other hand, this is a percentage could be increased with the optimisation of injection parameters. Hence the use of injection parameters to increase mass transfer and facilitate the jet breakup of the liquid nitrogen as it penetrates and propagates through the water.

4.2.1.3 Supercritical injections

With the increase in injection pressure, subcooled liquid injections were also compared with supercritical injections, that is injections where P_{inj} >33.4 bar andT_{inj} > 126.2 K. The pressure profiles were found to be identical to that of gaseous injections, albeit with much higher peak pressure. This was because of the increased mass flow rate through the valve as a result of the increased injection pressure. In the same way, these rates of pressurisation were solely a result of the mass transfer and transfer of sensible heat to the cold nitrogen. The peak pressure

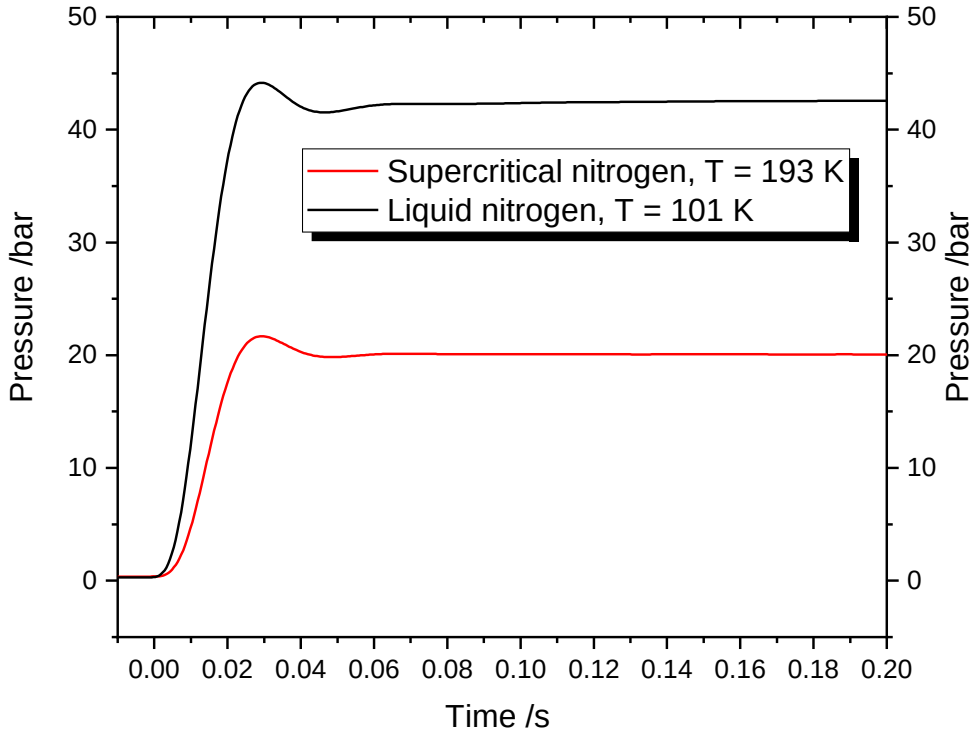

Figure 4.4: Pressure profile liquid and supercritical injections of nitrogen at 55 bar

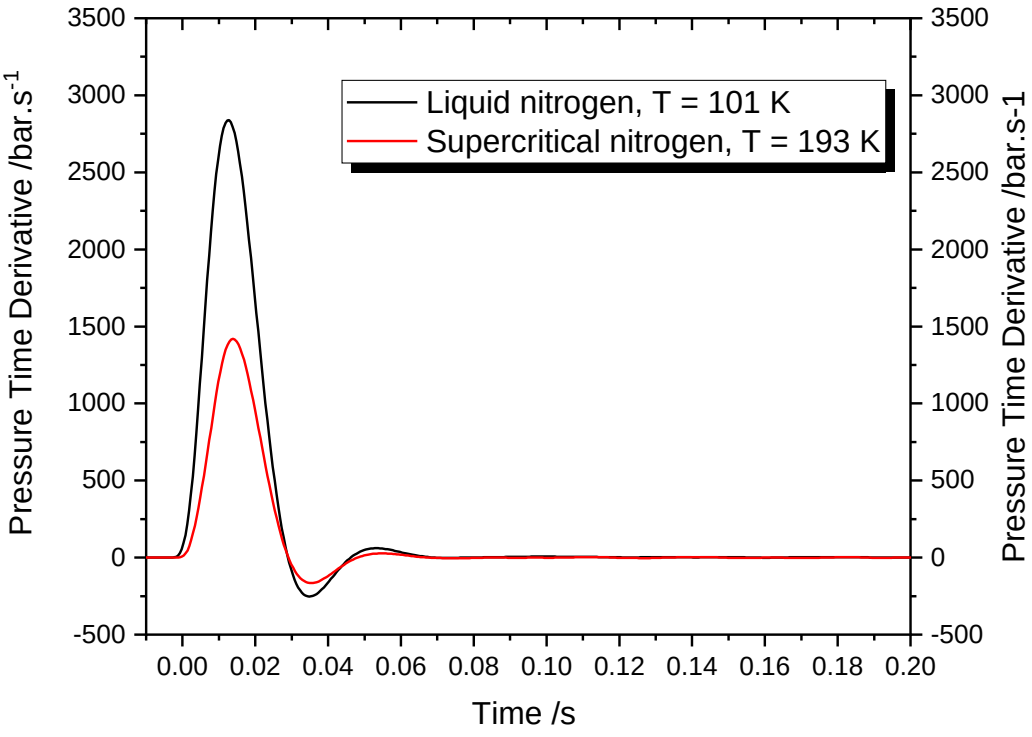

Figure 4.5: Pressure time derivative for liquid and supercritical nitrogen injections at 55 bar

and pressure time derivative of liquid injections were found to be twice that of nitrogen injected in a supercritical state (Figure 4.4 and Figure 4.5). A comparison of

the peak pressure and the maximum pressure time derivative for all three thermodynamic states with increasing pressure is shown in Figure 4.6. This once again reinforced the influence of increased flow density through the valve and benefits of latent heat from the liquid injections regardless of the injection pressure.

4.2.2 Effect of clearance volume

The clearance volume was the fixed volume of air above the piston in which the nitrogen expands. The clearance volume was an important factor in the engine performance as it determined the level of pressurisation attainable in the cylinder. It was determined and varied by the volume of water added to the vessel.

The water to air volumetric ratio was increased for the augmentation of the final pressure and the rate of pressurisation for a given rate of heat transfer per unit mass. Secondly, a larger volume of water was used to avoid the formation of ice debris, which was observed in fuel coolant interaction experiments(44) when water was injected into a pool of liquid nitrogen. Due to the drastic temperature drop, the subsequently formed ice would limit the movement of the piston and other moving components of the engine.

These results are demonstrated in Figure 4.7 with a comparison of liquid nitrogen injections 6 and 11 conducted at 30 bar and an injection temperature of 104 and 87 K respectively. With a larger volume to fill, the peak dp/dt in a 200 ml void was reduced by a factor of 8, in comparison to that with a 5 ml free volume. The peak pressure should be at least 40 times larger but is only 13 times greater because the valve was opened for only 1/250 of the time. It was necessary to increase in the

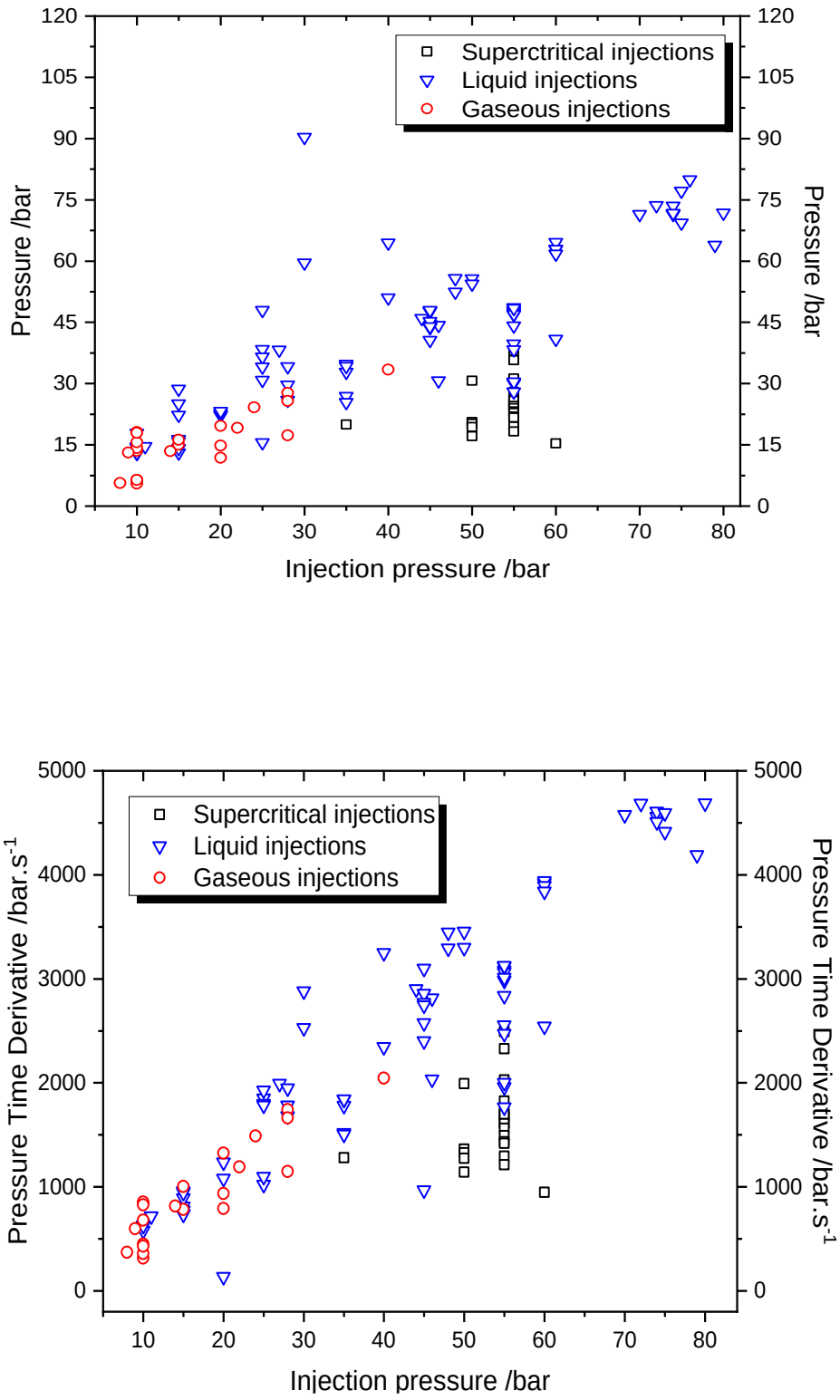

Figure 4.6: Peak pressure and maximum pressure time derivative for liquid, gas and supercritical injections at various injection pressures.

injection duration so as to get a pressure rise in the larger volume.

In similar liquid injections(22) conducted with a larger volume (90 ml) and at the injection pressure of 14 bar, a pressurisation rate of only 400 bar/s was recorded; half of what was recorded in these injections.

A larger free volume allowed for more heat transfer with the warm gas, before making contact with the water. By moving the water surface further from the valve

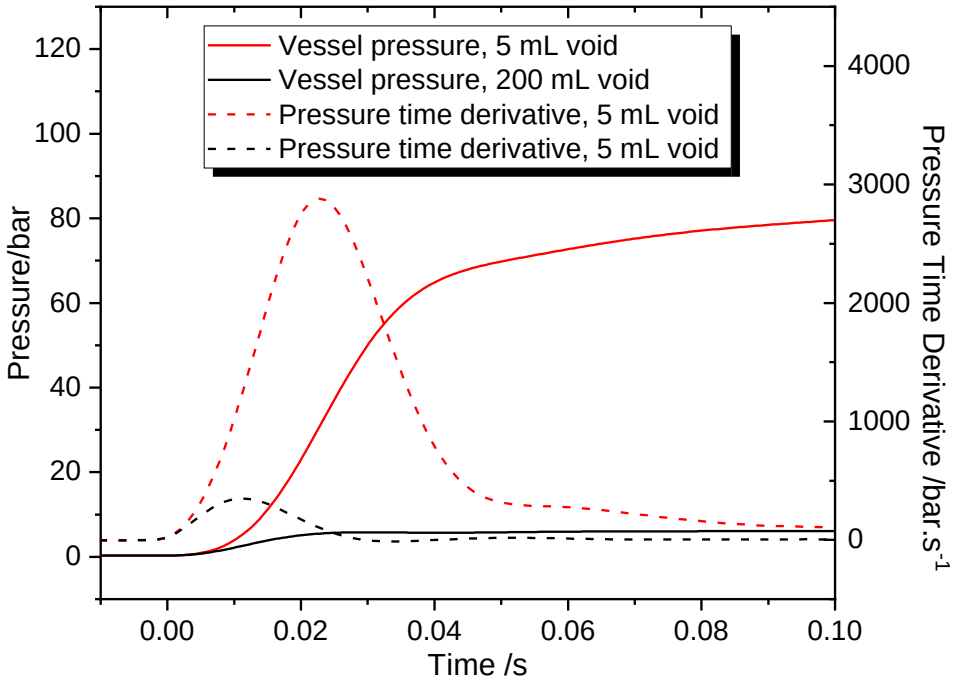

Figure 4.7: Pressure and pressure time derivative profiles for liquid nitrogen injections 6 and 11 at 5 and 200 ml free volume inside the vessel.

exit, higher flow velocities are required to have the same impact and propagation through the water. High impact with the water surface drives further turbulence with the volume of water which resulted in the breakdown of the formed vapour cloud layer and allowed for the rest of the trapped liquid to access heat from the water.

There was also the fact that the water had a greater mass and specific heat capacity in comparison. Therefore, the dispersion of energy is greatly controlled by the initial

contact and interaction which could result in a vapour explosion as they begin to mix(43). Furthermore, less water in the vessel reduced the amount of heat available to expand the injected nitrogen. Assuming the nitrogen gas behaves like an ideal gas, when divided by volume Equation 2.10 becomes Equation 4.2.

$$\frac{dp}{dt} = \frac{dm}{dt}\frac{RT}{V} + \frac{dT}{dt}\frac{mR}{V} \qquad 4.2$$

This shows that the continued decrease of the free volume (V) increases the pressure time derivative infinitely. However, this would reduce injection duration as the pressure would rise too quickly, exceeding that in the injector.

4.2.3 Effect of liquid nitrogen injection pressure

The pressure profiles of liquid nitrogen injections of 28, 55, 60 and 74 bar were compared in Figure 4.8. Each pressure profile was averaged over three injections and was conducted at a valve lift of 1.2 mm and the valve remained open for 10 ms. The pressure profiles demonstrated a clear increase in the peak pressure and the maximum pressure time derivative with increasing injection pressure.

Figure 4.9 shows the pressure profiles as a ratio of the local pressure to the peak pressure to objectively compare the speed at which the peak pressure was achieved, for a range of injection pressures. Because it was established that the peak pressure was approximately proportional to the injected mass, this was fair comparison of the various injected masses at different pressures for a fixed injection duration and valve lift.

Higher injection pressures were bound to result in greater pressurisation rates due to the increased flow velocity. The results (Figure 4.9) also showed an enhanced heat

transfer post injection. Higher injection pressures show slower rates closer to the plateau, which implied that the equilibrium temperature was attained a lot faster.

This is also suggested in Figure 4.8, that showed no evidence of the third stage and that the majority of the energy transfer occurred at the beginning of the pressurisation due to the high heat transfer coefficient.

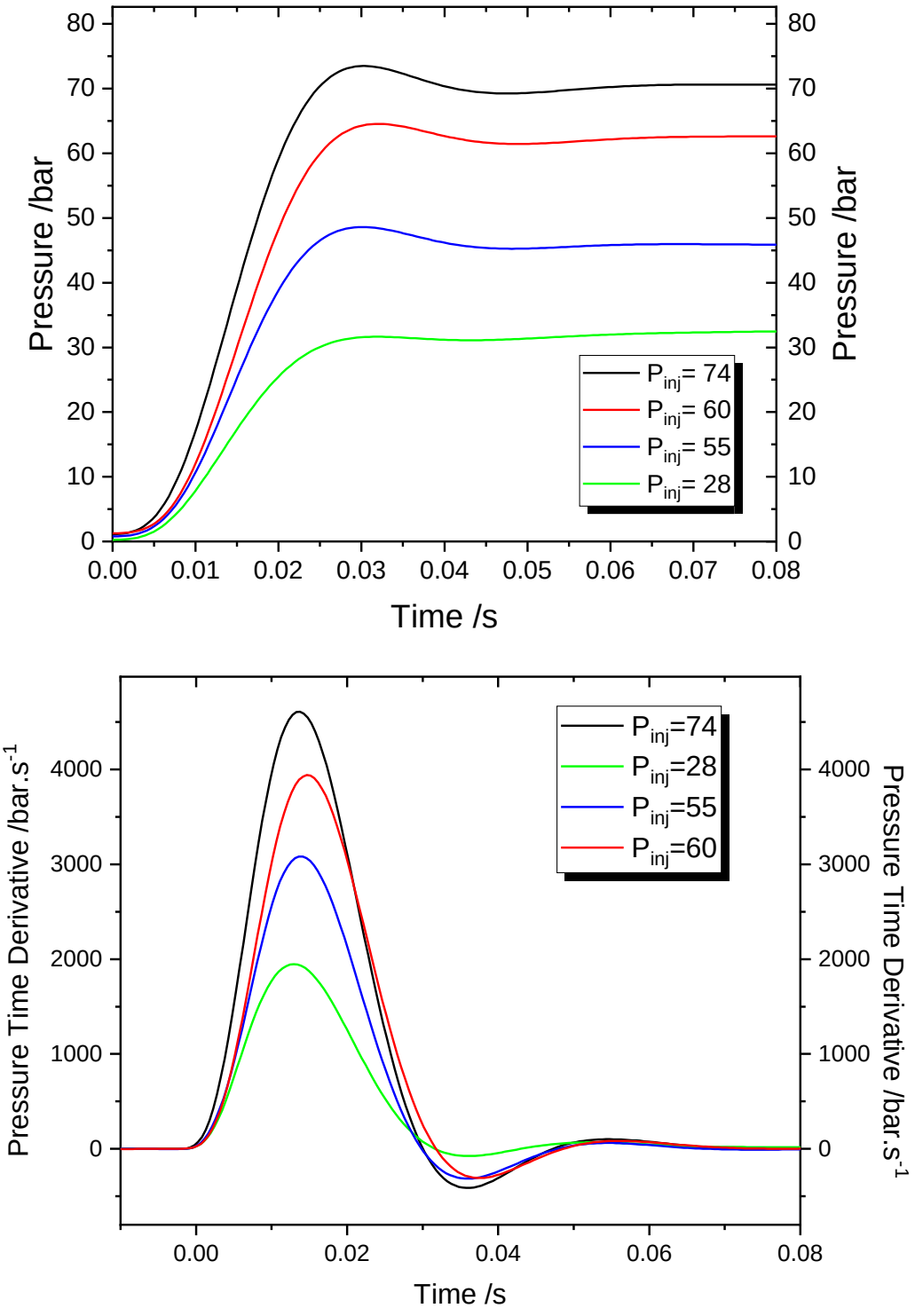

Figure 4.8: Vessel pressure and pressure time derivatives for liquid injections for various injection pressures at a sub-cooling of 0.83.

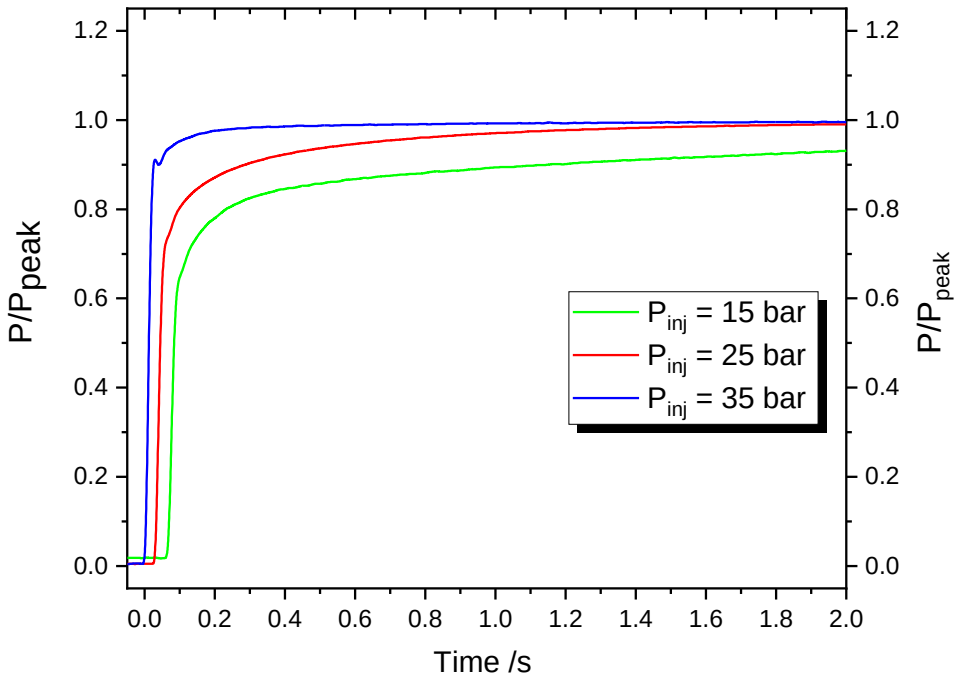

Figure 4.9: Profiles of pressure as a ratio of peak pressure displayed for liquid phase injections at for various injection pressure at the same sub-cooling ratio of 0.8.

There was an almost linear increase in both the maximum pressurisation rate and the vessel pressure with increasing injection pressure despite some outliers similar to the experiments conducted in previous work (21, 22).

For further comparison, the maximum pressure time derivative and vessel pressure were indexed to those of an injection at 10 bar. The data was indexed to that of Test 67 at an injection at 10 bar, which allowed the comparison of the peak pressure and dp/dt in relation to that obtained at 10 bar as shown in Figure 4.10.

There was a more prominent trend in the pressure time derivative that was still evident in a larger data set, even when other parameters such as temperature and injection duration are unchecked.

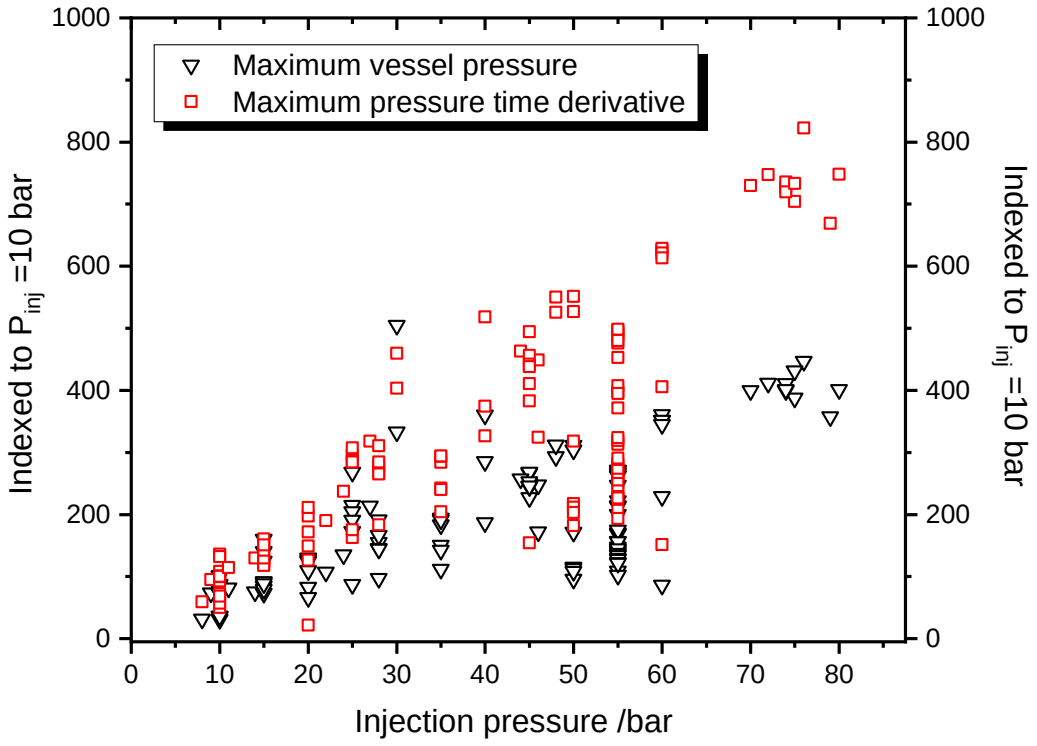

Figure 4.10: Indexed maximum pressure and pressure time derivative for liquid nitrogen injections at different injection pressures. Values at 10 bar injection = 18 bar and 627 bar/s respectively. 5

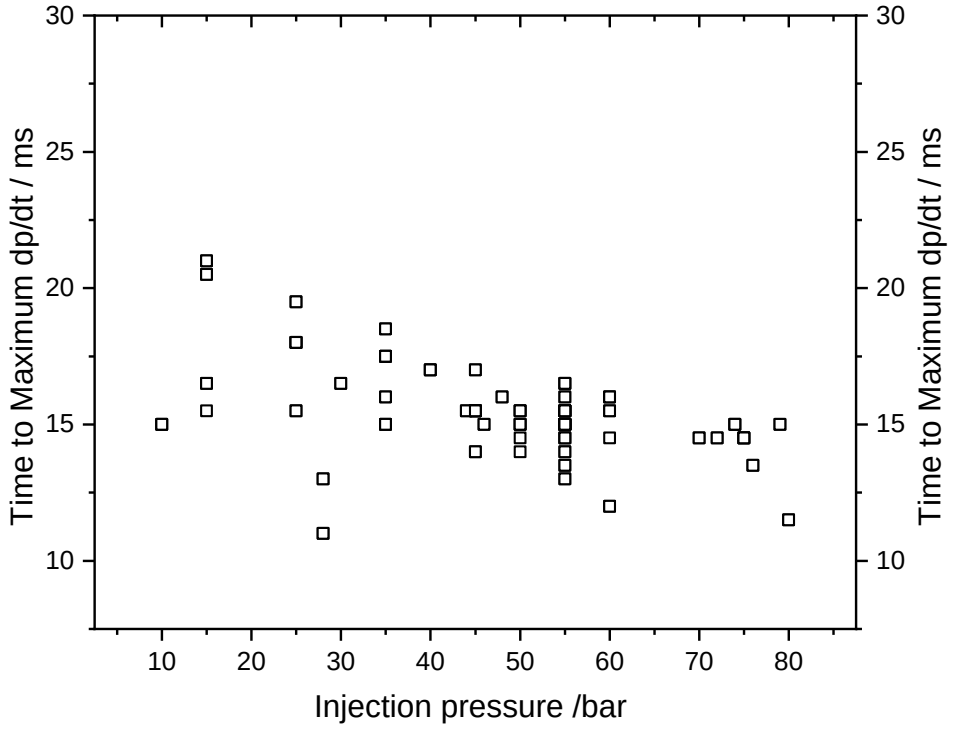

Figure 4.11: Time to maximum pressure time derivative with increasing injection pressure

4.2.4 Injection temperature

Liquid nitrogen was injected at different temperatures and the degree of sub-cooling was quantified by the subcooling ratio $\left({}^{T_{inj}}/_{T_{sat}}\right)$.The pressure profiles at different ratios are shown in Figure 4.12. The rate of pressurisation was greater for a lower ratio because of the high mass flow rate, as a result of the increased flow density through the valve. Subsequently, the speed of the pressurisation was reduced as the injection temperature approaches saturation. Closer to saturation temperature, the effect of flashing would be observed, which manifested in a slower rise in pressure as more of liquid emerges from the orifice.

Accordingly, there was a slight decrease in the maximum pressurisation as a result, albeit with a larger peak pressure attributed to the increased injected mass. This is evident in Figure 4.13, which shows the increase in the injected mass with density and pressure.

There was an insignificant difference in the pressurisation rate below a cooling ratio of 0.9. Therefore, while the rates at a lower temperature were bound to be higher, this implied that the larger proportion of the energy was a result of the phase change, and not the sensible heat transfer between injection and saturation temperatures and from saturation to ambient temperatures.

Figure 4.14 shows a stronger linear correlation between the peak pressure and the increasing injection pressure compared to that with the pressure gradient within the sub-cooling catergories.

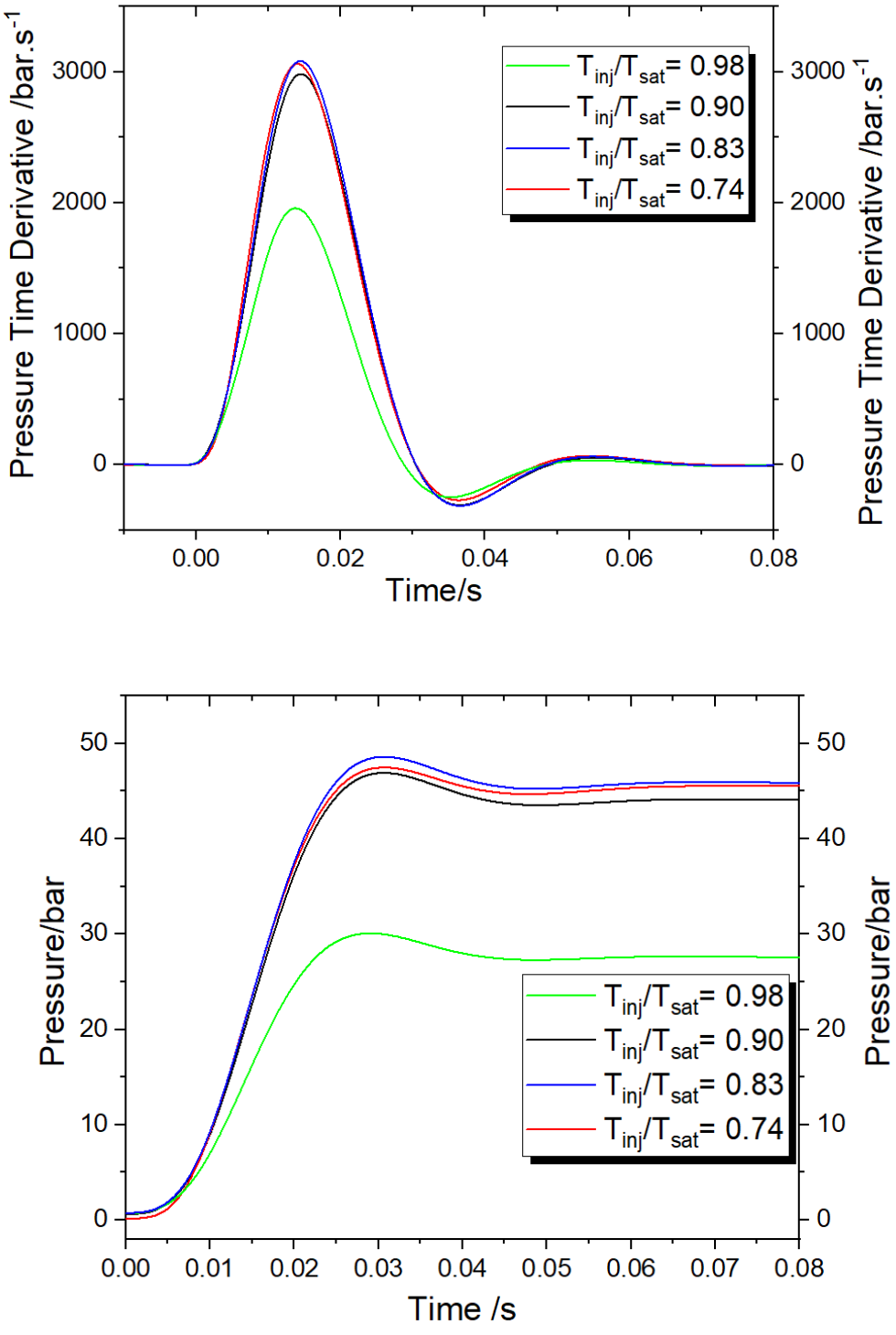

Figure 4.12: Vessel pressure and pressure time derivative profiles for liquid injections at different levels of sub-cooling but at a constant pressure $\left(P_{inj} = 55\ bar\right)$.

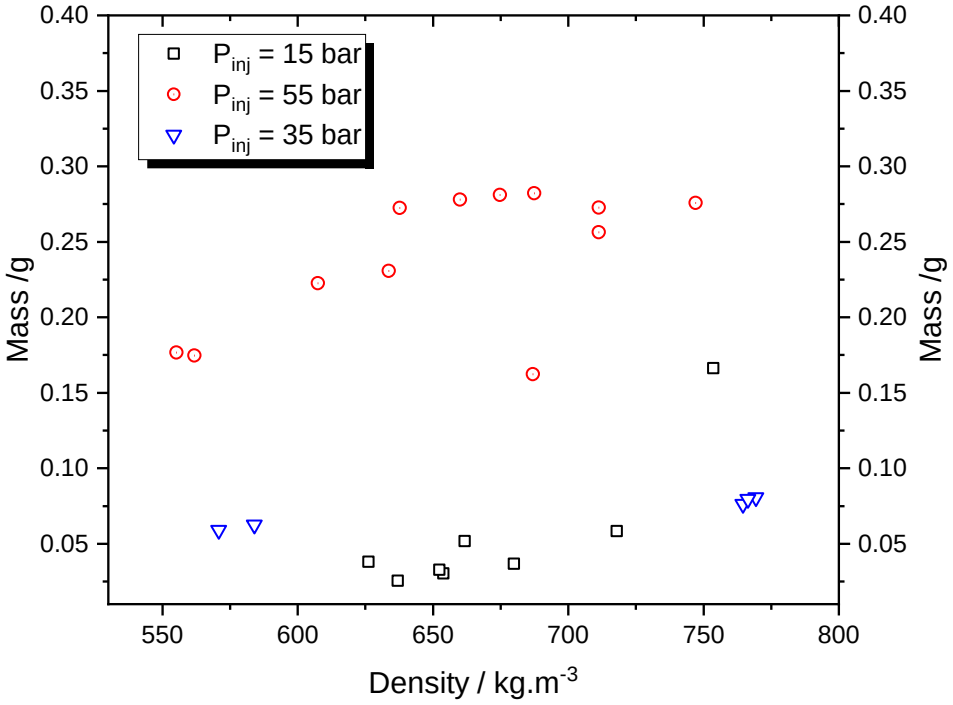

Figure 4.13: Injected mass with at different injection density.

This was because the temperature had a greater influence on the injected mass than the heat transfer process. Therefore, by focusing on just the temperature, Figure 4.15 shows a linear decrease of the maximum pressurisation for the controlled injections at 55 bar, but no clear correlation when all the data was compared. The constant pressure allows a comparison of the pressurisation of the different masses injected.

With increasing pressure, it became more difficult to achieve subcooled nitrogen below 100 K. On the other hand, with the large pressure drop incurred by the nitrogen upon the opening of the valve, would lead to the immediate onset of flashing. This could cause the majority of the liquid to evaporate, which would refute any subcooling that had been achieved prior to injection.

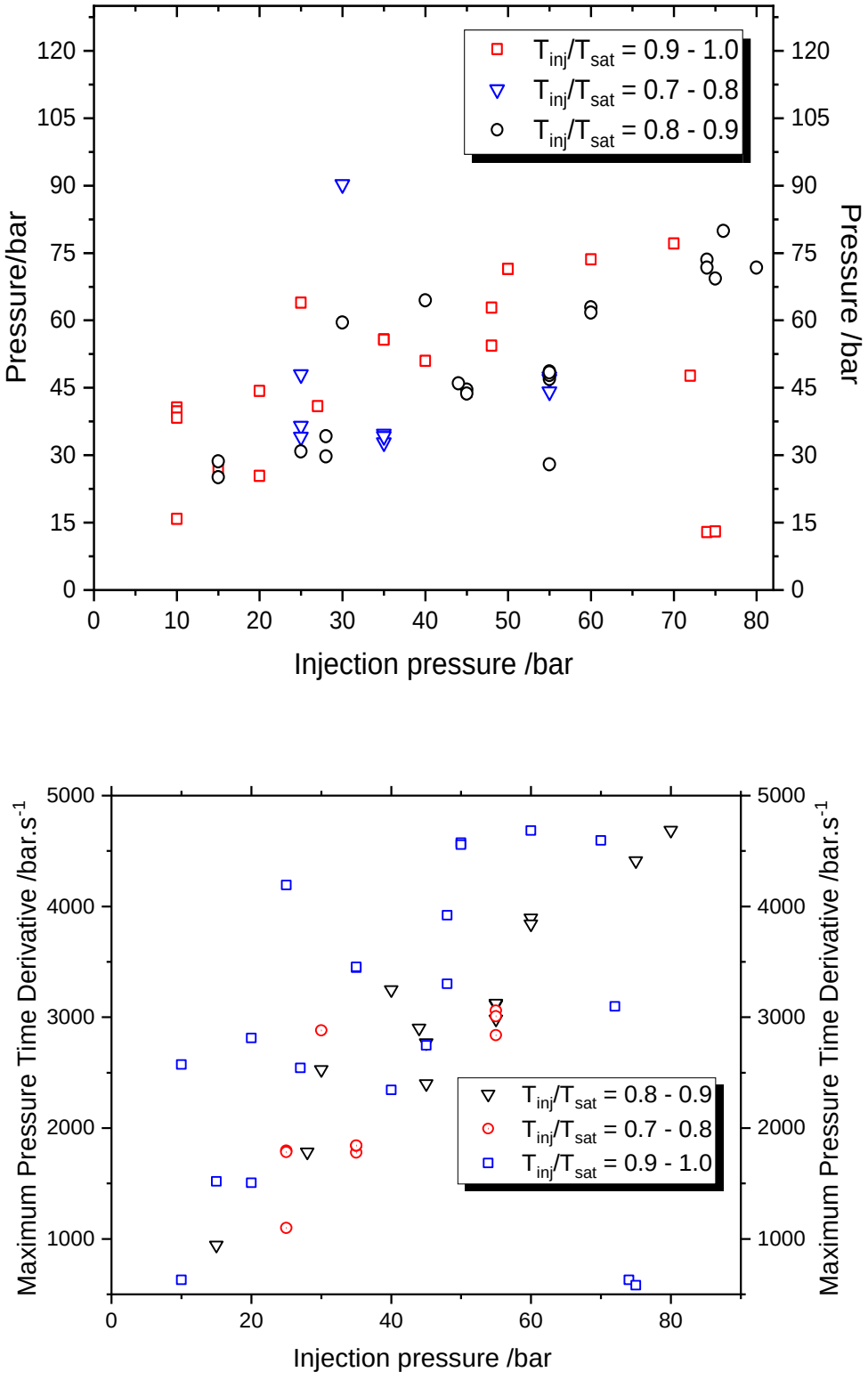

Figure 4.14: Peak pressure and pressure time derivative with increasing pressure and sub-cooling ratio

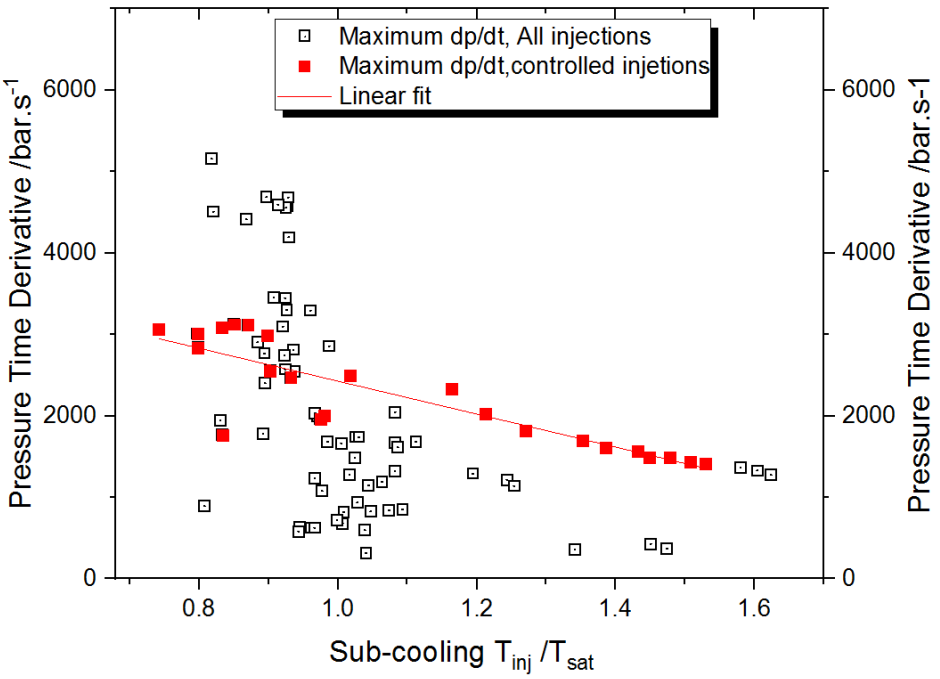

Figure 4.15: Indexed pressure rise and maximum pressure time derivative for increasing sub-cooling for 2 ml and 5 ml voids for supercritical injections at P_{inj} = 55 bar

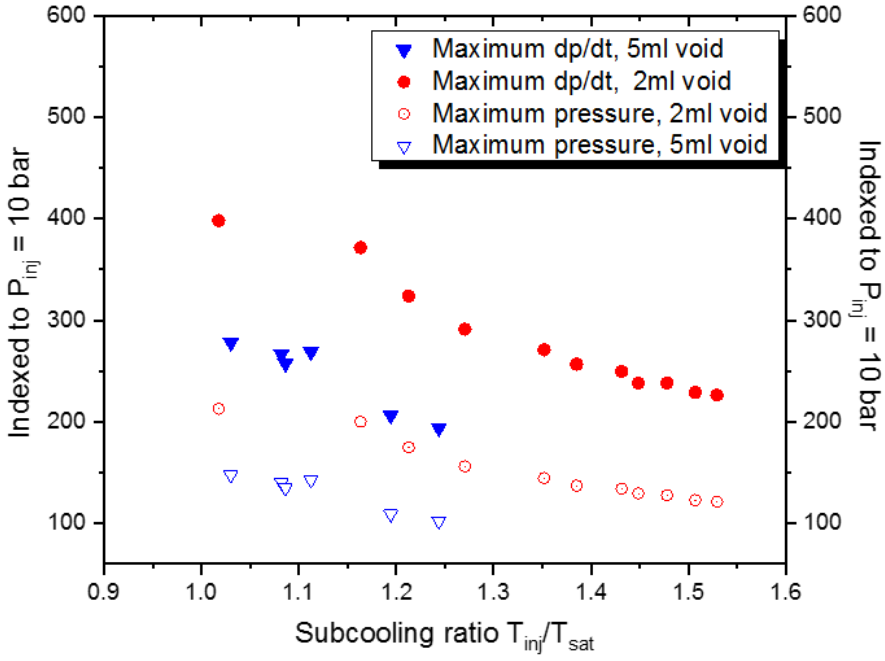

Figure 4.16: Maximum pressure time derivative with sub-cooling for uncontrolled and controlled injection at 55 bar. A linear fit is indicated for the controlled injections.

Evidence of this can also be seen in Figure 4.14, in which injections subcooled to a ratio between 0.8-0.9 produce a higher peak pressure and a maximum pressurisation, in comparison to that subcooled to a ratio less than 0.8. This pointed to ineffective sub-cooling. The results were also indexed to Test 67 shown in Table 4.1, which provided a better comparison of the increase in the maximum pressure time derivative and vessel pressure for nitrogen in its supercritical state at 55 bar (**Error! Reference source not found.**). There was an asymptotic decrease in both p arameters for a fixed free volume, once again confirming the proportion of energy converted from sensible heat transfer.

Liquid injections ($\frac{T_{inj}}{T_{sat}} < 1$) showed a considerable difference between the maximum pressurisation rate and the maximum pressure, which was due to the increased heat transfer rate provided by the deeper liquid jet propagation into the water and temperature difference between the water and nitrogen. On the other hand, this had no effect on the speed of the processes. That is, there was no significant variation of the time at which the maximum pressurisation occurred.

Figure 4.17 shows that, despite the increased mass flow during the injection, the injection pressure had a more prominent effect on the pressurisation, even when the sub-cooling ratio was relaxed. It was likely that the pressurisation would not increase infinitely with the increase in injection pressure. Past a certain point, the ratio of flow velocity to pressure would be taken over by the effects of cavitation and choking and the rate of mass transfer would be limited by fluid properties. However, even at these high pressures, this critical point was not attained here.

Therefore, based on the practicality of the injection process, the focus should be directed to the increase in the injection pressure for liquid injections, in order to improve the engine output and subsequently its efficiencies. The efficiency of this particular engine is perhaps more important because of the low energy density of nitrogen.

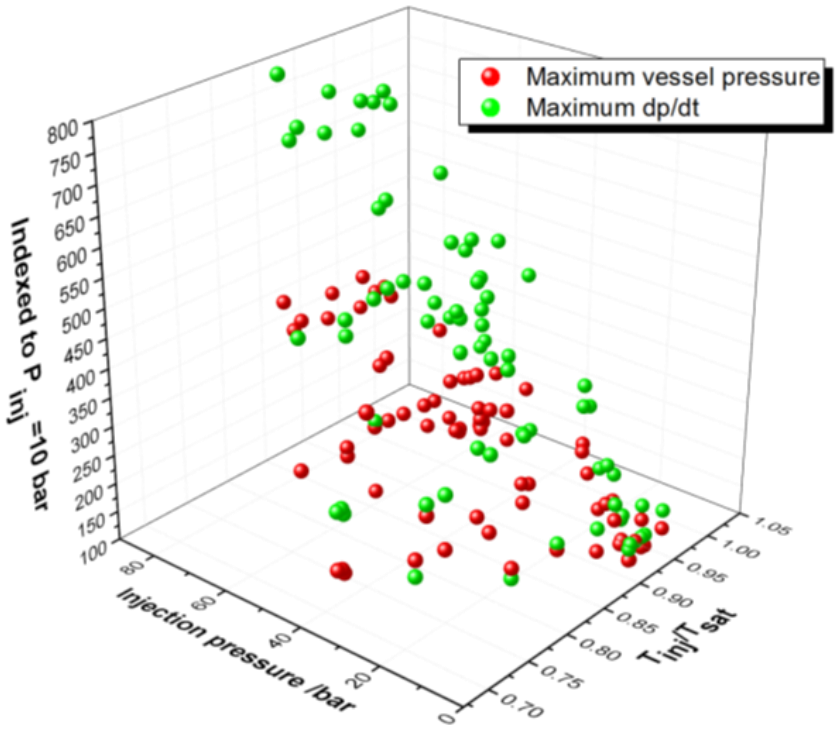

Figure 4.17: 3D plot showing a greater influence of the injection pressure on the increase in the pressure time derivative than the pressure rise in the vessel.

At a peak pressure of 90 bar, the maximum thermal specific work output of 0.58 MJ/kg, 161 Wh/kg at an injection pressure of 30 bar and a subcooing ratio of 0.705 was calculated. This represents a conversion of ~ 75 % of the available energy of nitrogen into useful work. However, this does not account for the energy consumed in injecting the sub-cooled liquid at such high pressure, as well as friction and pressure losses. The specific work of increases almost linearly before reaching an asymptotic maximum at the higher pressures as shown in Figure 4.18. This could be

attributed to the onset of two phase flow effects that are likely to reduce the mass flow across the valve.

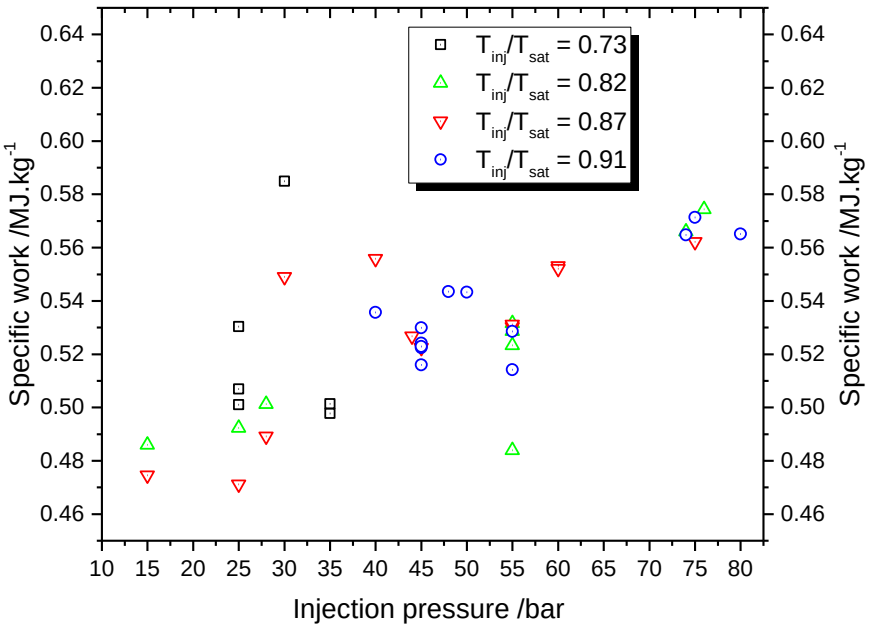

Figure 4.18: Specific work displayed as function of injection pressure for different sub-cooling

4.2.5 Effect of injection timing

The valve timing is a fundamental component of the injection process and consequently the engine performance and therefore vital to the work conducted here. It is considered necessary that the injection and boiling of the nitrogen occur with the piston still at TDC, so as to effectively utilise the minimum cylinder volume and achieve maximum pressurisation. Accordingly, this will influence the opening and closing of the valve to optimise the injected mass. Too long an injection and there was a risk of expelling none evaporated liquid nitrogen, while one that's too short would reduce the mass of nitrogen injected and the resulting peak pressure, thereby lowing the specific work output of the engine.

By controlling the period of the command signal, different valve profiles were established and were discussed in Section 3.1.7.1. A number of injections were conducted at different valve lifts and injection duration, but the pressure was kept constant at P_{inj} = 40 bar. The parameters of each test are shown in Table 4.2.

Table 4.2: Injection parameters for valve control investigations

Valve lift (mm)	Period (ms)	Cooling ratio	P_{peak} (bar)	Maximum dp/dt (bar/s)
0.386	4	0.84	5.3	1057.0
0.452	5	0.90	17.7	1218.3
0.602	6	0.92	19.6	1340.4
0.765	7	0.92	23.9	1619.4
1.023	8	0.93	25.1	1685.0
1.108	9	0.92	29.8	1935.4
1.221	10	0.93	30.7	1958.6
1.222	11	0.90	31.8	1979.0
1.222	12	0.90	32.2	1956.4

The injected mass was bound to increase with the injection duration and inherently the valve lift as shown in Section 3.4.1, because of the increased flow area. This is evident in Figure 4.19 whereby the generated peak pressure was reduced by a factor of 6 when the valve was triggered at the minimum valve lift of 0.386 mm. This value was found to a third of that of a gas injection at the same pressure but at the maximum lift. This was mainly because the short injection decreased the mass injected on account of the reduced flow area, which restricted the volume of nitrogen to be expanded. Effectively, this affected not only the peak pressure but the pressure gradient as well. It was assumed that the injected mass was in its liquid form

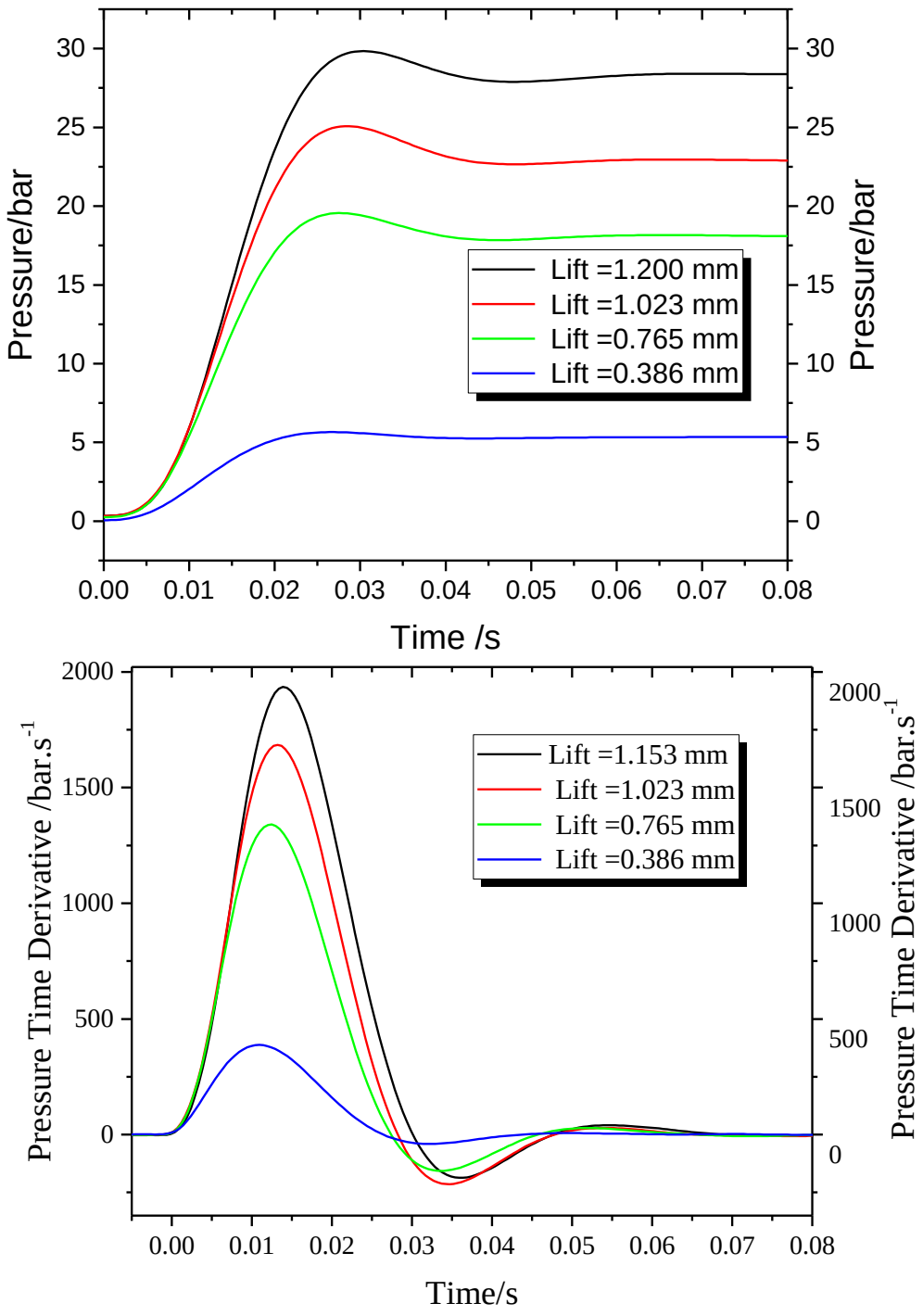

Figure 4.19: Time to maximum pressure time derivative with increasing valve lift for liquid injections at P_{inj} = 40 bar.

however, there was certainly some phase change during the injection by flashing of the liquid as pressure drops below the saturation pressure. In the initial stage of

injection visual experimental work(22) showed a gaseous jet preceding the liquid jet. Therefore, it was more likely that in this case the valve was only opened long enough to administer nitrogen gas, and without any velocity would not be able to propagate through the water. Examination of this set of injections demonstrated a compelling linear correlation between the increased injection period and the pressurisation parameters inside the vessel(Figure 4.20).

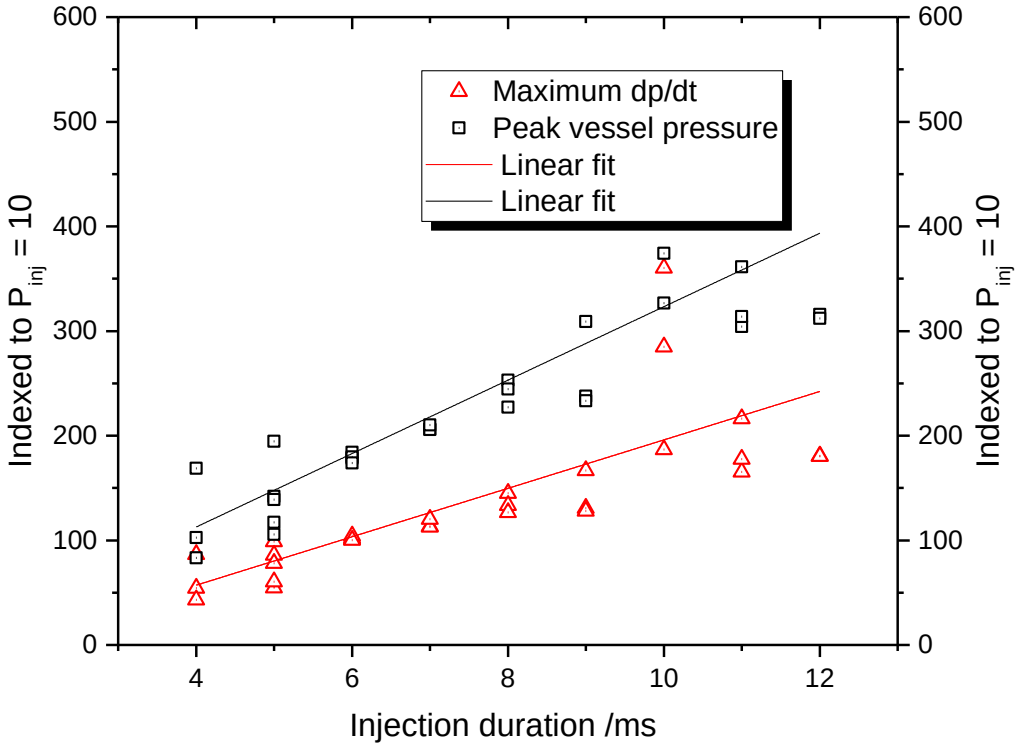

Figure 4.20: Linear increase in the indexed vessel pressure and maximum pressure time derivative with increasing injection duration

Although longer injections would increase the mass transfer, the nitrogen would require more time to completely evaporate. Evidence of this is shown in Figure 4.21 with the increase in the time it takes to reach the maximum pressurisation rate, with the increase in injection duration. Regardless of the injection pressure, the maximum

pressure gradient was achieved in less than 36 ms. Running at 1200 rpm, the engine would have 25 ms before BDC and the start of the exhaust stroke.

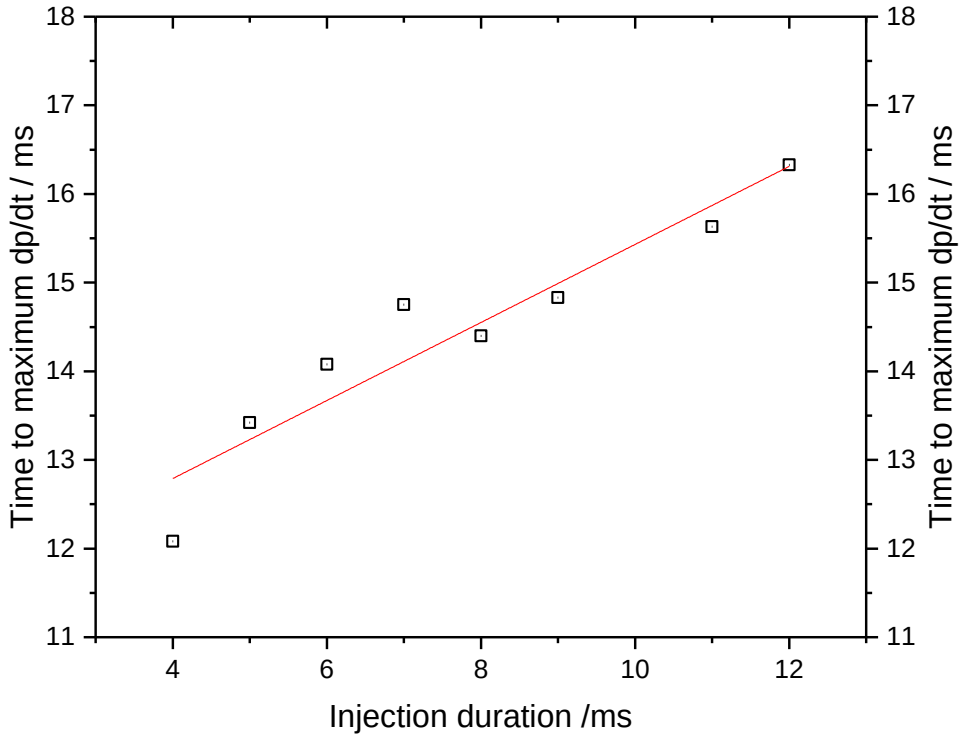

Figure 4.21: Time to maximum pressure time derivative with increasing injection duration for liquid injections at P_{inj} = 40 bar.

As such this may require a compromise between the speed and power of the engine. Lower engine speeds would allow more time for heat transfer between the HEF and nitrogen during the expansion and therefore increase engine efficiencies. As the injection valves would run directly from the driveshaft via a timing belt(26), higher speeds would result in a shorter injection time period and as such lower injected mass. An engine running at 1200 rpm would require an injection period less than 5 ms assuming the first 36° of the piston cycle in the expansion stroke.

Based on the gathered data, an injection period of 10 -12 ms was recommended for maximum valve lift and to allow for enough time for complete evaporation of the

injected nitrogen. The use of multiple engine cylinders could be explored as a way to meet the engines power requirement at higher speeds. This demonstrates the fact that the engine is best suited as a secondary dual purpose engine to provide auxiliary power and a cooling/air conditioning system. Therefore one can say the injection need only be optimised for power and not speed.

4.3 Discussion of injection results

The experimental data showed an increase in the rates of pressurisation which were 10 times greater than those presented in most recent work (21, 22). This is mainly because of the reduced expansion volume in the vessel and the increased injection pressure.

Under these circumstances, the increasing pressurisation cannot be described by the simple equation of state, because it does not apply at low temperatures. Although more complex equations of state(80) have been developed to provide a more comprehensive description of the thermal physical information of nitrogen, they cannot be easily differentiated to obtain any rates of change. Additionally, the reduced expansion volume and increased water volume has a strong influence on the jet breakup, which clearly provides some enhancement of the mixing and heat transfer. A reduction in the water mass could be seen to reduce the entrainment during the jet propagation as which was initially highlighted by Clarke et al(22). The use of a denser fluid such as water (instead of air) drives the onset of turbulence and promoted mixing between the two fluids.

Therefore, the injection pressure has a more prominent effect on the pressure gradient because of the increased impact velocity that facilitates further turbulent mixing of the fluids and enhances heat transfer as observed in earlier studies(43). Additionally, the high jet velocity could assist the breakup of the formed vapour cloud, which would release the unexpanded nitrogen and allow for their direct contact with the water.

At such high pressure, the valve flow will be more susceptible to thermal and dynamic effects such as cavitation which may increase the possibility of two-phase flow and such, affect the injected mass. A great deal of research has been published on the flow characteristics of the poppet valves (81, 82), but it is difficult to draw a comparison especially where the flow characteristics were dependent on the consistency of the single-phase fluid properties. So, although the use of a poppet valve for the intake has allowed for increased flow area, a better understanding of the two-phase flow characteristics is essential in the ability to predict the valve flow coefficient at different flow conditions in order to optimise the performance of the engine.

4.3.1 Boiling heat transfer analysis

The different boiling regimes can be characterised by pressurisation rates in the vessel as shown in Figure 4.22. The first stage is associated with the mass transfer of the nitrogen into the free volume and more importantly, the intense heat transfer driven by the boiling of the injected stream in the air and its impact on the water surface, resulting in the rapid rise in pressure. The jet breakup is mainly driven by the entraining of water closer to the valve as well as the impact from the vessel walls. Studies observed the formation of ligaments due to Kelvin–Helmholtz instability, which was evidence of the breakup of the injected stream to influence of viscous and aerodynamic forces (22).

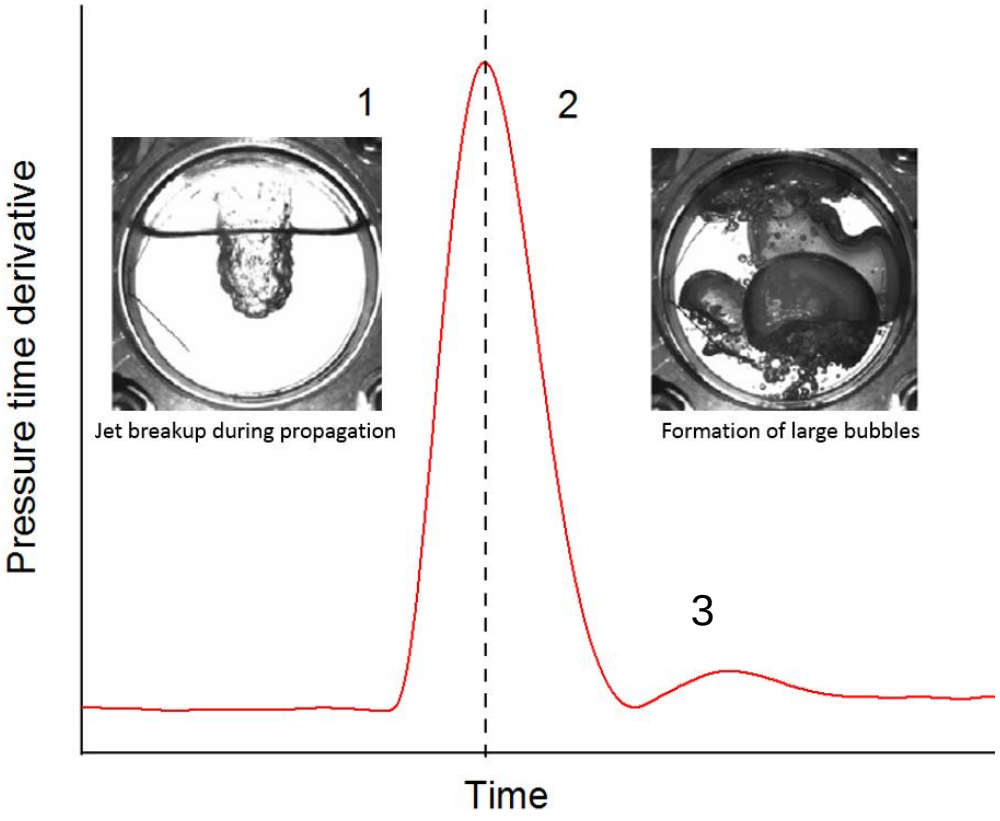

Figure 4.22: Pressure time derivative corresponding to the two main boiling stages of the liquid nitrogen

The second stage is associated with the formation of small then larger bubbles as buoyancy takes over forcing them to the surface. Smaller droplets of unexpanded nitrogen are thought to be encased within the bubbles restricting any further heat transfer resulting in a decrease of the pressurisation. The breakup of these bubbles is driven by further turbulence in the vessel releasing any encased nitrogen droplets.

Accordingly, the curves display a smaller peak labelled 3, which is evidence of this or the continued expansion of the nitrogen gas as it approaches room temperature.

The different regimes of convective heat transfer recognised during the pressurisation are film boiling at the beginning, followed by transition boiling and nucleate boiling towards the end. A large temperature gradient during this early stage results in the formation of a vapour film/layer typical of film boiling shown by curve DE in Figure 4.23. The generated bubbles form a continuous film between the water and the nitrogen, and as the vapour phase presents a greater thermal resistance, the heat flux decreases. The heat flux during film boiling starts off high and is greatly dependent on the thickness of the vapour film, which explains the rapid decline in the pressure gradient.

With time the temperature difference between the two steams falls to the point of the lowest heat transfer rate (Leidenfrost point) as shown point D. The vapour film eventually breaks up because the temperature gradient cannot sustain the layer. This causes the remaining nitrogen to come into contact with the water, leading to the onset of transition boiling. With the contraction of the film, the nitrogen is able to participate in convective heat transfer causing an increase in the heat flux despite

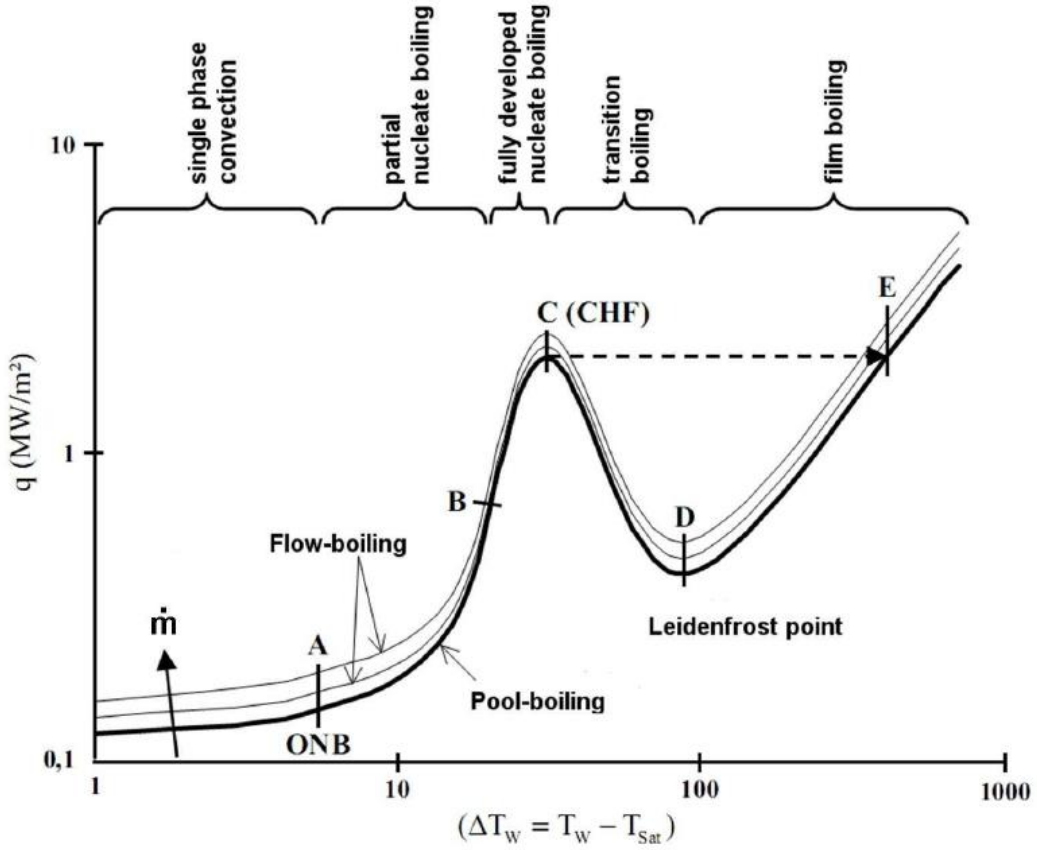

Figure 4.23: Pool boiling regimes according to Nukiyama's boiling curve (image reproduced from (1))

the decreasing temperature gradient. This would explain the second peak in the pressure time derivative.

Transition boiling is very unstable and is still the least understood of the several boiling mechanisms under a constant heat flux boundary condition. Experiments in the area are difficult and no accepted correlation exists for this region except for water(83). However, the duration of the boiling regime is very short and as a result, the accumulative vapour generated is very small in comparison to others(84). In the nucleate boiling regime, isolate bubbles detach from their nucleation sites which is usually strongly dependent on the roughness of the heating substrate. Evidence of this was also observed in previous visual experiments (22). The large bubbles of

nitrogen broke up into smaller ones that were forced upwards by buoyancy forces as shown in Figure 4.22. Heat transfer coefficients, based on the assumption of the contact area, reported in literature were comparable to values on the boiling heat transfer over very rough surfaces(21). This would explain the formation of several large and small bubbles reported in recent work(22).

The heat transfer rate in injection 49 is 0.9 kW, which gives a value of 5 W/K for hA for a temperature difference of 180 K. To determine the heat transfer coefficient and the heat flux, I assumed that the nitrogen makes contact with at least 50 % of the water surface, which is 6×10^{-3} m. This gives values of 0.8 MW/m^2.K and 144 MW/m^2 respectively. These results were found comparable, in the order of magnitude, to the film boiling of subcooled water on surfaces heated to > 723 K (85, 86). The study showed a strong correlation between the instantaneous heat transfer coefficient and dimensionless surface temperature that was found to increase with sub-cooling and surface area.

These results are based on the minimum values and the assumption that the nitrogen does not penetrate the water surface. Additionally, the actual values will vary with time because the contact area will be influenced by the jet dynamics and will increase as the jet continues to disintegrate in the water.

Nonetheless, these values are a kilowatt greater in magnitude compared to those presented in previous work (1) despite the similar contact area and temperature difference. This suggests that the increased heat transfer rate is mainly due to the

result of the increase in injection pressure, thus increasing the mass flow through the valve and the mixing process in the vessel.

However, it is also likely that due to the ill-defined and transient nature of the interfacial contact area, previous estimates of the heat transfer coefficient would be too low. There are studies in literature from which to draw a comparison for the flow area(82) of the valve, but not for the contact area as this valve type has never been used in such as an application.

4.1.1 Thermodynamic heat transfer analysis

The heat transfer is analysed by looking at the interaction between three systems, the injected nitrogen, the ambient nitrogen and water inside the vessel before and after injection. Based on the first law of thermodynamics, the energy equation for each system is written as:

$$\left({U_L}^2 - {U_L}^1\right) = Q_{G-L} + Q_{L-W} + Q_{other} - W_{L-G} - W_{L-W} \quad 4.4$$

$$\left({U_G}^2 - {U_G}^1\right) = -Q_{G-L} + Q_{W-G} + W_{L-G} - W_{G-W} \quad 4.5$$

$$\left({U_W}^2 - {U_W}^1\right) = -Q_{L-W} - Q_{W-G} + W_{L-W} + W_{G-W} \quad 4.6$$

where the change in the internal energy of each system is equal to the heat added minus the work done by the system. Superscripts 1 and 2 represent the liquid, gas and water before and after the injection respectively.

Despite the insulation, it is very likely that a significant amount of heat is transferred to the liquid nitrogen in the injector prior to injection. This is accounted for as Q_{other}.

Other assumptions include:

- No heat transfer between the water, gas and apparatus due to the very low temperature difference and therefore Q_{other} is left out of Equations 4.5 and 4.6.
- The ambient nitrogen gas and water are initially at the same temperature and hence Q_{W-G} = 0.
- As a closed system, the water and gas does no work

By solving for Q_{other}, Equations 4.4, 4.5 and 4.6 become Equation 4.7.

$$Q_{other} = \left({U_L}^2 - {U_L}^1\right) + \left({U_G}^2 - {U_G}^1\right) + \left({U_W}^2 - {U_W}^1\right) \qquad 4.7$$

To determine the work done by the liquid, we also assume that the pressure inside the vessel undergoes an isothermal compression post injection to the peak vessel pressure where the data is known.

Taking Test 11 at P_{inj} = 30 bar (Table 4.1) and a peak pressure of 90 bar, the total heat transfer to the liquid nitrogen is 3.9 KJ with 53 % coming from water, 0.6% from the ambient air and 46 % from the injection apparatus. This shows that there is a considerably high heat transfer from the injection apparatus. However, this can be advantageous if the heat transfer is controlled to limit it to occur after the injection.

These percentages agree with previous work, which was due to the control of the injection parameters made possible by the test rig used. The total heat transfer is expected to increase with the increase in the injected mass that results in the larger temperature difference and consequently changes in ΔU.

4.1.2 Implication to the performance of the engine

The experiments conducted were designed to simulate the injection of liquid nitrogen in the cryogenic engine. Based on a dead volume of 400 mL used in this study and with a more realistic injection period of 10 ms, the results showed specific work output of 0.32-0.58 MJ/kg and therefore engine efficiency of 46 -83 % based on Equation 2.4. However, this does not account for the energy expelled in pumping, cooling and pressurisation of nitrogen in the injector.

The paths taken involving the isothermal expansion and heat exchange are plotted on the PV diagram (Figure 4.24). The nitrogen from the onboard storage is slightly pressurised so as to deliver it to the buffer at about 3 bar (1-2). This eliminates the need for cryogenic pumps, which would decrease engine efficiencies. Previously nitrogen was pressurised prior to injection using ambient air but injection resulting in a cold gas injection (2-3). The sub-cooling applied here, condenses the pressurised nitrogen resulting in liquid injections at high pressure (1 – 1A). Post-injection, the third pressurization occurs in the engine cylinder after mixing with the heat transfer fluid with the piston at TDC (1A -4D). The isothermal expansion of the nitrogen results

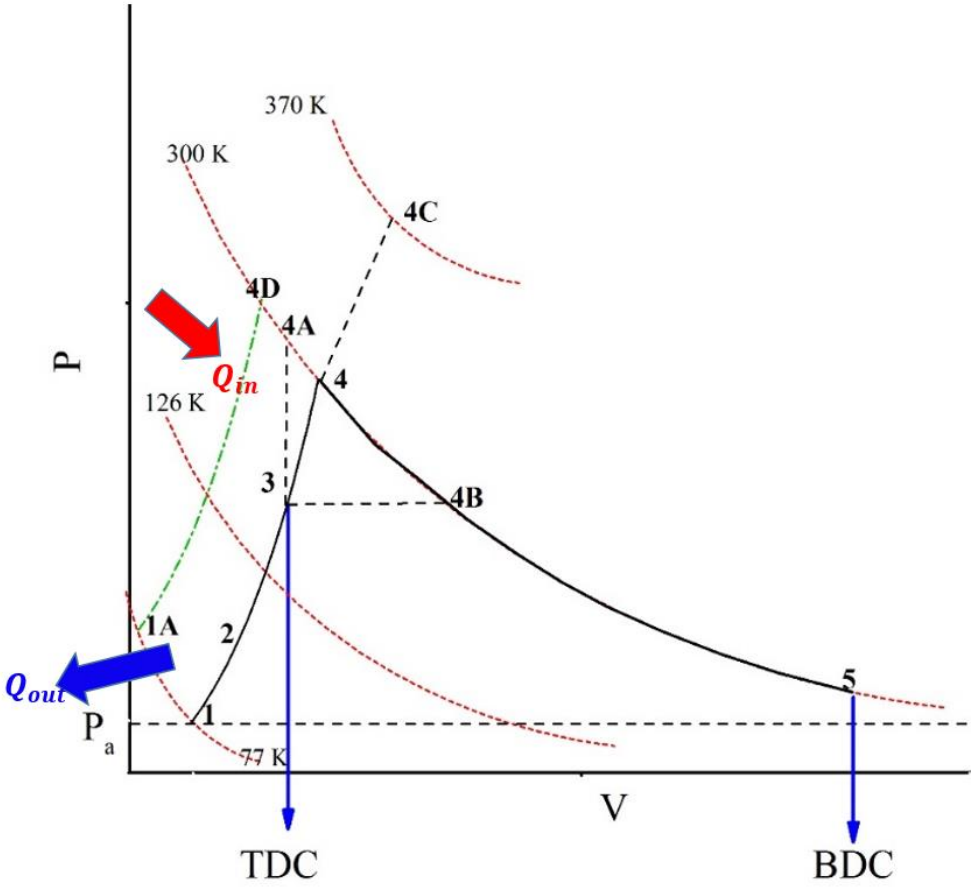

Figure 4.24 : PV diagram of nitrogen working cycle where expansion occurs between TDC and BDC.

in a power stroke, which moves the piston to BDC (4D-5). An isothermal expansion increases the engine output, but it requires a large heat reservoir capable of supplying the necessary heat needed for the process to occur at an increased rate. Some heat will be transferred to the nitrogen from the cylinder walls but would be small compared to that transferred from the HEF. The work done by the engine with and without the addition of sub-cooling is shown by 11A4D5 and 12345, respectively. Although the initial and final states are the same, the work out put to the engine is greater.

The pressurisation due to the nitrogen-HEF exchange is a rapid process and ideally an isochoric one – 3-4a. This is less likely to occur unless the heat transfer is unrealistically high. This could be released by the increase of the HEF temperature. The work done by the cycle, the area under 3-4-5, can be increased by the heat addition at 4c from waste heat from the primary engine.

Although not shown in this study, an increase in HEF temperature is bound to increase the heat transfer process in the engine. In a hybrid configuration, the exhaust heat can be used to raise the HEF temperature before it is injected into the engine. With exhaust temperatures of up to 500 K, care must be taken so as not to exceed the boiling point. This is because the use of multiphase HEF would alter the expansion ratios due to the changes incompressibility, and the condensation as it cools would decrease the pressure inside the cylinder(1).

The use of a cascading cycle was suggested in earlier work(35, 87) however, further system optimisation was required to offset the gained efficiency with the system complexity. As an alternative, this work suggests the addition of a passive sub-cooling system prior to injection as it will not only increase the output but also eliminate the need for a cryogenic pump (usually 80 % efficiency), which would limit the overall efficiency of the engine.

In contrast, while such an injection system would be ideal, it may increase the complexity of the feed system and may not be feasible for a dynamic application where speed is a vital requirement. At high pressure, the work required for pumping

would be a significant impact on the overall efficiencies, especially when operating at high flow rates with an increased density associated with single-phase flow.

In light of this, the gains achieved may be marginal compared to the costs and complexities involved in bringing the nitrogen to its injection state. The practicality of direct injection was thought to be impossible mainly due to issues related to valve control. Valve timing mechanism used in steam engines were considered for the cryogenic engine because they operate in the same way. They traditionally used complicated rigid body link mechanisms that were capable of changing the valve opening time(88). An electronically controlled valve system that used a solenoid or piezoelectric actuated valves was considered previously but, in comparison to petrol and diesel, the engine requires a rapid valve opening and large motions which prevented the use of off the shelf parts(1). The EHVA system used here provides the valve motion needed for this type of engine. In practice, it would need to be slightly modified to meet the size and weight requirements for an automobile application.

4.4 Chapter summary

Previous work on the injection of liquid nitrogen into water showed that attaining higher peak cylinder pressure is clearly beneficial, but the best way to achieve this was still ambiguous. The designed injection rig allows for the controlled injection of nitrogen at different thermodynamic states, which reveals the effect of various injection parameters based on the synchronized pressure and temperature measurements. The results from this Chapter can be summarised as:

1. Injections of nitrogen in its gas, liquid and supercritical states are compared and showed that the phase change process and latent heat transfer contribution play significant roles in the final peak pressure and maximum pressure time derivative.
2. The pressurisation rates increased with a decrease in the expansion ratio / free volume.
3. Results showed an almost linear correlation between the pressurisation rate and injection pressure for liquid nitrogen injections conducted between 10 – 80 bar. The effect of the injection pressure on the maximum pressure time derivative is still prominent even when other factors are relaxed. The maximum pressurisation rate is recorded at 5156 bar/s at an injection pressure of 76 bar which is 14 times that recorded in previous studies(22) .
4. The maximum specific work achieved in these tests was 0.58 MJ/kg or 161 Wh/kg at an injection pressure of 30 bar and a sub-cooing ratio of 0.705, based on the optimisation of pressure, temperature, and injection duration.
5. The injected mass increased with greater subcooling as a consequence of the increased flow density during the injection. However, lower temperatures became difficult to achieve at higher injection pressures.
6. Shorter injections and reduced valve lift significantly reduce the nitrogen injected thus compromising the peak pressure and maximum pressure time derivative in the engine. On the other hand, leaving the valve opened too long resulted in reverse flow in the injection feed line as the pressure continues to rise in the vessel. An injection duration of 10 ms at a maximum

valve lift of 1.2 mm was used in the majority of the injections for effective injection mass transfer into the vessel.

CHAPTER 5

5 Computational simulations of the injected jet and droplet evaporation

Computer fluid dynamics (CFD) is used to increase our understanding of the two-stage boiling heat transfer characterised by the pressure build-up discussed in Chapter 4. CFD is specifically an attractive analysis tool in this case because of the lack of visualisation of the injection and film boiling process during experiments. Parameters and controls can be altered instantaneously once the model is established, providing more comprehensive and quantitative data on a whole. The injection of liquid nitrogen into water presents a challenging CFD problem involving the heat and mass transfer between multiple phases that is; liquid nitrogen, gaseous nitrogen and water in the confinement of the vessel walls. Additionally, the problem calls for a transient analysis due to the evolving flow regimes as a function of time. The commercial CFD package, Fluent, was used to investigate hydrodynamic and heat transfer interactions between the fluids inside the engine cylinder.

As characterised in Chapter 4, the first boiling stage is associated with the flow behaviour and jet break up due to the impact with the water surface and possibly the piston head depending on the volume of water, while the second is related to the boiling of liquid nitrogen droplets within the formed vapour cloud beneath the water surface.

It was impossible to visualise the behaviour of the jet core or the droplet evaporation during experiments however, the hydrodynamic and thermal behaviour of the injection is important to fully understand the pressurisation inside the engine cylinder. CFD modelling is used to study these two important aspects of the injection process that is: the jet dynamics of liquid core and the boiling of liquid nitrogen droplets within its own vapour cloud.

Accordingly, this chapter is divided into two sections. The first section 5.1 presents the simulation of the injected jet starting with a description of the mathematical formulation of the CFD 2D Eulerian multiphase model that was used. This is followed by the description of the geometry, mesh and boundary conditions applied. Section 5.1.3 presents the results, with a discussion on the influence on the injection pressure on the core length, jet penetration and mixing below the water surface. The second Section 5.2 presents CFD simulations of evaporation of a liquid nitrogen drop in water using the Volume of Fluid model. The geometry, mesh and boundary conditions are presented, and the results discussed in thereafter. The chapter is concluded with a summary of the findings and their implications to the injection process.

5.1 Flow dynamics and jet break up

The complexity of this fluid dynamic problem is down to the interactions between the multiple phases inside the vessel. These include not only the liquid nitrogen, water and the nitrogen vapour formed, but also the warm air already present in the vessel and solid surfaces that come into contact with the fluids. To simply the

problem several assumptions were made, and individual correlations were chosen to describe the heat transfer between each fluid/phase as shown in Table 5. 1.

Assumptions:

- No heat transfer between the vessel walls and water as well as the air and water
- Atmospheric pressure in the vessel during the injection
- Incompressibility of liquid and gas nitrogen that remained at a fixed density
- With no information on the liquid nitrogen droplet size, a value of 0.01 mm was used in the phase properties

The analysis of the jet focus on two main regions as shown in Figure 5.1:

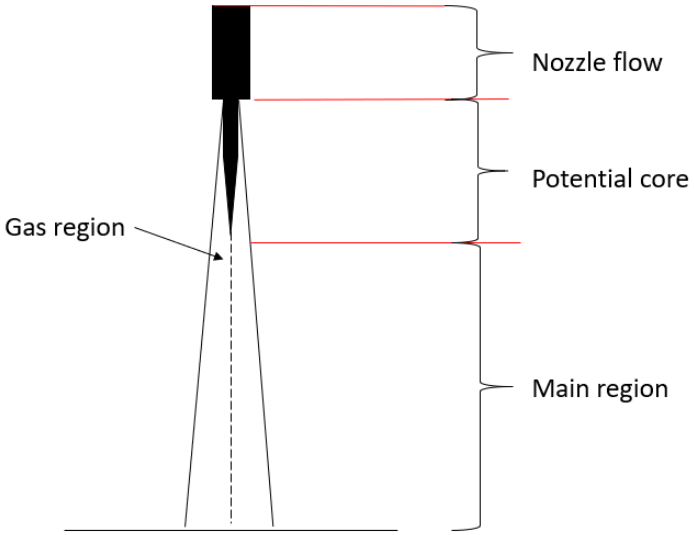

Figure 5.1: Anatomy of the injected jet showing the core and gas region

1. The core region close to nozzle exit which experiences instabilities and resulting in the breakup of the continuous stream into smaller droplets

2. The gas region formed by the vapour layer as a result of film boiling of the core

5.1.1 Mathematical formulations

The Eulerian-Eulerian multiphase flow model was used to simulate the injection of liquid nitrogen into water. The notion of multiphase flow incorporates the concept of the phasic volume fractions expressed by α_q, to represent the space occupied by each phase in the domain. For example, the effective density of phase q is:

$$\hat{\rho}_q = \alpha_q \rho_q \qquad 5.1$$

where ρ_q is the physical density of phase q.

The volume fraction may then be solved either through implicit or explicit time discretization. The governing equations of computational fluid dynamics are non-linear with several unknown variables and are therefore solved iteratively as shown in Equation 5.2.

$$Q_{n+1} = Q_n + dtS \qquad 5.2$$

where Q_n is the variable at time n and S is the rate of change of Q.

The implicit scheme evaluates all the terms of unknown quantities at a new time step $n + 1$. It can be used for both transient and steady-state calculations but, is mainly used to allow for a larger time step and allows for better stability. Transient calculations are far more complex and require more computational effort because an implicit solution requires the solution of several simultaneous equations for the entire grid at each time step (80).

Alternatively, the explicit approach evaluates the dependent variables from the known quantities at the previous time step n. An explicit solution was used due to the time-dependency of this transient problem. On the other hand, the solution required a time step that limited the advancement of pressure to less than one computational cell per time step. Although this method is more prone to high instability, convergence was achieved by reducing the courant number(C) whereby; $C \equiv \frac{\dot{v}\Delta t}{\Delta x} \leq 1.$

In the immiscible Eulerian model, Navier-Stocks equations are solved for each phase as well as tracking of the fluid interface(1). The continuity equation remains unchanged, while the momentum (Equation 5.3) and energy equations account for changing volume fraction of each phase.

$$\frac{\partial}{\partial t}\left(\alpha_q \rho_q \vec{v}_q\right) + \nabla.\left(\alpha_q \rho_q \vec{v}_q \vec{v}_q\right) = -\alpha_q \nabla p + \nabla.\bar{\bar{\tau}}_q + \alpha_q \rho_q \vec{g} + \sum_{p=1}^{n}\left(\vec{R}_{pq} + \dot{m}_{pq}\vec{v}_{pq} - \dot{m}_{qp}\vec{v}_{qp}\right) + \left(\vec{F}_q + \vec{F}_{lift,q} + \vec{F}_{vm,q}\right) \quad 5.3$$

where

$$\bar{\bar{\tau}}_q = \alpha_q \mu_q\left(\nabla \vec{v}_q - \nabla \vec{v}_q{}^T\right) + \alpha_q\left(\lambda_q - \frac{2}{3}\mu_q\right)\nabla.\vec{v}_q\bar{\bar{I}} \quad 5.4$$

where $\bar{\bar{\tau}}_q$ is the stress -strain tensor for the phase q and μ_q and λ_q are the shear and bulk viscosities, $\vec{F}_q$ is an external body force, $\vec{F}_{lift,q}$ is a lift force and $\vec{F}_{vm,q}$ is the virtual ass force.

The lift force acts on the nitrogen droplets or bubbles of the secondary phase due to the velocity gradient brought on by the primary phase flow. In most cases, the lift force is insignificant in comparison to the drag force and is often excluded. However, it is considered if when the phases separate quickly. The lift force is given by Equation 5.5 where the lift coefficient (C_l) is taken as 0.3 for the simulations from experiments on air bubbles in glycerol-water solutions(89). In this case, the lift was ignored as it introduced instability and it was insignificant in comparison to the drag.

$$\vec{F}_q = -C_l \rho_q \alpha_q \left(\vec{v}_q - \vec{v}_p\right) \times \left(\nabla \times \vec{v}_q\right) \quad 5.5$$

The virtual mass accounts for the acceleration of the secondary phase through the primary phase. It is not usually included but is significant when the secondary phase has a significantly reduced density in comparison. The virtual mass is most significant when the secondary phase is a lot lighter than the primary phase such as in a bubble column (80), therefore it was ignored in this case.

The drag force $\vec{R}_{pq}$, between phase p and q, is expressed as Equation 5.6 where K_{pq} is the momentum exchange coefficient given by Equation5.6.

$$\sum_{p=1}^{n} \vec{R}_{pq} = \sum_{p=1}^{n} K_{pq} \left(\vec{v}_p - \vec{v}_q\right) \quad 5.6$$

$$K_{pq} = \frac{\alpha_p \alpha_q \rho_p f}{\tau_p} \quad 5.7$$

where τ_p represents a particle relaxation time (Equation 5.7) and f is the drag coefficient based on the Schiller and Naumann model which is the default model for fluid-fluid phase interactions(90). The model is mostly developed for laminar flow

and it is often recommended to use the symmetric drag law for Eulerian problems involving a free surface between phases. However, out of the two better convergence was achieved with the Schiller and Naumann model, which uses a constant value of 0.44 for the drag coefficient (Equation 5.10) for Re greater than 1000, making for faster calculation of drag function in each cell. Based on the flow rates (maximum of 0.5 kg/s) obtained from the experiments conducted in Section 3.2.1, the range of this model was a good starting point for the value of Re of the liquid nitrogen during the injection.

$$\tau_{pq} = \frac{\rho_p {d_d}^2}{18\mu_p} \tag{5.8}$$

$$f = \frac{C_d Re}{24} \tag{5.9}$$

where
$$C_d = \begin{cases} 24(1 + 0.15Re^{0.687})/Re & Re \leq 1000 \\ 0.44 & Re > 1000 \end{cases} \tag{5.10}$$

and
$$Re = \frac{\rho_q |\vec{v}_p - \vec{v}_q| d_p}{\mu_q} \tag{5.11}$$

The energy equation consists of the total energy and mass transfer from phase q to phase p as shown in Equation 5.12 with the right side of the equation representative of the heat transfer. Therefore, the energy equation for phase q is given by:

$$\frac{\partial}{\partial t}(\alpha_q \rho_q h_q) + \nabla.(\alpha_q \rho_q \vec{u}_q h_q) \tag{5.12}$$

$$= \alpha_q \frac{\partial p_q}{\partial t} + \bar{\bar{\tau}}_q . \nabla \vec{u}_q - \nabla \vec{q}_q$$

$$+ \sum_{p=1}^{n} (\dot{Q}_{pq} + \dot{m}_{pq} h_{pq} - \dot{m}_{qp} h_{qp})$$

The exchange of heat is driven by the temperature difference between the two nitrogen phases and expressed as:

$$\dot{Q}_{pq} = h_{pq}(T_q - T_p) \quad 5.13$$

$$h_{pq} = \frac{6k_q\alpha_p\alpha_q Nu_p}{d_p^2} \quad 5.14$$

Accordingly, Equation 5.14 shows that the heat transfer rate is not affected by the thermal conductivity of the water but rather only that of the gaseous phase.

The Nusselt number given by the Ranz and Marshall correlation shown in Equation 5.15 (91) which is used to estimate the heat transfer coefficient. The correlation describes the heat transfer of a spherical droplet/particle and a surrounding gas plasma and was proposed because it is based on experimental data on the evaporation of water droplets in hot air. The study was limited to a Reynolds number between 0 to 200, droplet diameters between 0.06 - 0.11 cm and air temperatures of 220 ℃. Once again, the Reynold's number is based on the relative velocity between the gas fluid and the droplet. With the water a zero velocity, this value is assumed to be relatively low making the correlation suitable.

$$Nu_p = 2 + 0.6Re_d^{1/2}Pr^{1/3} \quad 5.15$$

The Lee model within the Eulerian model is used when the liquid -vapour mass transfer (in this case evaporation) is governed by the vapour transport equation:

$$\frac{\partial}{\partial t}(\alpha_v\rho_v) + \nabla.(\alpha_v\rho_v\vec{v}_v) = \dot{m}_{lv} - \dot{m}_{vl} \quad 5.16$$

The mass transfer $(\dot{m}/A_s)$from liquid to gas is calculated by the Hertz Knudsen equation (92) which follows the kinetic theory for a flat interface. The mass flux is expressed as:

$$\frac{\dot{m}}{A_s} = \frac{\beta(p^* - p_{sat})}{\sqrt{2\pi R M_{RMM} T_{sat}}} \quad 5.17$$

where β is the accommodation coefficient that indicates the fraction of vapour molecules destined for and absorbed by the liquid surface and p^* denotes the partial pressure on the vapour side of the interface.

The Clapeyron Clausius equation (Equation 5.18) relation allows us to obtain the variation of temperature from the variation of pressure close to the saturation condition(90). Therefore, assuming the pressure and temperature are close enough to the saturation point, the mass transfer is calculated using Equation 5.19 in terms of the evaporation coefficient(C_v). The accommodation coefficient (β) and bubble diameter $\left(d_p\right)$ are often know n in literature from empirical correlations. The default value for (C_v) of 0.1 usually adequate for most flows(63) however could range between 0-10.

$$\frac{dp}{dt} = \frac{h_{fg}}{T(v_v - v_l)} \quad 5.18$$

$$\dot{m}_{l\to v} = C_v * \alpha_l \rho_l \frac{(T_l - T_{sat})}{T_{sat}} \quad 5.19$$

where

$$C_v = \frac{6}{d_b}\beta\sqrt{\frac{M_{RMM}}{2\pi RT_{sat}}}\ L\left(\frac{\alpha_v\rho_v}{\rho_l - \rho_v}\right) \quad 5.20$$

The symmetric model was used to define the interfacial area (A_i) between the two phases, which is used in predicting the mass, momentum and energy transfers through the interface between the phases (78). This model was chosen because it ensures that the interfacial area approaches zero as the dispersed/secondary phase volume fraction approaches 1 as shown in Equation 5.21.

$$A_i = \frac{6\alpha_p(1-\alpha_p)}{d_p} \quad 5.21$$

Initially, the heat transfer between the water and the liquid nitrogen was ignored (in Cases 1-9 shown in Table 5.2) so as to determine the hydrodynamic effects of the surface impact on the jet break up and its propagation without the effects of heat transfer.

Due to the lack of extensive literature or heat transfer correlations to quantify the heat transfer between water and liquid nitrogen, a few assumptions were made. A constant heat transfer coefficient approximated from 53% of the total heat transfer to the nitrogen as calculated from the experiments in Chapter 4. Consequently, the heat transfer area is assumed to be cylindrical $(A = \pi rh + \pi r^2 \approx 9 \times 10^{-4}\ m^2)$, where h is the unbroken length of the injected jet, which was half the depth of the water. The contact area relies heavily on the assumption that the jet is jet is able to penetrate the water to this length. Justification of this was later discussed in the results section below.

Based on these assumptions, the heat transfer between the water and the nitrogen jet is investigated in Case 10. The heat transfer interaction between each phase is described in Table 5.1.

Table 5.1: Heat transfer correlations and input parameters

Heat transfer from	Heat transfer to	Correlation used
Water	Liquid nitrogen	Constant $h = 1000\ {}^{W}/_{m^2K}$
Water	Gaseous nitrogen	Ignored
Air	Liquid nitrogen	Ranz and Marshall
Air	Gaseous nitrogen	Ignored
Vessel Walls	Liquid and gaseous nitrogen	Constant wall temperature = 300 K

5.1.2 Simulation approach

5.1.2.1 Geometry

The analysis was simplified with a 2D axisymmetric geometry due to the complexity of the three-phase interaction. Consequently, the movement of any mechanical parts was omitted from the simulation. In this study, the injection of nitrogen upon the opening of the valve is postulated to consist of multiple infinitesimal small jets. Therefore, the analysis focusses on the behaviour of a single jet to provide a better understanding of the bulk flow behaviour. The geometry of the domain was a 50 x 65 mm rectangular vessel with a 1.2 x 15 mm nozzle was used as shown in Figure 5.2. Liquid nitrogen through a 1.2 mm nozzle depictive of the maximum valve lift of the poppet valve in the experiments.

5.1.2.2 Mesh

A structured mesh consisting of 22600 elements quadrilateral cells was generated for the computational domain (Figure 5.2) for better convergence and the reduced computational memory that is required.

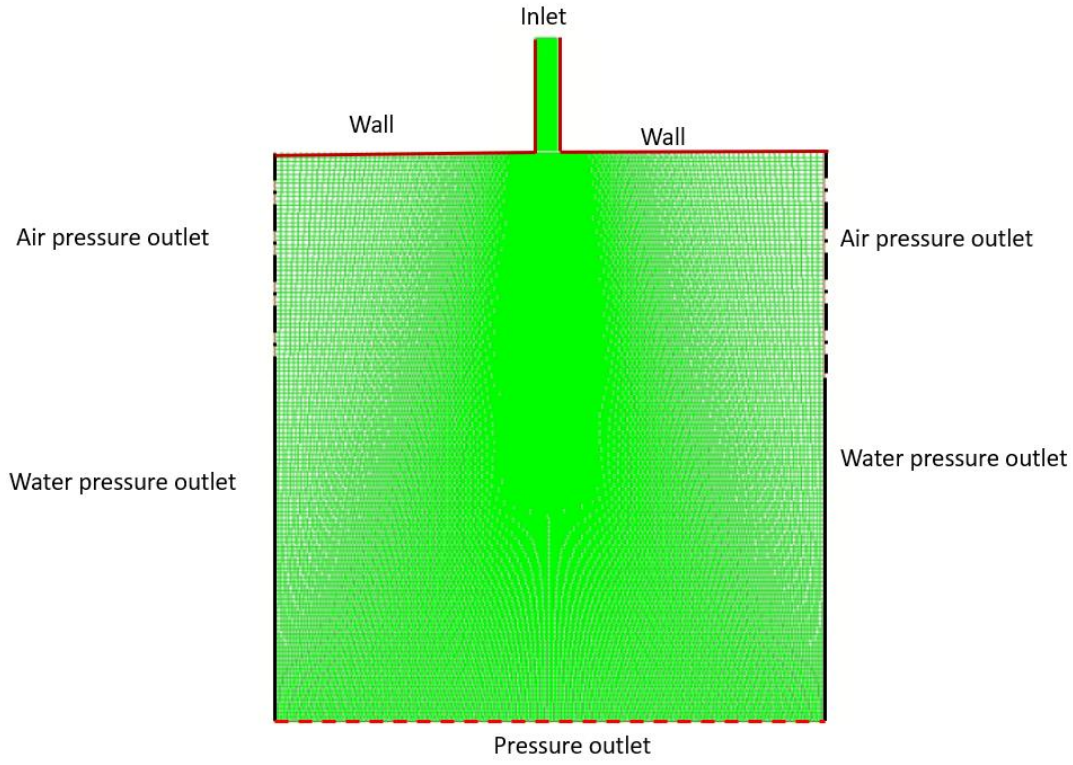

Figure 5.2: Geometry, mesh and boundary conditions

5.1.2.3 Boundary and initial conditions

An attempt was made to model the injection into a closed volume, but despite changes to the solver, relaxation factors, and the mesh itself, the solution failed to converge. Instability was thought to be caused by the compressible treatment of the gas phase based on the ideal gas law, that solves for the fluid density based on the pressure and temperature in the cell (1). This was also due to the inaccuracy of the

well-known equation of state at temperatures below 250 K(80), allowing for large error in the iterative values of the cell variables.

It was also impossible to simply omit the pressure dependency to simulate the injection because of the immediate pressure imbalance inside the vessel as an immediate and direct result of the liquid nitrogen inflow.

To combat this, the walls of the vessel were set with a pressure outlet boundary condition to create an infinite pool of water into which the nitrogen was injected as shown in Figure 5.2. Additionally, to maintain the water free surface, the walls were divided into two separate boundary conditions. This was done to prevent the backflow of ambient gas into the water and vice versa.

The inlet boundary condition was assigned a pressure inlet using a User Defined Function (UDF). The pressure was set to replicate the gradual opening of the valve as shown by the LVDT in Chapter 4. Since the majority of those experiments were conducted at an injection duration of 10 ms, the pressure was set to increase linearly as a function of time. The maximum injection pressure is attained at the midpoint (5 ms) before it gradually drops back down to zero as the valve closes.

The nozzle walls were assigned a no-slip boundary condition as used in previous works (83), which would lead to the formation of a velocity boundary layer as expected during the flow. A conductive heat transfer condition was applied to the walls of the nozzle whose walls were set to a constant temperature of 300 °K. The heat transfer to the wall was calculated by Equation 5.22.

$$q_{wall} = h_l(T_w - T_l) \quad 5.22$$

The air was defined as the primary phase whilst the water and liquid nitrogen were defined as secondary phases. The simulation was initialised with the water patched to the lower half of the domain.

The water is fixed at 70 % of the vessel volume and the injection pressure/velocity and evaporation coefficient (C_v) were varied to determine the mostly qualitative effect of the liquid nitrogen volume and heat transfer. The following cases were simulated, and the results are presented and discussed below. Note that the fluid properties, density, viscosity and specific heat are obtained from NIST data(93).

Table 5.2: Simulated cases and computational conditions

CASE	P_{inj}(bar)	ρ_l (kg/m^3)	T_{AIR} (K)	C_v	T_w (K)
1.	50	820	300	10	300
2.	10	810	300	10	300
3.	20	810	300	0.1	300
4	20	810	300	2	300
5	20	810	300	100	300
6	20	813	300	10	300
7	20	813	300	10	300
8	20	813	200	10	300
9	50	820	200	10	300
10	50	820	300	100	300

5.1.2.4 Grid independence study

Grid dependency was conducted to determine the accuracy of the results. This was conducted for an injection pressure of 10 bar using the UDF function with a C_v= 10. The maximum mass transfer rate at the water level was used to determine the grid dependency. Mesh independence was achieved at 22600 cells and 22955 nodes as shown in Table 5.3.

Table 5.3: Grid dependency results

No. of nodes	No. of cells	Maximum mass transfer at water level $(\frac{kg}{m^3.s})$
15721	15420	2143
19780	19560	2149
22955	22600	2155
28430	28980	2157

5.1.3 Results

Simulations of high pressure and high-speed turbulent water jets in air were used ascertain the reliability and accuracy of the model. Even though water is a different fluid, at a similar density it can be used to reproduce the characteristics of the injected liquid nitrogen jet and as a benchmark for the results. Using the Eulerian model and the $\kappa - \varepsilon$ turbulence model in Fluent, their results reasonably predicted the flow physics of the water jets(94). At an injection velocity of 155 m/s, the results were in good agreement with the decrease of the water volume fraction at along the centre line as shown in Figure 5.3.

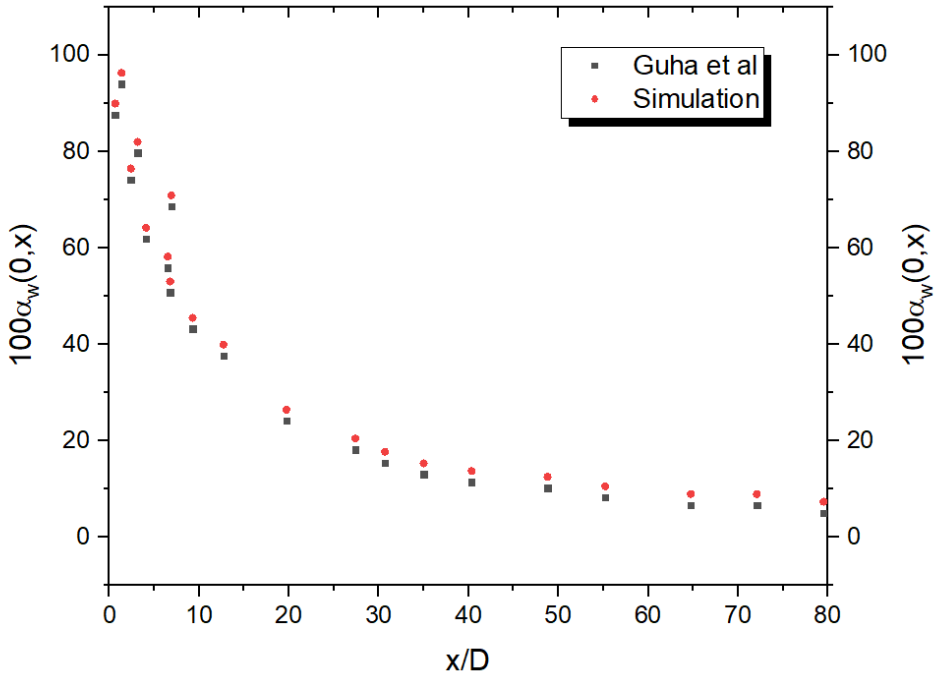

Figure 5.3: Numerical simulation of the decrease of the volume fraction of water at the centre line of the inlet in comparison to results from previous work (94).

5.1.3.1 Effect of injection pressure on jet propagation

In Case 1 shown in Figure 5.4, it was found that the jet exhibits a jet core of the liquid phase encased by the gas phase as it penetrates the water surface. This was in agreement with observations from previous visual experimental studies(1, 22). At 50 bar injection pressure, of velocity contour indicate a decreasing velocity gradient across the width of the jet due to the viscous effects brought on by the propagation of the jet through the stationary water.

The liquid phase velocity in the nozzle was reduced by heat transfer from the nozzle resulting in a reduced flow density. This makes the occurrence of two-phase flow inside the nozzle is very probable especially with increased injection velocity resulting in the onset of turbulence.

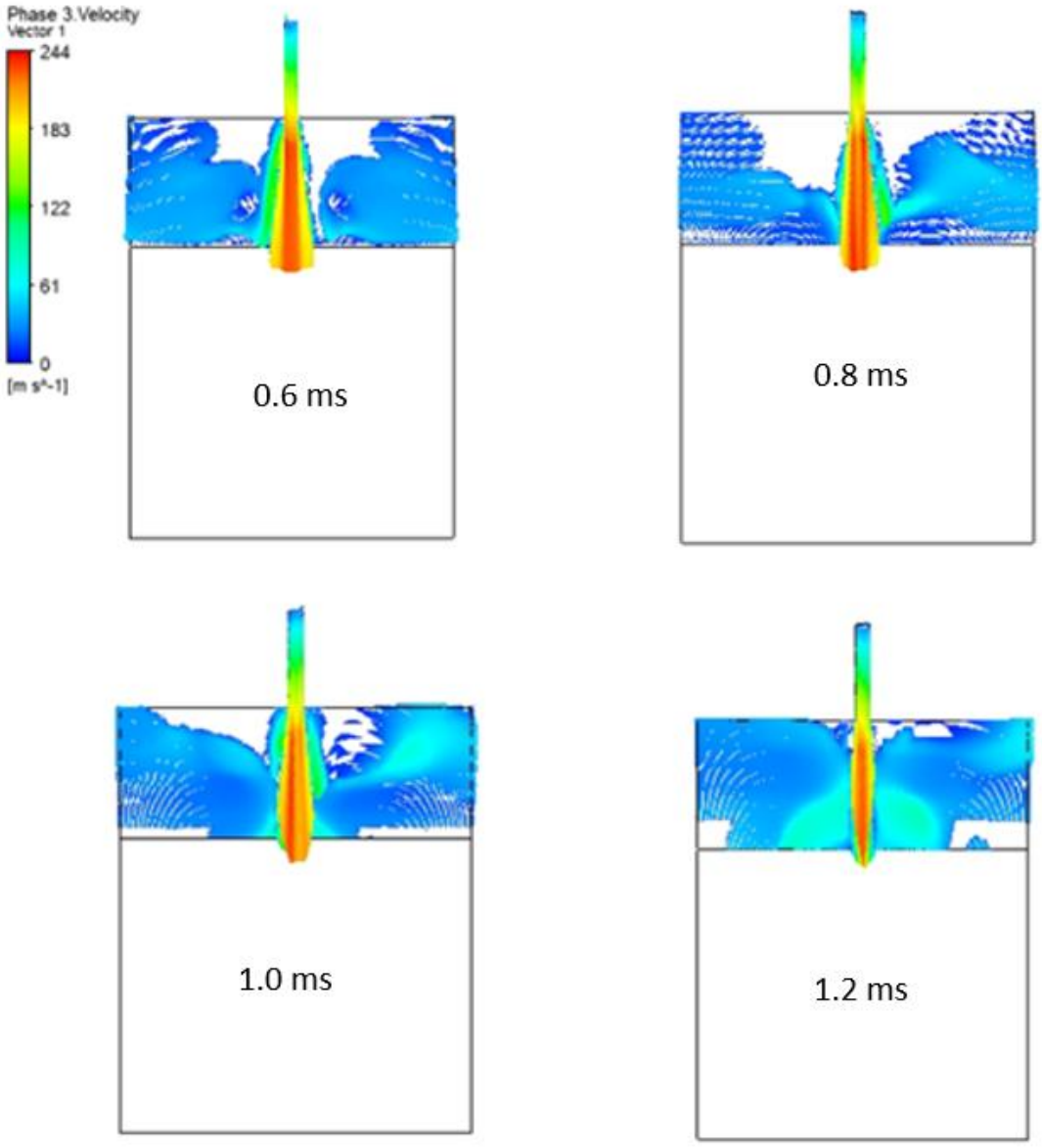

Figure 5.4: Velocity vector showing jet propagation at $\boldsymbol{P_{inj}}$ = 50 bar

On exit, the core regains its high flow velocity due to the limited heat transfer hindered by the vapour cloud surrounding it. The occurrence of cavitation is difficult to identify due to the constant evaporation of the liquid resulting in a persistent velocity and thermal gradient across the jet. Effects of cavitation would similarly result in the formation of vapour prior to the exit, which narrows down the flow and would significantly influence the shape and diameter of the emerging jet.

The model was able to capture the effects of flashing to some degree. Flashing often occurs as the pressure gradually approaches ambient and its occurrence causes the vapour to flow separately from the liquid, with the vapour at high velocity than the

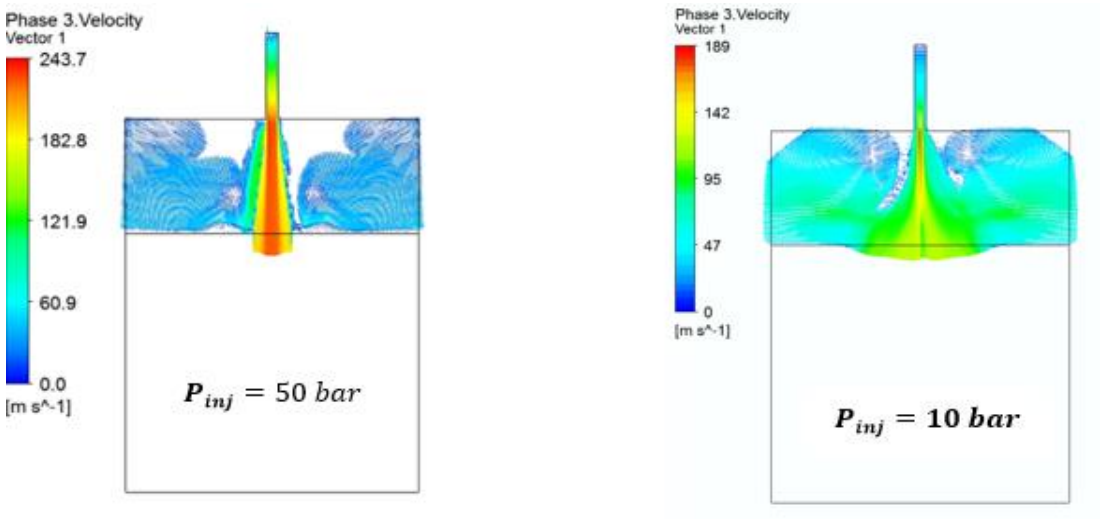

Figure 5.5: Contours map of velocities 6 ms into the injection of liquid nitrogen into a pool of water.

liquid. The increase in pressure greatly affects the occurrence of flashing and the lack of increasing back pressure in the vessel, makes it difficult to compare these results with what actually happens during the injection process. This can usually be modelled at a higher resolution by the Singhal et al cavitation model(63), but it was observed to introduce instability in the simulations causing divergence.

Case 1 and 2 were compared to demonstrate the effect of the injection pressure on jet propagation. Figure 5.5 shows that higher pressure increases the impact velocity of the jet core and inherently reduces the time it takes to reach the water surface. The leading tip of the jet is, therefore, able to penetrate the water surface at a higher velocity, resulting in increased propagation and mixing. At the reduced velocity, the results showed a reduced core length, which would lack the momentum to propagate through the water.

This is evident in the contour maps shown in Figure 5.6 after 12 ms, where a greater volume of the liquid phase is detected further below the water surface due to the increased injection pressure/velocity. Thus, confirming that the injection pressure increases the core length and the ability to initiate turbulence and enhance the mixing of the two fluids.

5.1.3.2 Effect of evaporation rate

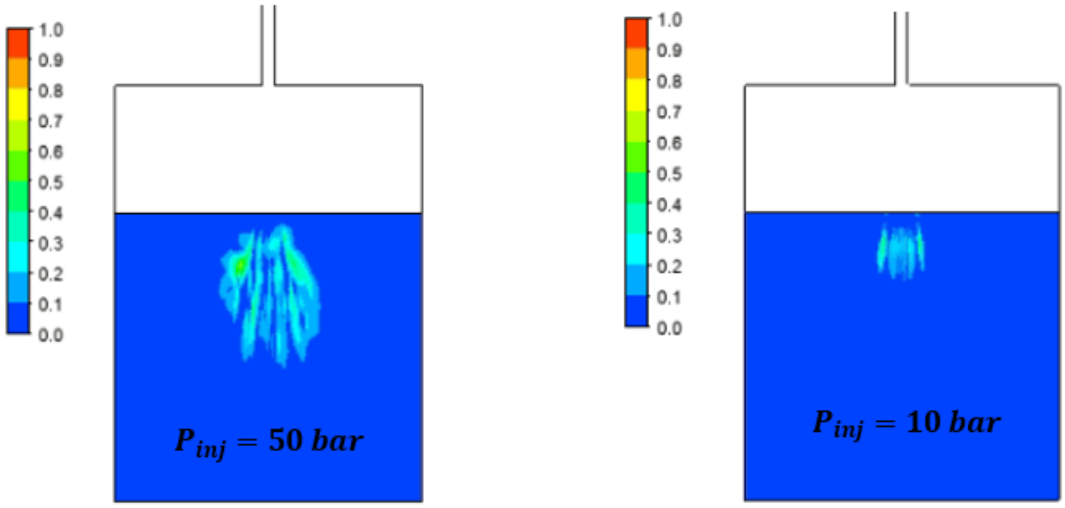

Figure 5.6: Volume fraction of liquid nitrogen below the water surface 6 ms into the injection

The evaporation coefficient of liquid nitrogen was varied and compared using Cases 3-5. The rate of evaporation was found to influence the shape and the core length of the propagating jet as shown in Figure 5.7. Initially, all three profiles are similar as the liquid phase emerges from into the vessel and the jet remained intact at this stage as it is continued to be shielded by the vapour layer. On impact with the water surface, the jet spreads forming an arrow type shape as it propagates through the water in Case 3 and 4. The vapour layer at higher values of C_v is a lot thicker due to the increased rate of evaporation upon contact with the water surface. Accordingly, the leading edge at a lower mass transfer exhibited a higher liquid phase volume

fraction at the leading edge of the jet. The boiling intensity is especially seen on the trailing edge, which gradually narrows down and for Case 5, disappears altogether. Consequently, the volume fraction of the liquid phase in Case 5 was recorded at zero below the water surface. At considerably higher evaporation coefficients, it is possible that the entire jet could evaporate above the water surface that would be detrimental to the overall heat transfer resulting in further pressurisation.

Increase in the C_v value was also observed to reduce the width and length of the core. The length of the jet that remains intact would have more flow resistance in the water and drive further turbulence and mixing below the surface.

At relatively higher velocities, the head of the jet experiences far greater momentum and drag forces resulting in a larger velocity and thermal boundary layer. The thickness may be up to a tenth of a micrometre, thus resulting in a very high heat transfer coefficient. As the jet propagates through the water, there is a slight decrease in mass transfer however, it occurs on a larger surface area due to the jet breakup that occurs during mixing.

Cv = 0.1

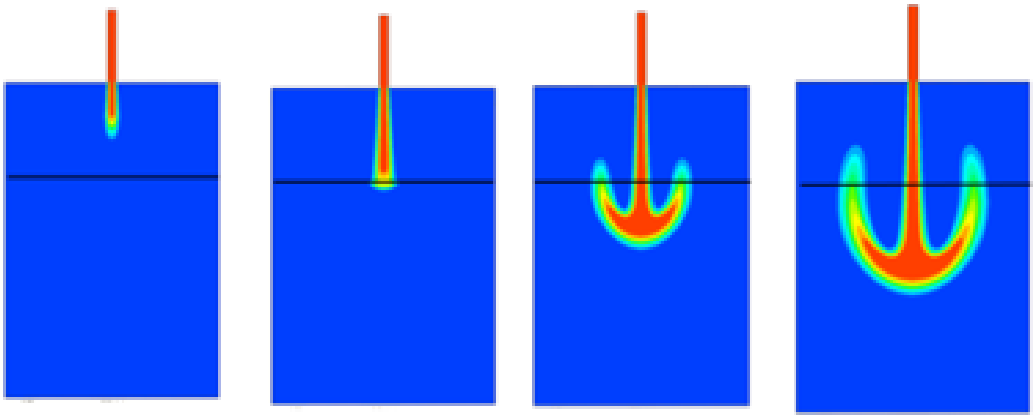

Cv = 2

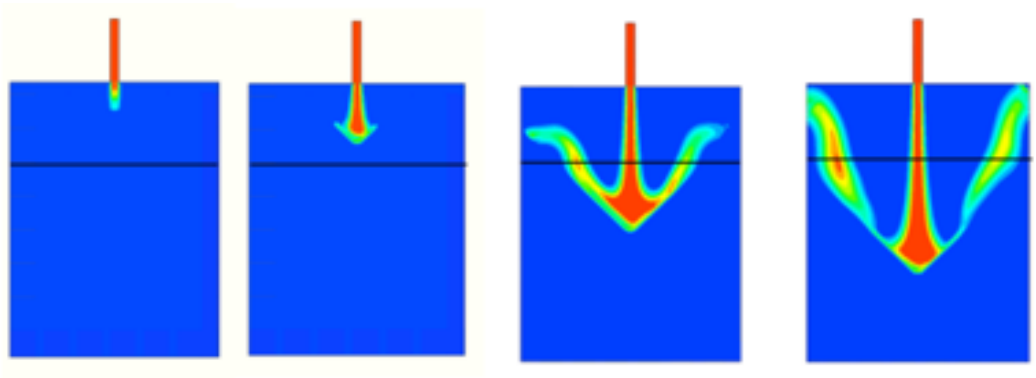

Cv = 10

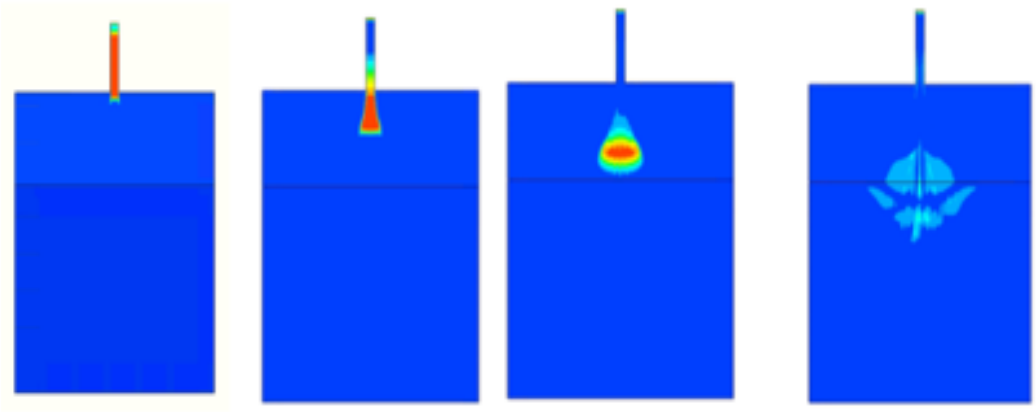

Figure 5.7 : Jet propagation of liquid nitrogen injection into an infinite pool of water for C_v = 0.1 (top), C_v= 2 (middle) and C_v = 10 (bottom). Liquid phase is shown in red and gradually disappears due to the phase change.

The mass transfer rate from the liquid to the vapour phase in the domain for Cases 2, 4 and 7 at different injection pressures is shown in Figure 5.8. There is a significant fluctuation of the mass transfer at the higher values of C_v in the entire domain, which could be attributed to the continuous breakup of the jet's core as it propagates

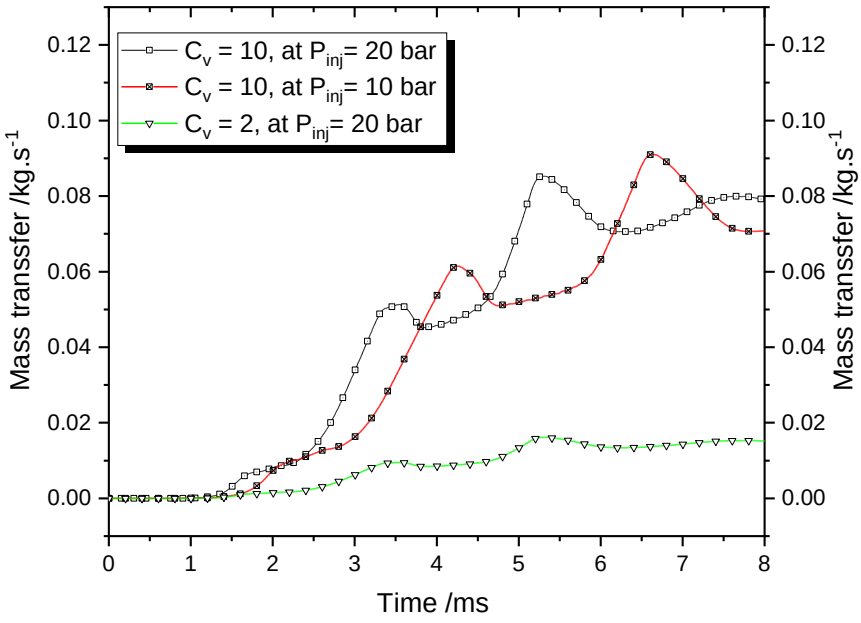

Figure 5.8: Effect of evaporation coefficient on the rate on the domain mass transfer using a comparison of Cases 2,4 and 7.

through the air and water. This is more evident in Case 7 at higher pressure with a rapid increase in the mass transfer, which is due to the propagation velocity.

At a higher evaporation rate, the mass transfer fluctuates significantly during the duration of the injection. During its propagation, the jet will intermittently come into direct contact with the water which could explain the consecutive peaks in mass transfer. Additionally, the increase in flow turbulence to facilitate the mixing of the two fluids could be the reason why this phenomenon is more pronounced at higher injection pressure.

5.1.3.3 Injection into warm and cold air

Cases 1 and 9 were compared in Figure 5.9. At 0.5 ms into the injection, there is an obvious effect on the jet propagation rate. In ambient air, the maximum velocity of the liquid core was at 40 m/s less than that in cold air.

Consequently, the impact velocity at the water surface is significantly reduced due to the increased evaporation rate above the water surface. The heat transfer in this region is therefore not only attributed to the enhanced turbulence generated by the interaction of the jet with its stagnant surroundings but also, due to the large temperature difference between the two fluids. With a reduced penetration velocity and consequently penetration depth, the intensity of the heat transfer below the water surface will be significantly reduced.

5.1.3.4 Case 10: Heat transfer with water

The incompressible jet was found to break up immediately upon its impact with the water surface as shown in Figure 5.10. The core is exposed to the water, which causes it to boil and evaporate. The contour images of the velocity show a significant

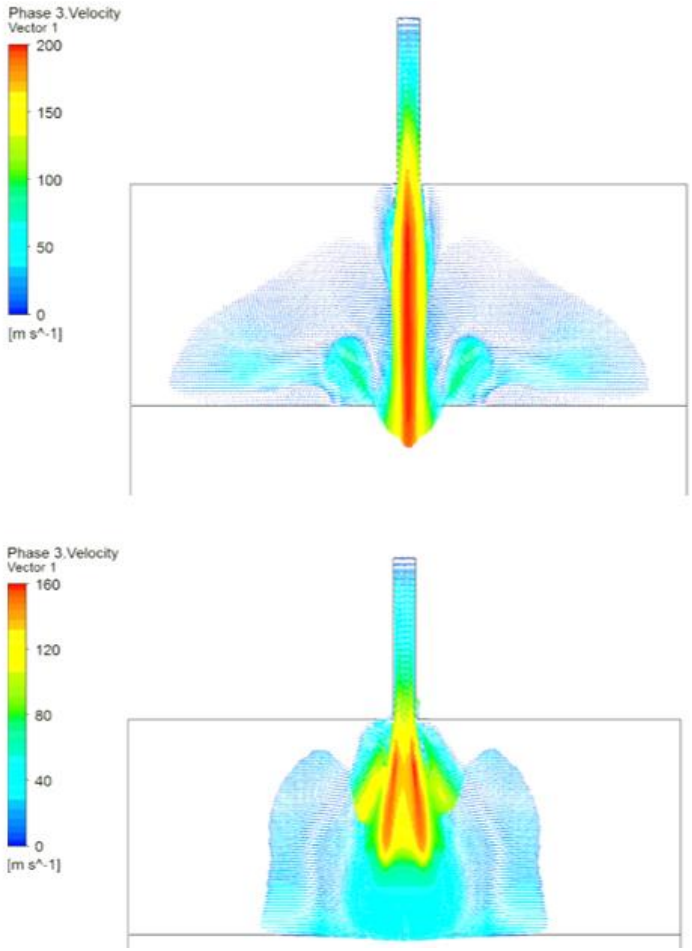

Figure 5.9: Velocity vectors of liquid nitrogen injected into cold air (Case 8; top) and ambient air (Case 7; bottom) at 0.5 ms

reduction in the core length, which is observed to disintegrate at the leading edge of the jet (Figure 5.11). The mass transfer in the wake of the jet is a clear indication of the formation of smaller ligaments that would eventually break off from the core. However, details of this phenomenon can only be captured using a 3D simulation.

Figure 5.11 shows the jet to split the surface of the water causing to rise on the sides of the vessel. Consequently, this will cause the water to collapse on the jet and enhance the turbulent mixing in the vessel. As a result of the heat transfer with the water the volume fraction of the liquid in the core is significantly reduced 0.4 ms into

the injection. These results confirm the hypothesis of the augmentation of the jet breakup due to both aerodynamic and thermal effects.

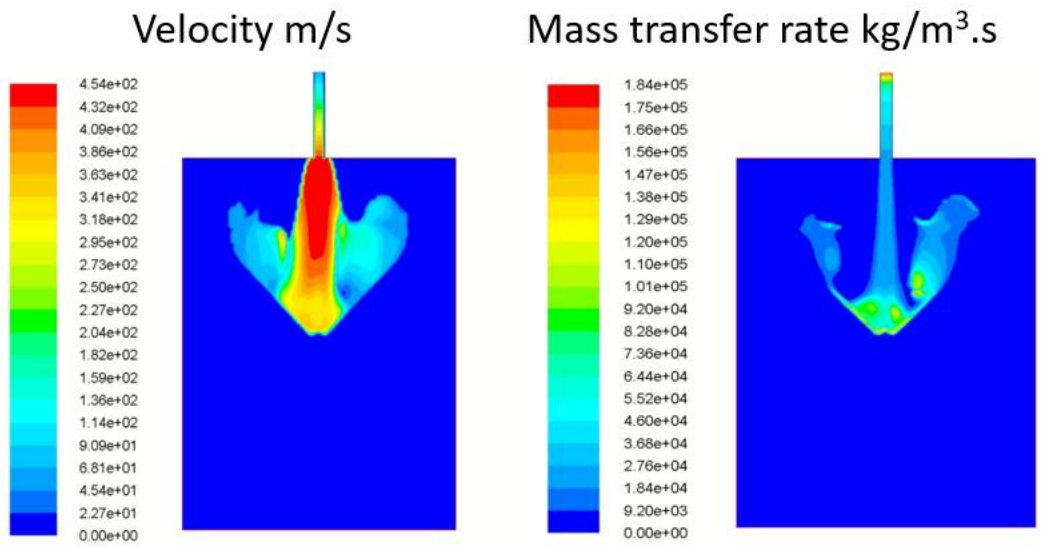

Figure 5.11: Contour map of the velocity and mass transfer rate for Case 10

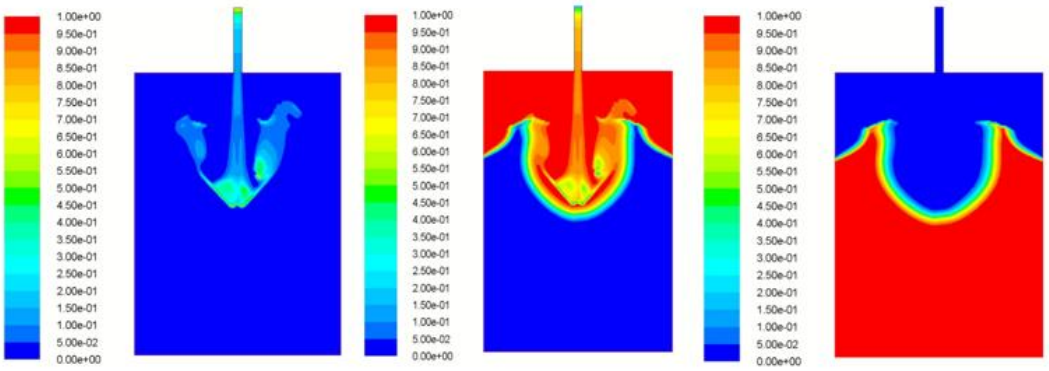

Figure 5.10: Volume fraction of the liquid, gas and water phases (from left to right) at 0.4 ms into the injection.

For further comparison, the mass transfer rate obtained from the simulations for Cases 2,7 and 10 is shown in Figure 5.12 along the centre line. Liquid nitrogen undergoes film boiling in the nozzle based on the temperature gradient. Heat is

transferred by forced convection associated with high heat transfer coefficients and high pressure drops in small pipe diameters(95). The flow can be described as transitory, where flow at uniform temperature develops under the influence of the walls at ambient temperature. The mass transfer rate at the inlet starts off really high

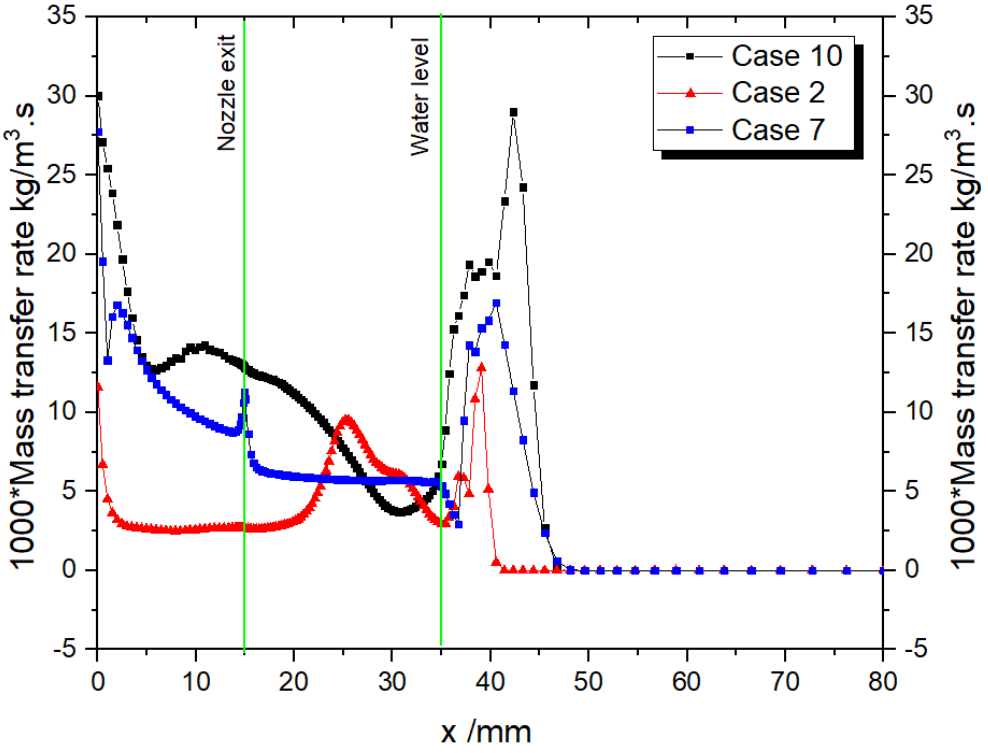

Figure 5.12: Mass transfer along the centre line from the nozzle to the outlet pressure for Cases 1,2 and 8 at 10 ms.

as a result of flashing. This is due to exposure to the warm nitrogen gas at ambient pressure inside the vessel. A temperature gradient develops across the diameter of the nozzle, resulting in the formation of a vapour film along the nozzle walls. This limit contact with the liquid nitrogen causing the steep decline of the mass transfer rate. The liquid flows in a continuous phase in the centre of the nozzle known as inverted-annular flow. The velocity increases gradually along the length of the nozzle and at high liquid velocity/pressure, the turbulence and agitation of the gas-liquid

interface would result in the much more chaotic flow regime known as churn flow(96).

The mass transfer in the region above the water surface is an indication of the length of the liquid core. Increase in the mass transfer along the axis suggests the onset of phase change and evidence of disruption to the continuity of the core. In contrast, Case 10 and 7 demonstrate a slightly extended core that ~ 12 mm below the water surface. This is because of the increased injection velocity and mass flux at the inlet resulting in higher propagation speed. As this is simply a snapshot in time, the decreasing mass transfer prior to the water surface is further evidence that the jet begins to narrow at the trailing edge, due to the intensity of the boiling process. When injected into cold air, thermal effects on the jet break up are eliminated resulting in an increased core length that goes beyond the water surface.

It should be noted that below the water surface, the mass transfer rate increases significantly for all three cases. The injection at 50 bar shows a greater mass transfer because of the greater impact velocity and increased turbulent mixing, which facilitates further break-up of the liquid core.

The distribution of the liquid volume fraction along the centre line 0.5 ms into the injection at various injections pressures is shown in Figure 5.13. The volume fraction at the nozzle is reduced significantly at a higher pressure as a result of the high mass transfer rate indicated in Figure 5.12. The volume fraction continues to decay gradually and the termination of the core at 10 – 20 mm below the water level confirming an increased penetration depth at higher injection pressure. As the jet

losses a significant amount of velocity as it travels, these results support the notion that the water level should be kept near the valve to ensure high impact velocity.

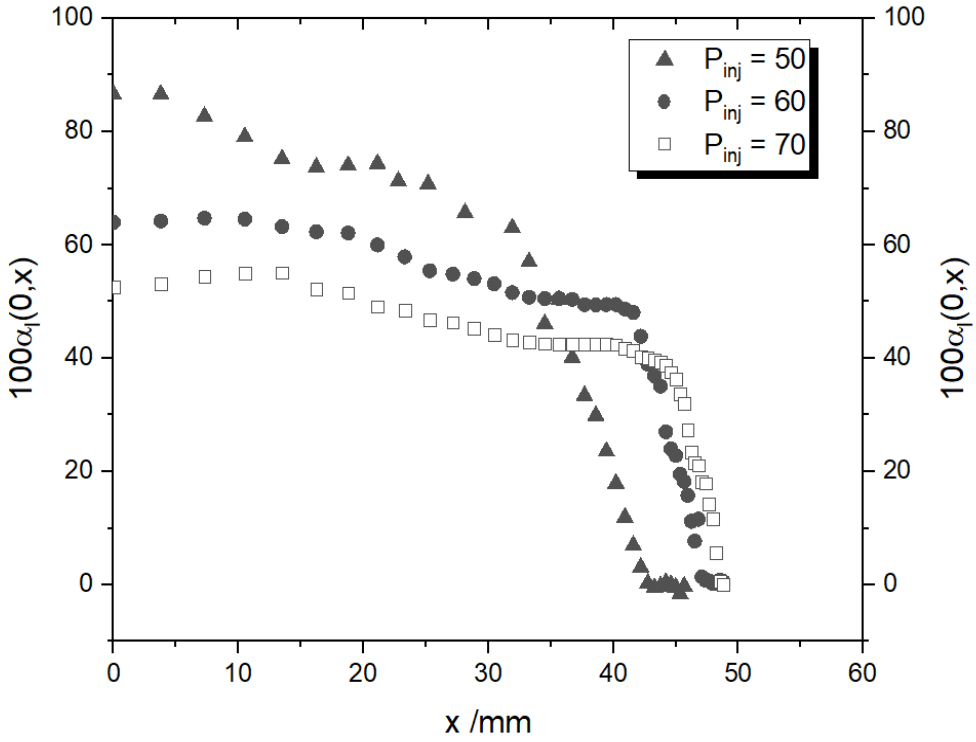

Figure 5.13: Volume fraction of liquid phase along centre line for Case 10 at 50, 60 and 70 bar.

5.1.4 Effects of injection parameters on the jet dynamics and propagation

The lack of compressibility within these simulations makes it difficult to compare the pressure data obtained from the experimental results in Chapter 4. However, these results were used for a more qualitative analysis of the effect of jet velocity, wall heat transfers and mass transfer rate on the propagation and mixing of the liquid nitrogen jet.

The forces required for the break-up of the liquid jet are surface tension, viscous and inertia forces. Surface tension is an important factor here. The primary break-up of the jet in its initial stages is associated with the shear instability at the gas/liquid interface that results in the stripping off of the liquid jet by high shear forces. Past

experiments(22) observed the jet to undergo Kelvin Helmholtz instabilities close to the nozzle, where the surface tension acts as a destabilising force. The individual liquid pieces chipped off the liquid core may still undergo further break up if the forces exerted by the turbulence can exceed those (surface tension and viscosity) that bind it together.

At high Reynolds number, as a result of the increase injection pressure, the large velocity gradient makes for turbulent surroundings and dynamic pressure which would facilitate further break up(61). The process of air entrainment creates turbulence within the air and breaks up the continuous liquid into droplets forming a wedged shaped core whose velocity is equal to that at the nozzle exit. The destabilisation of the liquid jet is a result of the aerodynamic forces acting on it. These are enhanced by the extent of turbulence in the nozzle flow and the relative velocity between the jet and its surroundings.

Drag forces increase with the acceleration/velocity of the jet, which is a consequence of the change of the streamline shape that causes a change to the pressure field (97). The work of the drag force if dissipated into heat in the trailing edge, which would also cause it to narrow in this region.

The inability to measure the instantaneous pressure across the valve means that the model was based on assumptions of the pressure profile during the injection, which further complicates comparison with experimental work. Additionally, in real injections, a larger volume fraction of the gas phase is expected due to the decrease

in density as the temperature increases. However, to the contrary, in practice, the density increases as a result of the pressure rise in the vessel.

Despite the increase in injection velocity/pressure, the model is not able to capture the entrainment of water into liquid nitrogen jet which facilitates further contact between the two liquids. This was due to the contrasting of the 2D geometry and the failure to model compressibility inside the vessel(1).

5.2 Droplet evaporation in water

An important element of this study was the evaporation from a liquid-liquid interface formed between the nitrogen and HEF. The heat needed to initiate this process is far greater than those on a solid surface.

Modelling of the process has been a very challenging task, especially due to the speed and limited visibility of the process. Nonetheless, CFD simulations can be utilised to provide a better understanding of the fluid behaviour inside the vapour cloud during the injection, especially the thermal and hydrodynamic interaction at the interface between the 3 phases. The VOF model with interfacial tracking is used to simulate the film boiling of the droplet when immersed in water.

5.2.1 Simulation approach

5.2.1.1 Mesh and geometry

The droplet was assumed to be spherical and that the surrounding fluid remains at a constant temperature throughout the process. A 2D computational domain of 85 x 85 mm was used to represent the vessel. Grid and time dependency tests showed that a structural grid of 28900 elements (Figure 5.14) with a time step of 5 x10^{-4} produced sufficient results.

5.2.1.2 Boundary and initial conditions

A pressure boundary condition was applied to the top of the cube to allow for the escape of the gas phase generated. The water phase was patched to a height of the 60 mm with the droplet located at the centre. The thermal physical properties and

saturation temperature of liquid nitrogen were kept constant and referenced at atmospheric pressure.

Interfacial tracking using the VOF model was used to trace the vapour-liquid interface, where the vapour was considered the primary phase. The geometric reconstruction algorithm was used to better estimate the bubble interface(90). The model represents the interface between two fluids using a piecewise -linear approach. It does so by assuming a linear slope at the interface within each cell and uses the linear shape for calculation of the advection of fluid through the cell faces.

The continuum surface force (CSF) model was used to account for the surface tension forces that stabilise the interfacial instability. First order implicit discretisation was used for the transient time calculations and VOF equation. The Quick logarithm was used for the momentum and energy discretisation and the Presto to interpolate the pressure values (84).

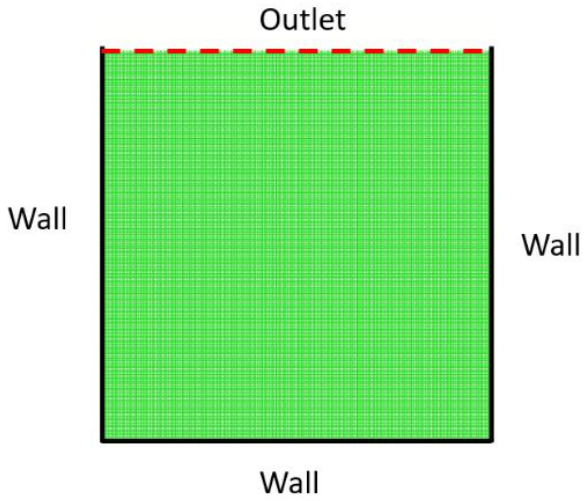

Figure 5.14: Structured mesh, boundary conditions and geometry of droplet simulation

5.2.1.3 Mesh dependency

Similar to Section 5.1.2.4, a grid dependency was also conducted here using the mass transfer rate at 5 ms, which is calculated from Equation 5.16. The mass transfer rate is calculated Results showed to be independent of mesh size and time step at a grid size of 28900, which was used in all the simulations in the case investigated.

Table 5.4: Mesh dependency

Elements	Maximum mass transfer ($kg/m^3.s$)
7225	102135
11236	102167
28900	102230
35721	102235
45369	102235

5.2.2 Results

The study was categorised into three main cases as shown in Table 5.5 to investigate the evaporation time of the droplet. The cases were selected based on injection conditions and previous studies on jet break up and droplet distribution.

Table 5.5 Cases simulated for the boiling of a liquid nitrogen droplet

Case A

Simulation	C_v	T_w (K)	d_p (mm)
A	10	200	6

Case B

Simulation	C_v	T_w (K)	d_p (mm)
1	0.5	300	1
2	5	300	1
3	10	300	1
4	100	300	1
5	3 x10^4	300	1

Case C

Simulation	C_v	T_w (K)	d_p (mm)
1	100	100	6
2	100	200	6
3	100	300	6

5.2.2.1 Case A: Droplet break-up

The contour map shown in Figure 5.15 shows the evolution of the bubble generated from the film boiling/evaporation, which was immediately encased by a thin ring of the vapour indicating an equal evaporation rate on the surface of the droplet. During the evaporation, the phase change occurs at the vapour-liquid interface. Contrary to the evaporation or film boiling on a heated surface, the formed bubble did not exhibit any detachment or frequency of generation. At the start, the vapour film thickness is

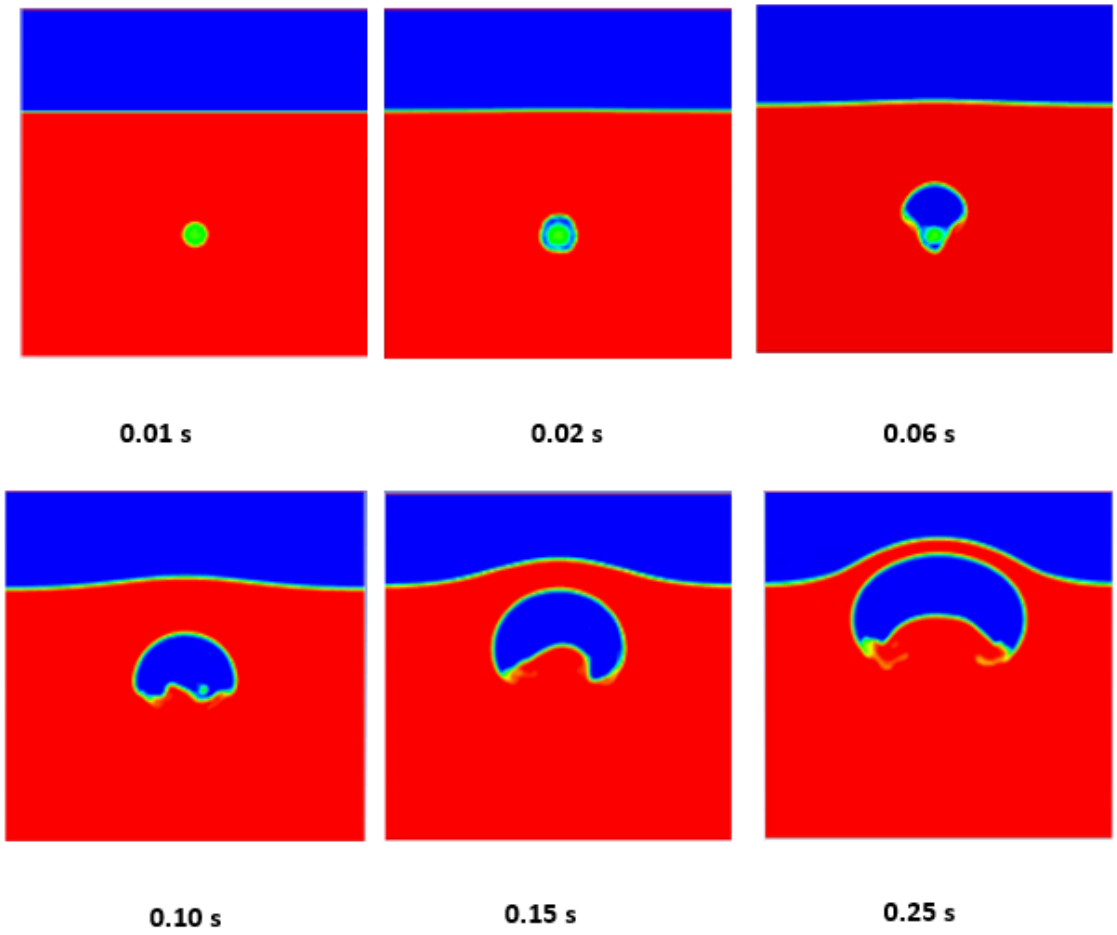

Figure 5.15: Evolution of vapour cloud during the evaporation of liquid nitrogen droplet in water. The liquid phase is shown in green, gaseous nitrogen in blue and water in red.

at its highest value, which would correspond to a lower heat flux but a larger mass transfer rate. At 0.22 s, the liquid volume fraction had reduced by 65% where the mass transfer rate had dropped significantly.

The growth of the bubble was sustained by the continuous formation of vapour as the droplet diminishes. At this large temperature difference, the vapour film remained undisrupted which is characteristic of film boiling above the Leidenfrost point (~ 180 K) (98).

There is evidence of droplet break up at this stage indicated by the high mass transfer rate within the bubble due to traces of unevaporated liquid nitrogen droplets (Figure 5.16). The mass transfer increases with the spread of the liquid droplet, which is attributed to the increased surface area. Buoyancy forces take over and drive what is left of the liquid nitrogen droplet upwards towards the surface. As the bubble rises it tries to attain a spherical shape due to the effects of surface tension(99).

Distortion of the larger vapour cloud to allow for contact between the water and the remaining liquid nitrogen droplets is postulated to be a direct result of the turbulence created by the jet impact with the water surface and the walls of the vessel. For longer injections, the injected jet would also facilitate the break-up of the cloud to release unexpanded liquid nitrogen from its confinement.

The 6 mm droplet evaporated in 3.1 s, which is ~8 times less than that presented in an experimental study by Chandra et al. (46) investigating the evaporation of liquid nitrogen droplets on a glass and copper surfaces. Assuming a spherical shape, these results show that a 0.09 g droplet of liquid nitrogen evaporated in 3.1 s.

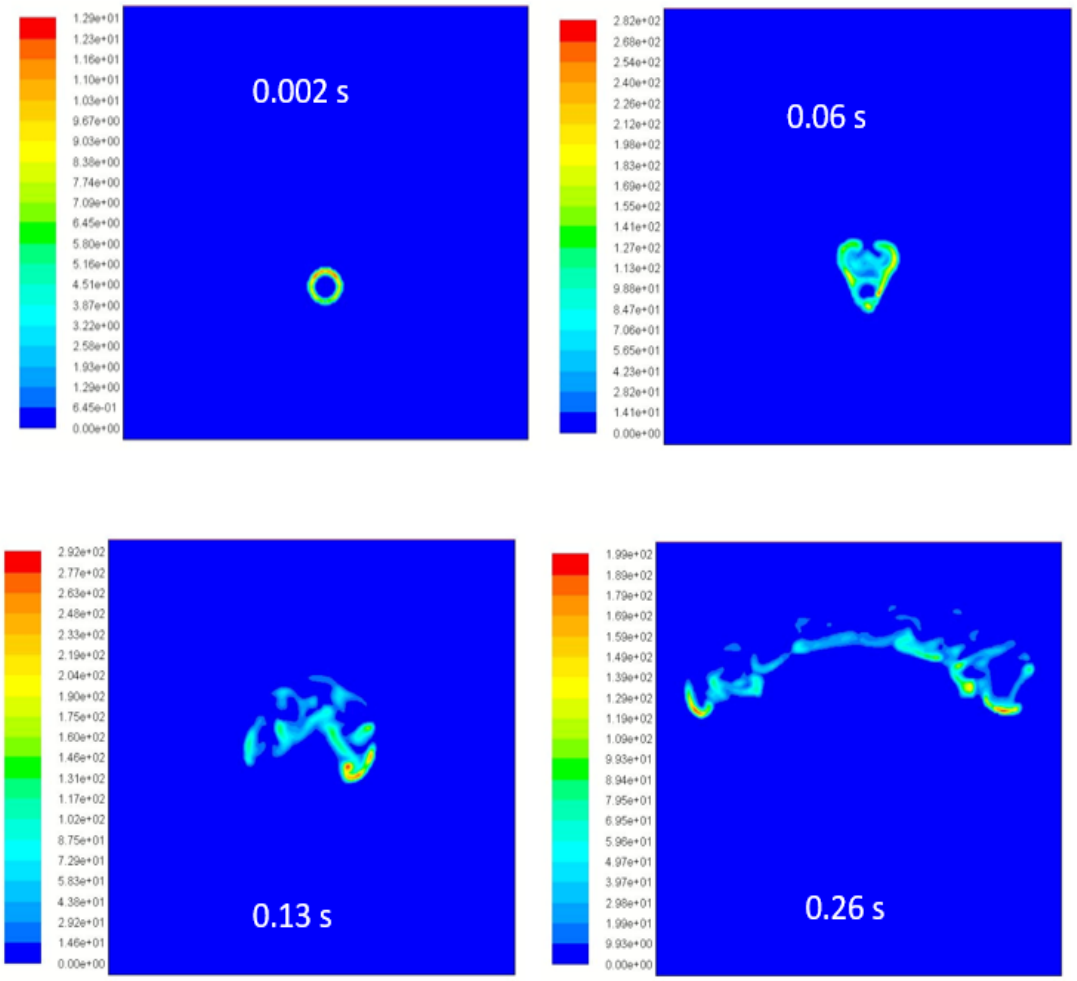

Figure 5.16: Contour map of liquid-gas mass transfer rate for case A1

In comparison to the experiments, assuming that the phase change is completed by the point of attaining the peak pressure in the vessel, the evaporation time in this simulation is overestimated by a factor of 10^2. However, it is important to note that the VOF model treats the energy and temperature as mass averaged variables and that the accuracy of the temperature at the interface is limited especially in cases with a large temperature difference between the phases.

5.2.2.2 Case B: Effect of evaporation coefficient

Figure 5.17 shows a comparison of the mass transfer rate as a function of time simulations in Case B. The mass transfer to the droplet in Case B3 increases drastically to a maximum of $\sim$ 35 kg/m.s before it rapidly declines as the droplet grows smaller. At a lower value of $C_v = 0.5$ for Case B1, the mass transfer increases gradually and plateaus off at value 1/6 that of Case B3.

In order to reflect the evaporation time scales observed in the experiments in Chapter 5, much higher evaporation coefficients are needed. Case B4 at $C_v = 100$ showed better results with the evaporation of the droplet within 40 ms as shown in Figure 5.18. Heat is conduct to the liquid through the vapour film and due to its thermal resistance, the mass transfer drops by 1/3 of its initial value in the first

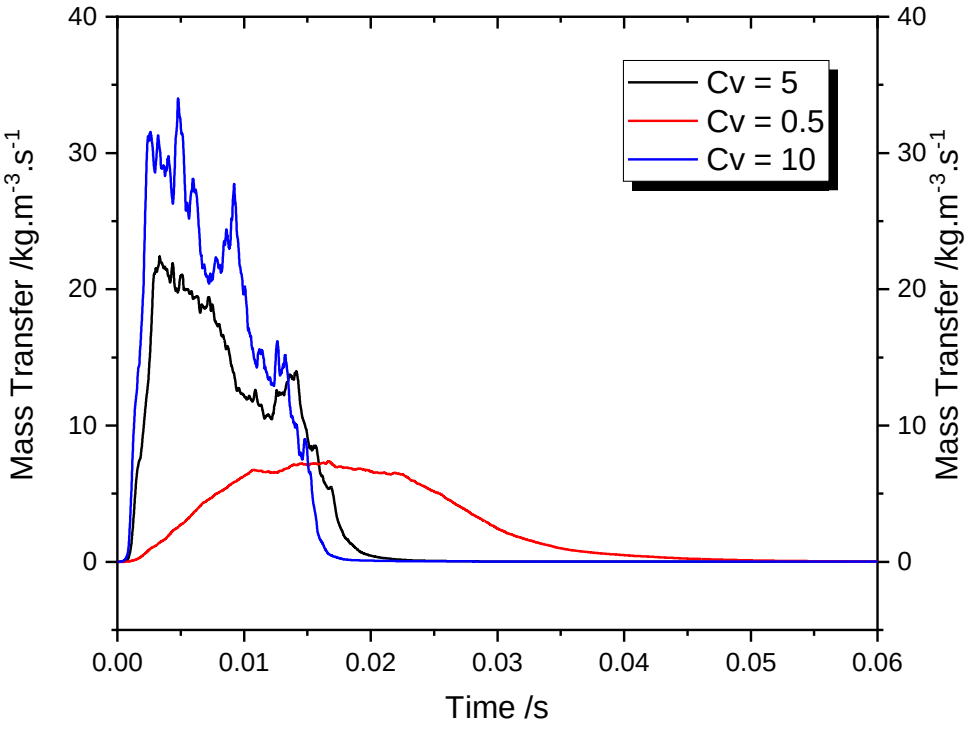

Figure 5.17: Effect of evaporation coefficient on the mass transfer and evaporation time

millisecond. This could also be attributed to the reduced volume fraction of the droplet.

Clarke (1) estimated the correct accommodation coefficient was greater than 3 x10^8 for a droplet of 1 mm in water at room temperature. However, Case B4 at C_v = 3 x 10^4 corresponded to mass transfer rates of up to 1.95 x 10^6 kg/m^3s and an evaporation time of 1.25 ms, which under predicted the experimental evaporations times based on the pressure rise in the vessel for a droplet of this size and density.

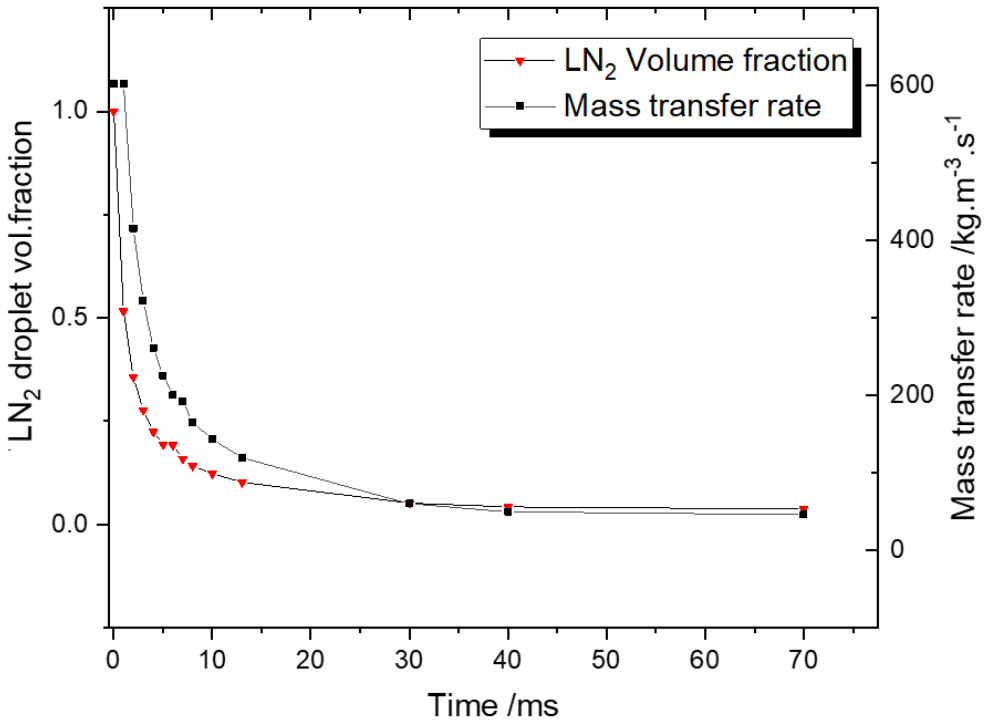

Figure 5.18: Liquid volume fraction and mass transfer as a function of time for Case B4 at Cv = 100

5.2.2.3 Case C: Effect of HEF temperature

Variation of the water temperature showed a decrease in the evaporation time with the increase in ΔT at the interface. Figure 5.19 shows that the initial maximum mass transfer rate at the start was 10^2 greater in magnitude with the water at ambient temperature (Case C3). This is attributed to the increase in heat flux with the increase

in the superheat provide by the water. As the droplet continues to evaporate, ΔT decreases and the boiling processes reach the Leidenfrost point corresponding to the lowest heat flux. The evaporation time in Case C3 was recorded at 1.47 s which was almost double that of Case C1 due to the reduced temperature difference.

The simulations were limited by the aggregative treatment of the energy equation and making it impossible to define the heat transfer between the phases. Another drawback was that the evaporation model does not account for the sensible heating of the droplet. By definition of the evaporation coefficient, the mass transfer only occurs once the saturation temperature is exceeded.

The Eulerian method was used as an alternative but suffered from stability and poor convergence due to the complex water-gas-liquid interface.

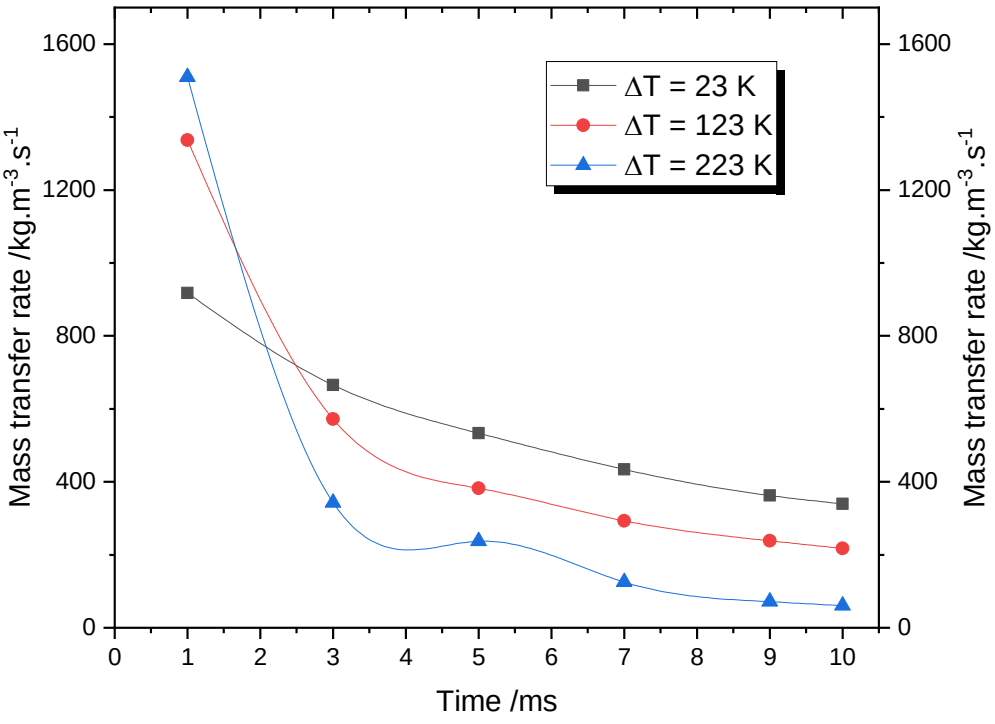

Figure 5.19: Effect of HEF temperature on droplet mass transfer rate

5.2.2.4 Discussion: Droplet evaporation

Without the effects of turbulence in the water, the results presented here will vary that in the vessel because the evaporation of the droplet is greatly influenced by the fluid flow around it. Earlier work(50) on the flow around submerged bodies such as bubbles and drops was based on assumptions of an ideal, incompressible and non-viscous continues phase. The results were impractical but were still predicted the velocity and pressure distributions for a small range of flow.

Navier-Stokes equations have been solved for large Reynolds numbers where the steep velocity and thermal gradient in the boundary layer. Outside the boundary layer, the velocity gradient is less of an issue and viscous effects are often ignored. Redfield and Houghton(100) studied the mass transfer and drag coefficient at different Reynolds number for single droplets of carbon dioxide and concluded that at Reynolds numbers between 100-5000, the shape of the bubbles changed from a spheroidal to a mushroom cap shape. The simulations conducted here revealed bubble velocities of up to 0.8 m/s which could be the reason for the bubble shape in Figure 5.15. Terjesen et al.(101) demonstrated that the effects of higher heat coefficients that were attributed to hydrodynamic disturbances in the unstable boundary layer.

Unfortunately, the model does not capture the rapid distortion and oscillation of the droplet in connection with the Leidenfrost phenomenon. The oscillation of the droplet causes degradation of the boundary layer and thus increases heat transfer. Previous studies(52) have shown that surfactants increase the heat transfer rate by

increasing the oscillation of the droplet but also lower it by repressing circulation and interfacial rippling.

The amount of distortion to a droplet/bubble was found to be dependent on droplet diameter, velocity and the physical properties of the system(100, 102) however, there is no method to predict the exact nature and distortion of a droplet of a given size.

5.3 Chapter summary

The CFD simulation work presented here aims to further our understanding of the jet flow dynamics of the injected nitrogen jet and the droplet boiling and evaporation within the vapour cloud in relation to the two-stage boiling process addressed in Chapter 4.

Both studies experienced several limitations to the proposed models related to convergence and stability, which necessitated the simplification of not only the geometry but material properties as well. This restricted the inclusion of pressure dependent fluid properties which is crucial to the pressurisation in the injection process.

Even so, the qualitative data showed that instability at the interface was invigorated by the enhanced shear flow generated by the sufficiency increased velocity gradient at higher injection pressures. The primary break-up of the injected jet is thought to be responsible for the formation of smaller liquid nitrogen droplets that are uncased in a vapour cloud. The vapour was maintained by the high temperature difference

and the release of unexpanded droplets highly dependent on the turbulence created by the jet propagation through the water and its impact with the walls of the vessel.

Simulations of droplet evaporation highlighted the effect of the HEF temperature and evaporation coefficient on the mass transfer and evaporation time. However, despite its interfacial tracking technique, the VOF model was not able to fully capture the interfacial heat transfer between phases due to the collective treatment of the energy at the interface. The model was found to underpredict the evaporation time of the droplet, which was attributed treatment of the energy equation of the VOF model. This is also due to the fact that the pressurisation in the vessel was also a result of mass transfer into a fixed volume.

CHAPTER 6

6 Conclusions and Future Work

Overall this work has shown improved engine performance using the direct liquid injection for the cryogenic engine due to the enhanced direct heat transfer allowing for a close to isothermal expansion of the liquid nitrogen. The extent of these results provides a method of performance prediction for a given combination of injection parameters allowing for engineers to develop engine output curves and power values based on the optimization of performance and fuel consumption.

6.1 Injection rig and performance

In addition to the valve system, the liquid nitrogen injection studied in this work is novel in the approach to simultaneous pre-pressurisation and sub-cooling. Experimental studies in the past had struggled with controlling the temperature of the nitrogen which limited the range of injection pressure.

A lot of work went into designing a static injection rig to provide an effective means of control of the injection process with synchronised measurement of the transient flow rate, pressure and temperature in order to quantify the influence of injection parameters such as pressure, temperature and valve timings on the engine performance.

- The rig allowed for the controlled injection of liquid nitrogen in three thermodynamic states; liquid, gas and supercritical states. Liquid injections showed better pressurisation results in comparison to both gas and supercritical critical injection s of nitrogen.

- A passive sub-cooling system allowed for the sub-cooling of liquid nitrogen pre-injection resulting in injection temperatures of up to 87°K. The use of a passive system means that no pumping work is needed which would otherwise reduce overall engine efficiencies.
- Precise valve movement and exact measurement of injection duration were achieved with the uses of the complex electromagnetic hydraulic actuator used to control the opening and closing of the valve during the injection.
- The use of a poppet valve is found to increase the contact area thus increasing the direct contact heat transfer between the liquids.

Mass flow rate experiments performed ranged from injection pressures of 5 to 96 bar, injection temperatures as low as 87°K and valve frequency of up to 20 Hz indicative of engine speed of up to 1200 rpm. The effect of valve actuation and timing and the thermodynamic state of the cryogen pre-injection were investigated.

Due to its ability to perform high pressure injections at cryogenic temperatures, flow experiments from the injection rig confirmed an approximately linear increase in injected mass for liquid injections with increasing pressure and increased subcooling. Results ranged from 0.19 -1.57 kg of liquid nitrogen providing a total heat energy of 38 – 312 KJ to convert to engine power inside the cylinder.

- Injection tests showed peak pressures of up to 91 bar, developing an engine output of 3.3 KJ due to the increased flow rate due to the increased pressure and reduced temperature.

- The highest-pressure time derivative of ~5200 bar/s (a $\frac{1}{10}$ th of the magnitude of that recorded in an ICE engine operating at 1000 rpm) was recorded at an injection at 76 bar and 103 °K for an injection duration of 10 ms. This value was 10 times greater than previous work. Experiments also confirmed an approximately linear correlation with the injection pressure and pressurisation rate.
- High pressure liquid injections showed better pressurisation with a specific work output of up to 0.6 MJ/kg with a maximum heat transfer rates of 8 kW resulting in a better isothermal expansion in the cylinder.
- This equates to an energy conversion of about 83 % of the available energy. This value of 66% greater than that found in literature. The enhanced isothermal efficiency and extraction of the available energy was attributed to the added passive subcooling pre-injection, the modified nitrogen delivery system and the considerable increase in the injection pressure made possible by the designed injection system.
- Short injections at high engine speeds were found to limit the amount of nitrogen admitted to the vessel and ultimately reduce engine power during the cycle. On the other hand, long injections not only bore down the engine speed, but the prolonged opening of the valve would compromise the pressurise in the vessel.

6.2 Recommended improvements

The most obvious improvement is the further increase of the injection pressure to increase engine efficiency. However, it is likely to increase the work input for subcooling pre-injection and call for the use of a cryogenic pump. The injection pressure can be increased infinitely so long as the work output continues to exceed the pumping work in, to maintain sufficient engine efficiencies.

Additionally, full pressurisation through a cryogenic pump would alleviate the heat leak prior to injection providing more control over the injection pressure.

Further experimental work is needed to determine the heat transfer rates involved at injection pressures of up to 400 bar. With the possibility of atomisation, it cannot be assumed to resemble the isothermal expansion at lower pressure. Therefore, the benefits of the increased injection pressure will not only depend on the heat transfer inside the engine cylinder but on the thermal and dynamic flow effects of the liquid across the injection valve.

At lower speeds, a large pressure ratio and consequently a large piston stroke is attainable with an intake/injection duration of 10 -15 ms. At higher speeds and shorter injection durations, multiple cylinders would need to be in operation to meet the speed and power necessary.

Engine efficiency can also be increased by the addition of multiple expansion stages within the engine cycle. Further expansion due to reheating in a secondary expansion stage has been known to increase cryogenic engine efficiency by 35- 45 % with the addition of waste heat from the primary engine (103).

Enhancement of heat transfer inside the engine lies with the increase in the mixing and turbulence between the two fluids in contact. This can be done using multiple valve injections or the simultaneous injection of HEF and the nitrogen into the vessel. However, both strategies would require further modification and improvements to the valve timings.

A thermodynamic systems analysis showed that although the majority of the heat transfer occurs in the water, a significant portion of the heat transfer may occur between the nitrogen and the engine apparatus. Improvement to the heat transfer could be achieved with the addition of internal fins or implementation of engineered materials. Additional channels of HEF flows could be incorporated in the piston head and the vessel walls.

6.3 Injection rig improvements

The current injector consists of a hardened stainless-steel poppet valve fitted with a UHMWPE valve seat to withstand any abrasion and fatigue at impact during the closing of the valve. The valve seat also serves as the seal to confine the pressure inside the vessel.

Flow tests did not indicate any signs of leakage of nitrogen into the vessel once the valve was closed. However, pressure tests showed a pressure leak as the vessel pressure approached the peak value.

In an attempted to correct this, the hydraulic oil pressure of the EHVA was increased in order to apply a greater force on closing the valve. However, during the pulsed injections, the increased force compromised the thread on the poppet valve stem.

The lack of a seal meant that all pulsed pressurisation tests were inaccurate and unsuitable. A more extensive study to determine the life cycle of the UHMWPE under cryogenic temperatures under such high impact forces is needed so that the seat can be changed prior to failure.

Additionally, modifications to the shape of the poppet valve can be considered. Designs can be refuted using CFD modelling of the flow patterns to determine its suitability and effectiveness for this application.

Modifications to the injector and the feed lines to realise a more adiabatic pressurisation is practically impossible. Higher injection pressures would increase flow instability and reduce the effectiveness of the injector. However, further insulation can be implemented to improve control of the heat leak in the feed system.

Additionally, a cryogenic pump would allow for more accurate measurement of the flow rates across the valve. A cryogenic flow meter would serve as an alternative however may give wrong readings in case of two-phase flow. An ideal device would be able to constantly gauge the density of the flowing medium.

Visibility of the injection processes would validate assumptions of the flow profile of the liquid nitrogen from the poppet valve. Modifications could be made to the cylinder walls to allow for visualisation but still able to without compromising the pressurisation process.

Listed below are other issues encountered during testing and how they were resolved.

- Overheating of the hydraulic oil: After numerous injections, the oil temperature would exceed 60 $°C$ and invalidate the accuracy of the valve movement. Expelled nitrogen from the sub-cooling system can be redirected to cool down the oil tank.
- Injector valve seal: The leak was detected where the injector locks into the top clamp plates of the vessel. PTFE tape was used here.
- Poppet valve lift adjustment: Due to wear of the thread on the valve stem, the valve often became loose during pulsed injections. The thread was re-machined however; a more permanent solution would require the entire replacement of the valve.
- Formation of ice on the poppet valve- often caused by the splashback of water during high pressure injections. This would limit flow through the valve which meant that experiments had to put off until the system returned to home temperature.
- Leak at the Kistler transducer- located in the piston head, a leak was detected and resolved with PTFE tape.
- Immovable piston head- occurred due to abrasion damage of the sides of the piston head making it difficult to make intricate adjustments during experiments. To move the piston, the entire vessel had to be taken apart.

6.4 Computational modelling

In this body of work, an attempt was made to gain a better understanding of the mixing of liquid nitrogen in the engine cylinder and droplet evaporation in water

using CFD. Simulations were simplified to a very basic level because the software is currently unable to deal with multiphase phase flow at such high temperature and velocity gradients.

Simulations of the phase change and heat transfer were simplified to achieve convergence. Multiphase heat transfer was limited to the nitrogen phases based on the known Ranz and Marshal correlation for liquid droplets in still air. Therefore, the simulations did not model the exchange of heat due to direct contact with water.

Furthermore, as the gas properties are restricted to a constant density, which would not reflect the initial reduction in gas density as the temperature rises, followed by the reverse effect when the vessel pressure increases due to the pressure build up. The pressurisation in the engine cylinder is a very vital aspect of the engine but not achievable in the simulations.

Aware of its limitations, the use of CFD in the development of the technology lies in the design and optimisation of the two-phase flow across the poppet valve. A closer investigation is needed for the thermal and dynamic effects due to the pressure drop at the intake. This can be done with the RPI model that would account for the convective, quenching and evaporative heat flux from the walls to the liquid. However, the description of the interfaces also greatly relies on empirical correlations which need to be verified from test results. It should also be noted that precise representation of the injector geometry and the full modelling of the unsteady flow would come at a greater computational cost.

The cryogenic engine has the capability of an auxiliary/secondary power source in a hybrid engine. This research shows direct high-pressure liquid nitrogen injections provide the necessary velocity and mass flow rates to increase the heat transfer to make this more viable. The static injection rig used to conduct the injections was able to elucidate the benefits and limitations of the liquid injections with emphasis on the parameters that would control engine speed and power. Further work is needed to cover the concept more extensively, but there is still potential for this novel zero-emission engine suitable for the use in freight vehicles that require a cooling compartment.

6.5 Future work

The results presented here provide an insight into to the direct injection of liquid nitrogen for a cryogenic engine. The scope of these results and conclusions are however limited by the range of the operating conditions due to the design of the injection rig. Discussed below is how future work could be conducted to facilitate in the development of the engine technology.

Based on its novelty, there was a lot to be learned from the shortcomings (discussed in Section 6.3) of the injector prototype and the complexity of the delivery and pre-pressurisation system. The rig was often out of commission due the wear and damage of its mechanical parts or by the pressure leak in the vessel. As repairs were made quite often, experiments could not proceed until the valve was returned to its original configuration. A look at alternative injector designs is suggested and this was a big deterrent to the continuity of experiments.

One of the major limitations of previous work was the lack of control of the injection duration and valve movement. While the implementation of the EHVA has alleviated this issue, the next step is to apply the valve to actual engine testing to determine the precise timing of the valve opening and closing.

REFERENCES

1. Clarke, H. *A Novel Cryogenic Energy System for Zero Emission Vehicles*. thesis, Queen Mary, University of London, 2011.
2. Rydberg, K.-E. Hydraulic servo systems. *TMHP51 Fluid and Mechanical Engineering Systems. Linköping University.* 2008.
3. Knowlen, C. et al. *Quasi-isothermal expansion engines for liquid nitrogen automotive propulsion.* SAE Technical Paper, 1997.
4. Williams, J. et al. Frost-free cryogenic heat exchangers for automotive propulsion. *AIAA paper.* 1997, (97-3168).
5. Ltd, D.E.C. *Improved cryogenic engine system* 10/2016.
6. WHO. *Ambient (outdoor) air quality and health.* [Online]. 2016. [Accessed 15/05/2018]. Available from: http://www.who.int/en/news-room/fact-sheets/detail/ambient-(outdoor)-air-quality-and-health.
7. Transport, D.o. *New regulations to double the use of sustainable renewable fuels by 2020.* [Online]. 2018. [Accessed]. Available from: https://www.gov.uk/government/news/new-regulations-to-double-the-use-of-sustainable-renewable-fuels-by-2020.
8. Wang, W. et al. Reducing CO2 footprint through synergies in carbon free energy vectors and low carbon fuels. *Energy.* 2016, **112**, pp.976-983.
9. Gill, S. et al. Assessing the effects of partially decarbonising a diesel engine by co-fuelling with dissociated ammonia. *International journal of hydrogen energy.* 2012, **37**(7), pp.6074-6083.
10. Collantes, G.O. The California zero-emission vehicle mandate: A study of the policy process, 1990-2004. 2006.
11. Adder, J. Assessment of future vehicle transportation options and their impact on the electric grid. *US Nat. Energy Technol. Lab., Morgantown, WV, USA, Tech. Rep. DOE/NETL-2010/1466.* 2011.
12. Debnath, S.C. Environmental regulations become restriction or a cause for innovation–a case study of Toyota Prius and Nissan Leaf. *Procedia-Social and Behavioral Sciences.* 2015, **195**, pp.324-333.
13. Bossel, U. Thermodynamic analysis of compressed air vehicle propulsion. *Journal of KONES Internal Combustion Engines.* 2005, **12**(3-4), pp.51-62.
14. CLCF. *Liquid Air on the Highway.* Centre for Low Carbon Futures, 2014.
15. Hertzberg, A. et al. Frost-free cryogenic heat exchangers for automotive propulsion. In: *33rd Joint Propulsion Conference and Exhibit*, p.3168.
16. Knowlen, C. et al. Cryogenic automotive propulsion. *Proceedings of AIAA 19th IECEC, CA, US AIAA, Paper.* 1994, (944224).

17. Ordonez, C. et al. Cryogenic heat engines for powering zero emission vehicles. In: *Proceedings of 2001 ASME international mechanical engineering congress and exposition, US, IMECE*, 2001, pp.67-75.

18. Dahlsveen, J. et al. Jet mixing of cryogen and water. In: *TSFP DIGITAL LIBRARY ONLINE*: Begel House Inc., 2001.

19. Dinh, T.N. et al. Experimental and analytical studies of melt jet-coolant interactions: a synthesis. *Nuclear Engineering and Design.* 1999, **189**(1-3), pp.299-327.

20. Burgess, D.S. et al. *Hazards of LNG spillage in marine transportation.* BUREAU OF MINES PITTSBURGH PA SAFETY RESEARCH CENTER, 1970.

21. Wen, D.S. et al. Liquid nitrogen injection into water: Pressure build-up and heat transfer. *Cryogenics.* 2006, **46**(10), pp.740-748.

22. Clarke, H. et al. Experimental study of jet structure and pressurisation upon liquid nitrogen injection into water. *International Journal of Multiphase Flow.* 2010, **36**(11-12), pp.940-949.

23. Mazza P, H.R. *Wind-to-wheel energy assessment.* [Online]. 2009. [Accessed]. Available from: <http://www.efcf.com/reports/E18.pdf>.

24. CLCF. *Liquid Air Technologies: A guide to the potnetial.* [Online]. 2013. [Accessed 01/10]. Available from: http://www.lowcarbonfutures.org/reports/research-reports.

25. Research, T.M. *Transport Refrigeration Units Market – Global Industry Analysis, Size, Share, Growth, Trends, and Forecast, 2018 – 2026.* [Online]. 2018. [Accessed 22/05]. Available from: https://www.transparencymarketresearch.com/transport-refrigeration-units-market.html.

26. Dearman, C. *The Dearman Engine.* [Online]. 2015. [Accessed 05/05/2015]. Available from: http://www.dearmanengine.com/#!the-dearman-engine/c1g0q.

27. Heywood, J.B. Internal combustion engine fundamentals. 1988.

28. Stone, R. *Introduction to internal combustion engines.* Springer, 1999.

29. Knowlen, C. et al. *High efficiency energy conversion systems for liquid nitrogen automobiles.* SAE Technical Paper, 1998.

30. Ordonez, C.A. Liquid nitrogen fueled, closed Brayton cycle cryogenic heat engine. *Energy Conversion and Management.* 2000, **41**(4), pp.331-341.

31. Chen, H. et al. Air fuelled zero emission road transportation: A comparative study. *Applied Energy.* 2011, **88**(1), pp.337-342.

32. Liu, L. et al. Thermal cycle design of liquid nitrogen engine. *JOURNAL-ZHEJIANG UNIVERSITY ENGINEERING SCIENCE.* 2006, **40**(11), p.1989.

33. Ameel, B. et al. Thermodynamic analysis of energy storage with a liquid air Rankine cycle. *Applied Thermal Engineering.* 2013, **52**(1), pp.130-140.

34. Latter, A.L. et al. *Engine system using liquid air and combustible fuel*. 1982.

35. Dooley, J. and Hammond, R. CRYOGENIC NITROGEN AUTOMOTIVE ENGINE. *Mechanical Engineering.* 1984, **106**(10).

36. Manning, L. and Schneider, R. *Nitrogen vapor engine*. 1974.

37. West, C.W. et al. *Vehicle utilizing cryogenic fuel*. 1978.

38. Plummer, M. et al. Cryogenic heat engine experiment. In: *Advances in cryogenic engineering*. Springer, 1998, pp.1245-1252.

39. Dearman, P.T. *Engines driven by liquified or compressed gas*. 2006.

40. Ayres, M. et al. *Cryogenic engine system*. Google Patents, 2014.

41. Dearman, P. *Injection Apparatus for Cryogenic Engines*. Google Patents, 2006.

42. Khabeev, N.S. Simulation of vapour explosions. *Applied Energy.* 1999, **64**(1-4), pp.317-321.

43. Duckworth, R. et al. Analysis of liquid cryogen-water experiments with the MELCOR code. *Proceedings of 14th topical meeting on the technology of fusion energy, Park City, UT, US.* 2000.

44. Archakositt, U. et al. Effect of volumetric ratio and injection pressure on water-liquid nitrogen interaction. *Journal of Nuclear Science and Technology.* 2004, **41**(4), pp.432-439.

45. Drake, E.M. et al. TRANSIENT BOILING OF LIQUEFIED CRYOGENS ON A WATER SURFACE .1. NITROGEN, METHANE AND ETHANE. *International Journal of Heat and Mass Transfer.* 1975, **18**(12), pp.1361-1368.

46. Hu, H.-P. The surface tension effects in boiling heat transfer of cryogenic LN2 on an ellipsoid. *Nuclear Engineering and Design.* 2010, **240**(1), pp.139-145.

47. Drake, E.M. et al. Transient boiling of liquefied cryogens on a water surface: I. Nitrogen, Methane and Ethane. *International Journal of Heat and Mass Transfer.* 1975, **18**(12), pp.1361-1368.

48. Okuyama, K. and Iida, Y. TRANSIENT BOILING HEAT-TRANSFER CHARACTERISTICS OF NITROGEN (BUBBLE BEHAVIOR AND HEAT-TRANSFER RATE AT STEPWISE HEAT-GENERATION). *International Journal of Heat and Mass Transfer.* 1990, **33**(10), pp.2065-2071.

49. Prakash, C.B. and Pinder, K. Direct contact heat transfer between two immiscible liquids during vaporisation. *The Canadian Journal of Chemical Engineering.* 1967, **45**(4), pp.210-214.

50. Prakash, C.B. *Direct contact heat transfer between two immiscible liquids during vaporization*. thesis, University of British Columbia, 1966.

51. Sideman, S. and Taitel, Y. Direct-contact heat transfer with change of phase: evaporation of drops in an immiscible liquid medium. *International Journal of Heat and Mass Transfer.* 1964, **7**(11), pp.1273-1289.

52. Klipstein, D.H. *Heat transfer to a vaporizing immiscible drop*. thesis, Massachusetts Institute of Technology, 1963.

53. Battya, P. et al. Parametric studies on direct contact evaporation of a drop in an immiscible liquid. *International journal of heat and mass transfer.* 1984, **27**(2), pp.263-272.

54. Luketa-Hanlin, A. A review of large-scale LNG spills: experiments and modeling. *Journal of hazardous materials.* 2006, **132**(2), pp.119-140.

55. Bøe, R. Pool boiling of hydrocarbon mixtures on water. *International Journal of Heat and Mass Transfer.* 1998, **41**(8-9), pp.1003-1011.

56. Chandra, S. and Aziz, S.D. LEIDENFROST EVAPORATION OF LIQUID-NITROGEN DROPLETS. *Journal of Heat Transfer-Transactions of the Asme.* 1994, **116**(4), pp.999-1006.

57. Wen, D. et al. PHASE CHANGE HEAT TRANSFER OF LIQUID NITROGEN INJECTION INSIDE A HEAT TRANSFER FLUID. In: *International Heat Transfer Conference 13*: Begel House Inc., 2006.

58. Martin, H. Heat and mass transfer between impinging gas jets and solid surfaces. In: *Advances in heat transfer*. Elsevier, 1977, pp.1-60.

59. Eroglu, H. et al. Coaxial atomizer liquid intact lengths. *Physics of Fluids A: Fluid Dynamics.* 1991, **3**(2), pp.303-308.

60. Marmottant, P. and Villermaux, E. On spray formation. *Journal of Fluid Mechanics.* 2004, **498**, pp.73-111.

61. Lasheras, J. et al. Break-up and atomization of a round water jet by a high-speed annular air jet. *Journal of Fluid Mechanics.* 1998, **357**, pp.351-379.

62. Lasheras, J.C. and Hopfinger, E. Liquid jet instability and atomization in a coaxial gas stream. *Annual review of fluid mechanics.* 2000, **32**(1), pp.275-308.

63. *Release 16.2, theory guide, in. 2017. 2014*.

64. Sadus, R.J. *Molecular simulation of fluids: theory, algorithms, and object-orientation.* Elsevier, 2002.

65. Mackie, A.D. et al. Dissipative particle dynamics with energy conservation: Modelling of heat flow. *Physical Chemistry Chemical Physics.* 1999, **1**(9), pp.2039-2049.

66. Avalos, J.B. and Mackie, A. Dynamic and transport properties of dissipative particle dynamics with energy conservation. *The Journal of chemical physics.* 1999, **111**(11), pp.5267-5276.

67. Nourgaliev, R. et al. The multiphase Eulerian-Lagrangian transport (MELT-3D) approach for modeling of multiphase mixing in fragmentation processes. *Progress in Nuclear Energy.* 2003, **42**(2), pp.123-157.

68. Fletcher, D. The particle size distribution of solidified melt debris from molten fuel-coolant interaction experiments. *Nuclear Engineering and Design.* 1988, **105**(3), pp.313-319.

69. Gabillard, M. et al. Rapid phase transition of liquefied gas. In: *European applied research conference, Trondheim, Norway*, 1996.

70. Hosangadi, A. et al. Three-dimensional hybrid RANS/LES simulations of a supercritical liquid nitrogen jet. In: *44th AIAA/ASME/SAE/ASEE Joint Propulsion Conference & Exhibit*, 2008, p.5227.

71. Park, T.S. LES and RANS simulations of cryogenic liquid nitrogen jets. *The Journal of Supercritical Fluids.* 2012, **72**, pp.232-247.

72. Zong, N. Modeling and simulation of cryogenic fluid injection and mixing dynamics under supercritical conditions. 2004.

73. Potoff, J.J. and Siepmann, J.I. Vapor–liquid equilibria of mixtures containing alkanes, carbon dioxide, and nitrogen. *Aiche Journal.* 2001, **47**(7), pp.1676-1682.

74. Lefebvre, P. *Poppet valve for internal combustion engine*. Google Patents, 1991.

75. Wang, A. et al. Lubrication and wear of ultra-high molecular weight polyethylene in total joint replacements. *Tribology International.* 1998, **31**(1-3), pp.17-33.

76. Hambir, S. and Jog, J.P. Sintering of ultra high molecular weight polyethylene. *Bulletin of Materials Science.* 2000, **23**(3), pp.221-226.

77. Liu, H.T. et al. Tribological properties of ultra-high molecular weight polyethylene at ultra-low temperature. *Cryogenics.* 2013, **58**, pp.1-4.

78. *Moog, n.d. Type 30 nozzle-flapper flow control servovalves.* [Online]. [Accessed 19/09/2017]. Available from: http://www.mylesgroupcompanies.com/moog_pdfs/Moog%2030%20Series%20Catalog.pdf.

79. Zhou, Z.-j. et al. Analysis on shock wave speed of water hammer of lifting pipes for deep-sea mining. *China Ocean Engineering.* 2013, **27**(2), pp.205-214.

80. Span, R. et al. A reference equation of state for the thermodynamic properties of nitrogen for temperatures from 63.151 to 1000 K and pressures to 2200 MPa. *Journal of Physical and Chemical Reference Data.* 2000, **29**(6), pp.1361-1433.

81. Wood, G. et al. *Air flow through intake valves.* SAE Technical Paper, 1942.

82. Stanitz, J.D. et al. *Steady-and intermittent-flow coefficients of poppet intake valves.* AIRCRAFT ENGINE RESEARCH LAB CLEVELAND OH, 1946.

83. McDougall, I. The boiling of cryogenic fluids—A survey. *Cryogenics.* 1971, **11**(4), pp.260-267.

84. Ahammad, M. et al. A CFD based model to predict film boiling heat transfer of cryogenic liquids. *Journal of Loss Prevention in the Process Industries.* 2016, **44**, pp.247-254.

85. Zvirin, Y. et al. Boiling on free-falling spheres: drag and heat transfer coefficients. *Experimental Heat Transfer.* 1990, **3**(3), pp.185-214.

86. Yagov, V. et al. Film boiling of subcooled liquids. Part I: Leidenfrost phenomenon and experimental results for subcooled water. *International Journal of Heat and Mass Transfer.* 2016, **100**, pp.908-917.

87. Fyke, A. et al. Recovery of thermomechanical exergy from cryofuels. *International Journal of Hydrogen Energy.* 1997, **22**(4), pp.435-440.

88. Ripper, W. *Steam-engine theory and practice.* Longmans, Green & Co., 1912.

89. Tomiyama, A. et al. Transverse migration of single bubbles in simple shear flows. *Chemical Engineering Science.* 2002, **57**(11), pp.1849-1858.

90. *Ansys Fluent : User Guide* 2018.

91. Young, R. and Pfender, E. Nusselt number correlations for heat transfer to small spheres in thermal plasma flows. *Plasma Chemistry and Plasma Processing.* 1987, **7**(2), pp.211-229.

92. Koffman, L. et al. Theory of evaporation and condensation. *The Physics of fluids.* 1984, **27**(4), pp.876-880.

93. [Online]. [Accessed]. Available from: https://webbook.nist.gov/chemistry/.

94. Guha, A. et al. Numerical simulation of high-speed turbulent water jets in air. *Journal of Hydraulic Research.* 2010, **48**(1), pp.119-124.

95. Chen, X. et al. Two-phase flow boiling frictional pressure drop of liquid nitrogen in horizontal circular mini-tubes: Experimental investigation and comparison with correlations. *Cryogenics.* 2017, **83**, pp.85-94.

96. P, K.Z. et al. Flow boiling of liquid nitrogen in narrow annular channels. *Progress in Superconductivity and Cryogenics.* 2008, **10**(4), pp.1-5.

97. Wallis, G.B. The terminal speed of single drops or bubbles in an infinite medium. *International Journal of Multiphase Flow.* 1974, **1**(4), pp.491-511.

98. Barron, R.F. and Nellis, G.F. *Cryogenic Heat Transfer: Cryogenic Heat Transfer.* CRC press, 2016.

99. Ahammad, M. et al. Application of Computational Fluid Dynamics in Simulating Film Boiling of Cryogens. *Industrial & Engineering Chemistry Research.* 2016, **55**(27), pp.7548-7557.

100. Redfield, J. and Houghton, G. Mass transfer and drag coefficients for single bubbles at Reynolds numbers of 0· 02–5000. *Chemical Engineering Science.* 1965, **20**(2), pp.131-139.

101. Thorsen, G. and Terjesen, S. On the mechanism of mass transfer in liquid-liquid extraction. *Chemical Engineering Science.* 1962, **17**(3), pp.137-148.

102. Garner, F. and Hammerton, D. Circulation inside gas bubbles. *Chemical Engineering Science.* 1954, **3**(1), pp.1-11.

103. Zhang, N. et al. *A novel Brayton cycle with the integration of liquid hydrogen cryogenic exergy utilization.* 2005.

APPENDIX

Table **A**: Pressurisation tests

Test	P_{inj} (bar)	T_{inj} (K)	Phase	ρ_{inj} kg/m^3	Injection period (s)	Lift (mm)	Mass (g)	P_{eak} (bar)	dp/dt (bar/s)
1	20	101.2	liquid	690	0.700	1.222	4.406	21.9	668
2	20	120.9	vapor	78	0.400	1.212	3.964	19.9	630
3	20	86.4	liquid	771	2.500	1.212	6.748	37.0	167
4	30	293.0	vapor	35	2.500	1.212	0.504	4.6	147
5	30	293.0	vapor	35	2.500	1.222	0.571	8.7	172
6	30	103.6	liquid	685	2.500	1.212	1.617	7.0	349
7	30	125.9	vapor	142	4.000	1.211	1.146	4.9	309
8	30	120.0	liquid	541	4.000	1.212	1.992	8.6	468
9	30	93.7	liquid	735	0.010	1.212	5.672	33.0	124
10	38	128.6	supercritical	318	0.700	1.212	3.451	30.9	851
11	30	87.1	liquid	770	0.010	1.211	0.210	90.3	2882
12	38	121.0	liquid	551	0.010	1.222	3.702	15.9	984
13	38	123.9	liquid	509	0.010	1.222	3.247	14.0	921
14	30	125.4	vapor	147	0.010	1.212	5.919	25.5	1710
15	30	108.7	liquid	652	0.010	1.222	0.138	59.5	2527
16	40	114.9	liquid	618	0.010	1.222	0.118	51.0	2345
17	40	112.4	liquid	633	0.010	1.213	0.150	64.5	3248
18	40	127.0	supercritical	458	0.020	1.212	2.854	49.1	2806
19	40	123.1	liquid	528	0.020	1.212	2.430	41.9	2510
20	20	108.2	liquid	644	0.020	1.212	1.405	24.2	1138
21	20	95.1	liquid	725	0.010	1.212	1.409	24.3	593
22	20	113.3	liquid	598	0.020	1.213	0.335	22.0	72
23	48	121.3	liquid	567	0.003	1.222	0.118	22.2	1428
24	49	123.1	liquid	551	0.003	1.222	0.146	25.1	1719
25	49	125.4	liquid	525	0.003	1.222	0.127	21.9	1516
26	49	108.0	liquid	667	1.000	1.222	0.332	57.2	3629
27	49	145.1	supercritical	186	0.007	0.765	0.230	39.6	88
28	24	122.0	vapor	103	0.010	1.190	0.140	24.1	1488
29	60	135.5	supercritical	422	0.010	1.199	0.036	15.3	948
30	28	127.6	vapor	115	0.010	1.199	0.101	17.3	1147
31	28	125.4	vapor	124	0.010	1.222	0.161	27.7	1742
32	22	123.0	vapor	74	0.010	1.212	0.111	19.2	1192
33	20	118.8	vapor	82	0.010	1.212	0.086	14.8	935
34	15	111.9	vapor	62	0.010	1.212	0.035	15.0	784
35	14	110.1	vapor	58	0.010	1.212	0.078	13.4	815
36	10	111.4	vapor	36	0.010	1.212	0.078	13.5	844
37	10	113.4	vapor	35	0.010	1.212	0.082	14.2	853
38	10	108.6	vapor	38	0.010	1.212	0.105	18.1	828
39	15	108.2	liquid	637	0.010	1.212	0.025	21.8	891
40	15	104.9	liquid	662	0.010	1.212	0.052	22.3	960
41	20	113.0	liquid	610	0.010	1.212	0.129	22.2	1079

Test	P_{inj} (bar)	T_{inj} (K)	Phase	ρ_{inj} kg/m^3	Injection period (s)	Lift (mm)	Mass (g)	P_{eak} (bar)	dp/dt (bar/s)
42	35	117.2	liquid	584	0.010	1.212	0.063	26.9	1519
43	35	128.3	supercritical	193	0.010	1.212	0.116	20.0	1280
44	35	118.5	liquid	571	0.010	1.212	0.059	25.4	1505
45	50	138.3	supercritical	259	0.010	1.212	0.178	30.7	1993
46	48	121.2	liquid	568	0.010	1.212	0.304	52.4	3294
47	48	116.6	liquid	607	0.010	1.212	0.324	55.8	3447
48	50	114.5	liquid	623	0.010	1.212	0.323	55.7	3454
49	60	119.1	liquid	602	0.010	1.212	0.146	62.9	3921
50	50	116.9	liquid	607	0.010	1.212	0.316	54.4	3300
51	45	113.0	liquid	631	0.010	1.212	0.259	44.6	2401
52	60	109.0	liquid	668	0.010	1.212	0.147	64.6	3940
53	60	110.1	liquid	662	0.010	1.212	0.145	62.9	3893
54	60	109.0	liquid	668	0.010	1.212	0.143	61.7	3842
55	75	109.5	liquid	674	0.010	1.212	0.403	69.3	4413
56	70	117.0	liquid	631	0.010	1.212	0.415	71.5	4575
57	72	117.1	liquid	627	0.010	1.212	0.427	73.6	4684
58	74	116.8	liquid	631	0.010	1.212	0.415	71.5	4557
59	74	104.8	liquid	699	0.010	1.212	0.421	73.5	4609
60	74	103.6	liquid	705	0.010	1.212	0.416	71.7	4509
61	76	103.2	liquid	708	0.010	1.212	0.464	79.9	5156
62	75	115.3	liquid	641	0.010	1.212	0.448	77.1	4595
63	25	114.9	liquid	590	0.010	1.212	0.089	38.4	1851
64	15	119.4	vapor	53	0.010	1.212	0.038	16.2	1005
65	27	117.9	liquid	561	0.010	1.212	0.222	38.2	1993
66	10	104.5	vapor	41	0.010	1.212	0.091	15.6	679
67	10	98.8	liquid	698	0.010	1.212	0.104	17.9	627
68	10	106.3	vapor	39	0.010	1.212	0.097	17.9	452
69	20	111.7	liquid	612	0.010	1.212	0.132	22.7	1236
70	20	113.8	liquid	593	0.010	1.212	0.117	23.2	135
71	15	119.1	vapor	54	3.600	1.222	0.089	15.3	806
72	45	116.2	liquid	607	0.010	1.212	0.277	47.7	3098
73	45	121.4	liquid	560	0.010	1.212	0.131	47.9	968
74	10	107.9	vapour	38	0.010	1.212	0.037	6.4	314
75	9	106.1	vapor	35	0.010	1.212	0.076	13.1	596
76	10	98.1	liquid	702	0.010	1.212	0.075	12.9	631
77	10	97.9	liquid	704	0.010	1.212	0.076	13.0	581
78	10	99.8	liquid	692	0.010	1.212	0.085	14.6	626
79	10	100.3	liquid	689	0.010	1.212	0.083	14.4	626
80	11	106.5	liquid	647	0.010	1.212	0.085	14.6	718
81	10	139.1	vapor	26	0.010	1.212	0.032	5.5	358
82	8	148.0	vapor	19	0.010	1.212	0.033	5.7	371
83	10	150.5	vapor	24	0.010	1.212	0.037	6.4	429
84	20	158.5	vapor	47	0.010	1.212	0.027	11.8	791
85	25	90.1	liquid	753	0.010	1.212	0.111	47.9	1797
86	28	120.4	liquid	528	0.010	1.212	0.151	25.9	1680

Test	P_{inj} (bar)	T_{inj} (K)	Phase	ρ_{inj} kg/m^3	Injection period (s)	Lift (mm)	Mass (g)	P_{eak} (bar)	dp/dt (bar/s)
87	28	101.5	liquid	693	0.010	1.212	0.198	34.2	1948
88	28	109.1	liquid	643	0.010	1.212	0.172	29.7	1784
89	28	122.8	vapor	143	0.010	1.212	0.149	25.7	1662
90	25	118.2	liquid	525	0.010	1.212	0.036	15.6	1021
91	79	117.2	liquid	632	0.010	1.212	0.371	63.9	4192
92	80	113.2	liquid	657	0.010	1.212	0.417	71.8	4687
93	60	118.2	liquid	609	0.010	1.212	0.237	40.9	2541
94	45	116.6	liquid	603	0.010	1.212	0.236	40.6	2574
95	44	111.6	liquid	646	0.010	1.212	0.267	46.0	2902
96	46	115.9	liquid	610	0.010	1.212	0.178	30.7	2034
97	46	118.1	liquid	592	0.010	1.212	0.257	44.3	2813
98	45	124.6	liquid	523	0.010	1.212	0.263	45.2	2858
99	45	112.9	liquid	631	0.010	1.212	0.254	43.7	2769
100	45	116.5	liquid	604	0.010	1.212	0.255	44.0	2746
101	40	136.6	vapor	169	0.010	1.212	0.194	33.4	2046
102	55	128.4	supercritical	505	0.010	1.212	0.088	38.1	2493
103	55	136.5	supercritical	361	0.010	1.212	0.146	25.1	1668
104	55	137.1	supercritical	348	0.010	1.212	0.140	24.1	1613
105	55	113.3	liquid	638	0.010	1.212	0.272	46.9	2984
106	55	130.0	supercritical	484	0.010	1.212	0.153	26.3	1741
107	55	105.1	liquid	687	0.010	1.212	0.282	48.6	3082
108	55	93.6	liquid	747	0.010	1.212	0.276	47.5	3060
109	55	123.0	liquid	562	0.010	1.212	0.175	30.1	1959
110	55	109.8	liquid	660	0.010	1.212	0.278	47.9	3116
111	55	100.7	liquid	711	0.010	1.212	0.273	47.0	3009
112	55	100.7	liquid	711	0.010	1.212	0.256	44.2	2838
113	55	123.8	liquid	555	0.010	1.212	0.177	30.4	2002
114	55	113.9	liquid	634	0.010	1.212	0.231	39.7	2554
115	55	117.6	liquid	607	0.010	1.212	0.223	38.3	2473
116	55	140.4	supercritical	283	0.010	1.212	0.148	25.5	1683
117	55	150.7	supercritical	196	0.010	1.212	0.113	19.5	1294
118	55	156.9	supercritical	169	0.010	1.212	0.106	18.3	1214
119	50	158.2	supercritical	144	0.010	1.212	0.099	17.1	1141
120	20	125.1	vapor	498	0.010	1.221	0.114	19.6	1323
121	40	116.4	liquid	599	0.009	1.108	0.173	29.8	1935
122	40	116.9	liquid	599	0.008	1.023	0.146	25.1	1685
123	40	118.1	liquid	584	0.007	0.765	0.139	23.9	1619
124	40	116.3	liquid	600	0.006	0.602	0.114	19.6	1340
125	40	113.1	liquid	625	0.005	0.425	0.103	17.7	1218
126	40	105.6	liquid	677	0.004	0.386	0.090	15.5	1057
127	40	88.0	liquid	768	0.011	1.222	0.225	38.7	2263
128	40	97.0	liquid	729	0.011	1.222	0.172	29.6	1907
129	40	123.7	liquid	519	0.011	1.222	0.107	18.4	1187
130	40	113.1	liquid	625	0.011	1.222	0.184	31.8	1967
131	40	113.1	liquid	625	0.012	1.222	0.188	32.3	1979

Test	P_{inj} (bar)	T_{inj} (K)	Phase	ρ_{inj} kg/m^3	Injection period (s)	Lift (mm)	Mass (g)	P_{eak} (bar)	dp/dt (bar/s)
132	40	110.9	liquid	641	0.012	1.222	0.187	32.2	1956
133	40	115.0	liquid	611	0.012	1.222	0.144	24.8	1600
134	40	117.7	liquid	587	0.009	1.108	0.136	23.4	1490
135	40	118.8	liquid	577	0.009	1.108	0.133	22.9	1462
136	40	131.5	supercritical	232	0.008	1.023	0.070	12.1	810
137	40	94.2	liquid	738	0.008	1.023	0.151	25.9	1586
138	40	102.5	liquid	693	0.008	1.023	0.138	23.8	1533
139	40	99.4	liquid	711	0.008	1.023	0.132	22.7	1424
140	40	99.1	liquid	713	0.007	0.765	0.118	20.3	1292
141	40	98.4	liquid	716	0.007	0.765	0.117	20.2	1289
142	40	95.1	liquid	734	0.007	0.765	0.125	21.5	1318
143	40	97.0	liquid	724	0.006	0.602	0.106	18.3	1118
144	40	97.4	liquid	721	0.006	0.602	0.105	18.0	1154
145	40	94.9	liquid	734	0.006	0.602	0.108	18.6	1125
146	40	96.6	liquid	725	0.006	0.602	0.104	17.9	1090
147	40	101.8	liquid	697	0.005	0.425	0.089	15.4	890
148	40	117.4	liquid	589	0.005	0.425	0.056	9.6	856
149	40	135.1	supercritical	180	0.005	0.425	0.047	8.1	570
150	40	99.6	liquid	710	0.005	0.425	0.081	14.0	871
151	40	108.8	liquid	655	0.005	0.425	0.057	9.8	662
152	40	111.0	liquid	640	0.005	0.425	0.063	10.8	735
153	40	116.6	liquid	596	0.004	0.386	0.033	5.7	388
154	40	115.4	liquid	606	0.004	0.386	0.035	6.0	408
155	40	105.4	liquid	676	0.004	0.386	0.056	9.7	643
156	40	108.2	liquid	660	0.004	0.386	0.045	7.7	521
157	55	105.2	liquid	687	0.010	1.222	0.162	28.0	1766
158	55	107.3	liquid	675	0.010	1.212	0.281	48.4	3124
159	55	106.9	liquid	677	0.008	1.023	0.269	46.4	3007
160	55	115.7	liquid	621	0.006	0.602	0.216	37.1	2460
161	55	117.0	liquid	611	0.004	0.386	0.146	25.1	1728
162	55	109.4	liquid	663	0.012	1.222	0.282	48.6	2961
163	55	119.1	liquid	596	0.014	1.222	0.269	46.2	2856
164	55	146.8	supercritical	216	0.010	1.212	0.083	35.8	2328
165	55	153.1	supercritical	183	0.010	1.212	0.073	31.3	2028
166	55	160.3	supercritical	159	0.010	1.212	0.065	27.9	1824
167	55	170.6	supercritical	137	0.010	1.212	0.060	25.8	1697
168	55	174.8	supercritical	131	0.010	1.212	0.057	24.5	1608
169	55	180.7	supercritical	123	0.010	1.212	0.056	23.9	1564
170	55	182.8	supercritical	120	0.010	1.212	0.054	23.1	1491
171	55	186.5	supercritical	116	0.010	1.212	0.053	22.8	1493
172	55	190.2	supercritical	112	0.010	1.212	0.051	21.9	1432
173	55	193.0	supercritical	110	0.010	1.212	0.050	21.7	1419
174	50	199.4	supercritical	94	0.010	1.212	0.120	20.6	1363
175	50	202.4	supercritical	92	0.010	1.212	0.117	20.2	1328
176	50	204.9	supercritical	90	0.010	1.212	0.112	19.4	1274

Test	P_{inj} (bar)	T_{inj} (K)	Phase	ρ_{inj} kg/m^3	Injection period (s)	Lift (mm)	Mass (g)	P_{eak} (bar)	dp/dt (bar/s)
177	15	106.0	liquid	654	0.010	1.212	0.030	13.1	742
178	15	106.2	liquid	652	0.010	1.212	0.033	14.1	775
179	15	109.5	liquid	626	0.010	1.212	0.038	16.4	737
180	15	102.2	liquid	680	0.010	1.212	0.037	15.8	812
181	15	89.2	liquid	754	0.010	1.212	0.166	28.6	892
182	15	95.9	liquid	718	0.010	1.212	0.058	25.1	944
183	25	99.7	liquid	701	0.010	1.212	0.072	30.8	1926
184	25	88.4	liquid	759	0.010	1.212	0.085	36.5	1099
185	25	92.8	liquid	739	0.010	1.212	0.079	34.1	1782
186	35	88.4	liquid	765	0.010	1.212	0.076	32.8	1779
187	35	87.4	liquid	769	0.010	1.212	0.081	34.8	1840
188	35	88.0	liquid	766	0.010	1.212	0.080	34.2	1843
189	15	291.1	vapour	17	0.010	1.212	0.010	4.3	298
190	25	291.1	vapour	29	0.010	1.212	0.011	8.4	323
191	25	291.8	vapour	29	0.010	1.212	0.011	4.5	339
192	25	103.3	liquid	680	0.010	1.212	0.056	24.1	1361
193	25	99.2	liquid	704	0.010	1.212	0.062	30.5	1153
194	25	96.5	liquid	719	0.010	1.212	0.058	32.2	808
195	25	99.8	liquid	701	0.010	1.212	0.007	19.8	12

Table **B**: Flow tests

Test	P_{inj} (bar)	T_{inj} (K)	Phase	Valve speed (Hz)	Demand (ms)	Lift (mm)	$\dot{Q}_g$ (l/s)	Injection duration (s)	Injected mass (kg)
1	24	104.4	Liquid	5	5	0.542	68	4.4	0.377
2	24	102.0	Liquid	5	5	0.536	67	6.6	0.555
3	25	108.0	Liquid	5	5	0.516	74	5.6	0.518
4	26	109.0	Liquid	5	10	1.165	77	7.8	0.757
5	26	106.8	Liquid	5	10	1.167	80	8.1	0.808
6	27	107.6	Liquid	5	7	0.582	80	6.4	0.644
7	27	102.4	Liquid	5	7	0.572	88	4.4	0.488
8	27	101.0	Liquid	5	7	0.560	88	5.2	0.577
9	29	101.5	Liquid	5	5	0.542	84	3.6	0.381
10	28	105.5	Liquid	5	5	0.496	86	3.6	0.388
11	29	96.8	Liquid	5	10	1.132	93	4.6	0.540
12	29	102.0	Liquid	5	10	1.128	91	6.0	0.690
13	29	102.1	Liquid	5	10	1.130	94	4.6	0.547
14	29	106.8	Liquid	5	7.5	0.552	86	4.4	0.479
15	29	102.4	Liquid	5	7.5	0.578	87	5.0	0.548
16	29	104.4	Liquid	5	7.5	0.566	89	5.0	0.563
17	28	102.9	Liquid	5	7.5	0.552	89	5.8	0.647
18	15	104.5	Liquid	5	5	0.516	59	5.8	0.428
19	44	101.7	Liquid	5	5	0.516	91	3.2	0.366
20	44	100.4	Liquid	5	7.5	0.588	101	5.2	0.664
21	44	97.9	Liquid	5	10	1.173	113	4.6	0.655
22	44	97.0	Liquid	5	10	1.120	115	4.4	0.640
23	44	95.5	Liquid	5	10	1.175	108	6.6	0.898
24	44	95.8	Liquid	5	10	1.171	115	4.8	0.694
25	45	96.4	Liquid	5	10	1.120	121	4.6	0.699
26	47	97.6	Liquid	5	5	0.516	95	5.2	0.621
27	46	96.9	Liquid	5	5	0.516	96	6.0	0.724
28	46	97.7	Liquid	5	5	0.516	97	5.6	0.682
29	47	100.5	Liquid	5	7.5	0.631	107	4.8	0.644
30	46	100.5	Liquid	5	7.5	0.657	102	5.8	0.743
31	46	105.7	Liquid	5	7.5	0.679	99	5.4	0.676
32	46	112.1	Liquid	5	7.5	0.667	101	4.0	0.511
33	47	120.2	Liquid	5	5	0.516	95	3.6	0.429
34	46	106.3	Liquid	5	12.5	1.195	76	6.6	0.633
35	11	108.7	Gas	5	10	1.197	38	8.5	0.399
36	11	104.9	Liquid	5	10	1.189	48	5.8	0.350
37	11	96.3	Liquid	5	10	1.193	58	9.7	0.701
38	11	89.9	Liquid	5	5	0.516	83	6.4	0.668
39	11	93.4	Liquid	5	5	0.516	81	6.0	0.610
40	11	98.4	Liquid	5	5	0.516	75	6.2	0.585
41	11	107.9	Gas	5	7.5	0.725	44	6.4	0.355
42	70	101.5	Liquid	5	10	1.191	117	6.4	0.940
43	66	102.5	Liquid	5	7.5	0.733	102	4.4	0.563

Test	P_{inj} (bar)	T_{inj} (K)	Phase	Valve speed (Hz)	Demand (ms)	Lift (mm)	$\dot{Q}_g$ (l/s)	Injection duration (s)	Injected mass (kg)
44	59	98.1	Liquid	5	7.5	0.709	98	6.2	0.767
45	54	98.1	Liquid	5	7.5	0.697	103	5.6	0.728
46	50	99.1	Liquid	5	7.5	0.699	110	4.2	0.583
47	41	103.9	Liquid	5	5	0.496	88	4.0	0.444
48	38	101.9	Liquid	5	5	0.496	89	4.6	0.513
49	34	100.0	Liquid	5	5	0.496	89	5.0	0.561
50	50	103.0	Liquid	2	10	1.205	60	5.0	0.377
51	50	96.8	Liquid	2	10	1.189	62	5.0	0.387
52	50	95.5	Liquid	2	10	1.185	62	5.0	0.390
53	50	95.0	Liquid	2	10	1.193	64	5.0	0.398
54	51	99.5	Liquid	2	10	1.199	64	5.0	0.397
55	52	107.7	Liquid	2	7	0.973	49	5.0	0.308
56	52	107.2	Liquid	2	7	0.991	50	5.0	0.315
57	52	107.6	Liquid	2	7	1.002	51	5.0	0.318
58	53	108.1	Liquid	2	7	1.018	51	5.0	0.321
59	53	108.3	Liquid	2	7	1.008	51	5.0	0.316
60	54	99.6	Liquid	2	8	1.104	55	5.0	0.345
61	54	96.9	Liquid	2	8	1.122	57	5.0	0.357
62	53	97.7	Liquid	2	8	1.137	58	5.0	0.362
63	54	99.3	Liquid	2	8	1.147	58	5.0	0.364
64	54	101.4	Liquid	2	8	1.159	58	5.0	0.361
65	53	115.1	Liquid	2	9	1.044	54	5.0	0.337
66	55	119.3	Liquid	2	9	1.189	53	5.0	0.329
67	52	122.1	Liquid	2	9	1.193	49	5.0	0.308
68	49	123.7	Liquid	2	8	1.199	46	5.0	0.291
69	31	105.9	Liquid	2	8	1.197	47	5.0	0.295
70	94	111.0	Liquid	2	10	1.157	72	5.0	0.451
71	94	107.9	Liquid	2	10	1.163	74	5.0	0.462
72	93	106.9	Liquid	2	10	1.200	75	5.0	0.466
73	93	106.4	Liquid	2	10	1.200	76	5.0	0.472
74	93	106.2	Liquid	2	10	1.200	76	5.0	0.475
75	93	105.8	Liquid	2	10	1.200	77	5.0	0.481
76	94	105.9	Liquid	2	10	1.200	78	5.0	0.487
77	93	107.6	Liquid	2	10	1.200	78	5.0	0.486
78	93	106.2	Liquid	2	10	1.200	79	5.0	0.493
79	93	105.4	Liquid	2	10	1.200	79	5.0	0.495
80	92	106.4	Liquid	2	10	1.200	78	5.0	0.490
81	82	106.1	Liquid	5	10	1.200	136	5.0	1.513
82	84	107.3	Liquid	5	10	1.200	136	5.0	1.508
83	75	103.5	Liquid	5	10	1.200	134	5.0	1.487
84	73	108.6	Liquid	2	10	1.200	72	5.0	0.451
85	69	105.5	Liquid	2	10	1.200	72	5.0	0.453
86	68	106.5	Liquid	2	10	1.200	73	5.0	0.456
87	65	106.3	Liquid	2	10	1.200	73	5.0	0.457
88	62	105.2	Liquid	2	10	1.200	72	5.0	0.453

Test	P_{inj} (bar)	T_{inj} (K)	Phase	Valve speed (Hz)	Demand (ms)	Lift (mm)	$\dot{Q}_g$ (l/s)	Injection duration (s)	Injected mass (kg)
89	59	105.1	Liquid	2	10	1.200	72	5.0	0.448
90	57	105.6	Liquid	2	10	1.200	71	5.0	0.444
91	51	103.8	Liquid	5	10	1.200	120	5.0	1.335
92	63	107.7	Liquid	5	10	1.200	117	5.0	1.338
93	62	99.5	Liquid	5	10	1.210	121	5.0	1.386
94	63	98.4	Liquid	5	10	1.202	124	5.0	1.425
95	63	99.6	Liquid	5	10	1.202	125	5.0	1.445
96	62	97.4	Liquid	5	10	1.200	125	5.0	1.447
97	63	98.7	Liquid	5	10	1.200	125	5.0	1.447
98	66	108.6	Liquid	5	10	1.204	122	5.0	1.407
99	65	101.5	Liquid	5	10	1.200	125	5.0	1.444
100	64	101.3	Liquid	5	10	1.200	125	5.0	1.445
101	65	102.1	Liquid	5	10	1.200	124	5.0	1.433
102	65	103.5	Liquid	5	10	1.200	123	5.0	1.428
103	64	103.6	Liquid	5	10	1.200	122	5.0	1.415
104	64	105.4	Liquid	5	10	1.200	120	5.0	1.387
105	64	107.7	Liquid	5	10	1.200	117	5.0	1.358
106	65	111.2	Liquid	5	10	1.200	114	5.0	1.323
107	65	115.8	Liquid	5	10	1.200	110	5.0	1.275
108	66	122.3	Liquid	5	10	1.200	102	5.0	1.178
109	66	130.8	Gas	5	10	1.200	89	5.0	0.555
110	66	98.8	Liquid	5	10	1.174	119	5.0	1.374
111	67	105.5	Liquid	5	9	1.153	113	5.0	0.709
112	67	101.9	Liquid	5	8	1.023	104	5.0	0.649
113	67	96.8	Liquid	5	7	0.944	98	5.0	0.611
114	67	96.4	Liquid	5	6	0.765	88	5.0	0.551
115	68	96.5	Liquid	5	5	0.624	80	5.0	0.503
116	69	99.3	Liquid	5	4	0.386	67	5.0	0.417
117	69	98.8	Liquid	5	3	0.226	59	5.0	0.369
118	71	104.9	Liquid	5	2	0.054	30	5.0	0.189
119	69	104.1	Liquid	5	10	1.204	126	5.0	1.463
120	68	95.6	Liquid	5	10	1.208	130	5.0	1.509
121	67	95.3	Liquid	5	10	1.214	132	5.0	1.531
122	68	95.7	Liquid	5	10	1.218	131	5.0	1.519
123	67	95.7	Liquid	5	10	1.208	130	5.0	1.505
124	85	97.8	Liquid	5	10	1.202	136	5.0	1.570
125	83	97.9	Liquid	5	10	1.206	134	5.0	1.546
126	78	100.2	Liquid	5	10	1.216	130	5.0	1.500
127	75	103.4	Liquid	5	10	1.214	126	5.0	1.453
128	39	109.3	Liquid	5	10	1.214	97	5.0	1.121
129	65	105.8	Liquid	5	10	1.214	119	5.0	1.372
130	63	106.1	Liquid	5	10	1.216	117	5.0	1.353
131	56	105.0	Liquid	5	10	1.216	114	5.0	1.321
132	52	105.8	Liquid	5	10	1.218	111	5.0	1.283
133	47	107.0	Liquid	5	10	1.222	106	5.0	1.229

Test	P_{inj} (bar)	T_{inj} (K)	Phase	Valve speed (Hz)	Demand (ms)	Lift (mm)	$\dot{Q}_g$ (l/s)	Injection duration (s)	Injected mass (kg)
134	48	112.6	Liquid	5	10	1.216	101	5.0	1.169
135	42	106.3	Liquid	5	10	1.212	101	5.0	1.171
136	37	106.3	Liquid	5	10	1.216	97	5.0	1.118
137	32	105.0	Liquid	5	10	1.218	94	5.0	1.082
138	30	104.8	Liquid	5	10	1.216	92	5.0	1.063
139	29	104.9	Liquid	5	10	1.220	90	5.0	1.037
140	27	105.4	Liquid	5	10	1.214	86	5.0	0.997
141	71	100.9	Liquid	5	10	1.204	116	5.0	1.346
142	71	98.3	Liquid	5	10	1.206	119	5.0	1.378
143	73	98.3	Liquid	5	10	1.212	131	5.0	1.517
144	73	95.7	Liquid	5	10	1.212	132	5.0	1.521
145	73	93.8	Liquid	5	10	1.210	132	5.0	1.525
146	72	93.8	Liquid	5	10	1.212	131	5.0	1.516
147	72	95.9	Liquid	5	10	1.214	126	5.0	1.454
148	72	97.7	Liquid	5	10	1.220	128	5.0	1.479
149	71	99.8	Liquid	5	10	1.218	125	5.0	1.449
150	72	103.1	Liquid	5	10	1.216	118	5.0	1.370
151	72	106.7	Liquid	5	10	1.214	118	5.0	1.361
152	53	120.7	Liquid	5	10	1.220	94	5.0	1.089
153	53	122.4	Liquid	5	10	1.218	90	5.0	1.044
154	48	122.5	Liquid	5	10	1.216	84	5.0	0.974
155	44	124.0	Liquid	5	10	1.210	76	5.0	0.875
156	41	125.2	Liquid	5	10	1.216	67	5.0	0.779
157	47	95.2	Liquid	5	10	1.212	92	5.0	1.059
158	28	99.9	Liquid	5	10	1.212	89	5.0	1.032
159	48	93.3	Liquid	5	10	1.212	99	5.0	1.149
160	46	91.4	Liquid	5	10	1.214	101	5.0	1.163
161	43	91.4	Liquid	5	10	1.210	101	5.0	1.166
162	40	90.8	Liquid	5	10	1.208	100	5.0	1.159
163	39	92.1	Liquid	5	10	1.212	100	5.0	1.160
164	36	90.8	Liquid	5	10	1.210	100	5.0	1.159
165	34	91.3	Liquid	5	10	1.215	99	5.0	1.149
166	32	91.6	Liquid	5	10	1.208	99	5.0	1.140
167	30	91.5	Liquid	5	10	1.212	98	5.0	1.129
168	29	92.9	Liquid	5	10	1.210	95	5.0	1.094
169	27	94.0	Liquid	5	10	1.212	92	5.0	1.064
170	25	95.5	Liquid	5	10	1.206	90	5.0	1.036
171	26	99.3	Liquid	5	10	1.206	87	5.0	1.008
172	24	100.8	Liquid	5	10	1.212	84	5.0	0.967
173	23	104.6	Liquid	5	10	1.212	74	5.0	0.860
174	17	108.4	Liquid	5	10	1.212	60	5.0	0.692
175	78	96.8	Liquid	5	10	1.154	115	5.0	1.327
176	78	97.1	Liquid	5	10	1.212	114	5.0	1.320
177	78	97.1	Liquid	5	10	1.212	116	5.0	1.339
178	78	97.8	Liquid	5	10	1.212	116	5.0	1.339

Test	P_{inj} (bar)	T_{inj} (K)	Phase	Valve speed (Hz)	Demand (ms)	Lift (mm)	$\dot{Q}_g$ (l/s)	Injection duration (s)	Injected mass (kg)
179	78	99.0	Liquid	5	10	1.212	117	5.0	1.351
180	78	101.2	Liquid	5	10	1.212	116	5.0	1.339
181	79	104.2	Liquid	5	10	1.212	114	5.0	1.318
182	78	108.0	Liquid	5	10	1.212	113	5.0	1.313
183	79	112.2	Liquid	5	10	1.212	111	5.0	1.283
184	79	116.8	Liquid	5	10	1.212	108	5.0	1.255
185	79	121.1	Liquid	5	10	1.212	104	5.0	1.203
186	79	124.1	Liquid	5	10	1.212	100	5.0	1.160
187	78	125.3	Liquid	5	10	1.212	99	5.0	1.141
188	75	99.1	Liquid	5	10	1.212	102	5.0	1.178
189	80	100.7	Liquid	5	10	1.212	109	5.0	1.260
190	82	99.4	Liquid	5	10	1.212	111	5.0	1.281
191	81	94.3	Liquid	5	10	1.212	114	5.0	1.324
192	82	94.2	Liquid	5	10	1.212	116	5.0	1.340
193	80	93.0	Liquid	5	10	1.212	117	5.0	1.355
194	81	94.5	Liquid	5	10	1.212	117	5.0	1.358
195	80	94.5	Liquid	5	10	1.212	117	5.0	1.351
196	57	96.9	Liquid	5	10	1.212	101	5.0	1.172
197	44	95.6	Liquid	5	10	1.212	96	5.0	1.111
198	43	98.8	Liquid	5	10	1.212	94	5.0	1.085
199	42	96.5	Liquid	5	10	1.211	96	5.0	1.114
200	42	99.1	Liquid	5	10	1.211	94	5.0	1.090
201	42	105.0	Liquid	5	10	1.211	89	5.0	1.028
202	43	114.7	Liquid	5	10	1.211	81	5.0	0.932
203	43	124.9	Liquid	5	10	1.211	65	5.0	0.747